Compressive mechanics of hyaluronan-rich pericellular matrices – A study on a biomimetic model film, combining atomic force and reflection interference contrast microscopy

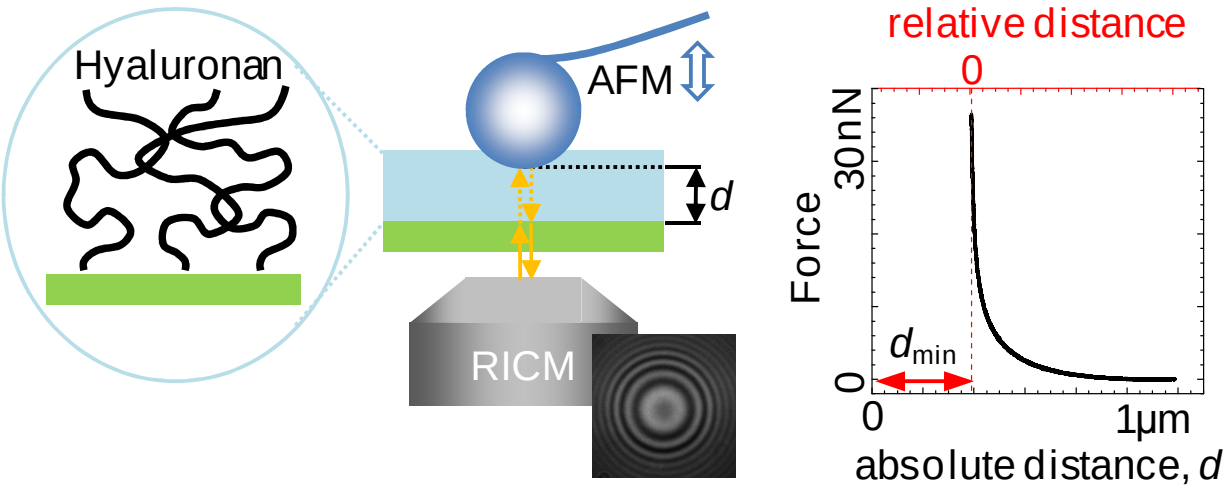

Seetharamaiah Attili

2012

Universidad del País Vasco
Euskal Herriko Unibertsitatea

Department of Biochemistry and Molecular Biology,
University of Basque Country, Spain.

Compressive mechanics of hyaluronan-rich pericellular matrices – A study on a biomimetic model film, combining atomic force and reflection interference contrast microscopy

Dissertation presented to the Department of Biochemistry and Molecular Biology to obtain the degree of Doctor from the University of Basque Country

by

SEETHARAMAIAH ATTILI

Thesis advisor: Dr. Ralf P. Richter

University Tutor: Prof. Felix Goñi Urcelay

Donostia-San Sebastian

2012

Universidad del País Vasco
Euskal Herriko Unibertsitatea

The thesis has been performed at:

CIC biomaGUNE

Biosurfaces Unit,

Donostia-San Sebastian,

Spain.

Max-Planck-Institute for Intelligent Systems

Department of New Materials and Biosystems,

Stuttgart,

Germany.

Asato maa sad-gamaya

Tamaso maa jyotir-gamaya

Mrtyor-maa amrtam-gamaya

Lead us from Ignorance to Truth

Lead us from Darkness to Light

Lead us from Mortality to Immortality

(Brhadaranyaka Upanishad — I.iii.28)

Acknowledgements

My first gratitude would go to Dr. Ralf Richter, who not only served as my supervisor but also encouraged and challenged me throughout my education for the past four years. I especially feel thankful for Ralf's extraordinary patience and his continuous support at times needed. I am deeply impressed with Ralf's broad and deep knowledge in basic science and in particular his expertise in engineering the lab accessories. His brilliance as a well-balanced researcher with punctual working style and valuable suggestions from time to time and guidance helped me to finish my project on time that resulted in shaping up of this thesis. I thank Ralf for his mentorship and the skills he has given me to face the next challenge in my professional career.

The work would not have been so easy without the co-operation of my co-workers in the group. I thank Ixaskun Carton and Dr. Patricia Wolny for their help and guidance during my initial days in Spain. Dr. Anja Bernecker, Nico Eisele and Natalia Baranova for the fruitful discussions. Dr. Leire Diaz for the suggestions, and helping me in the organization of the documents during the submission process. Dr. Galina Dubacheva for the good advices during writing of my thesis.

Many thanks to people at CIC biomaGUNE, starting from administration to maintenance staff to information technology department and each and every person working at different groups, who helped me in one or the other way in and outside of office. Your friendly nature and social events out of work made my stay pleasant here in Donostia, in particular to Gabriela Romero for sharing my joy and her role of care-taker and for helping me to translate the information from English to Spanish.

Nothing would have been possible without the support of my parents and my loving brother. Thanks for the lovely words of congratulations and encouragement I have been getting from you at each and every phase of my career.

Abstract

Hyaluronan (HA) is a naturally occurring linear, negatively charged polysaccharide that plays a vital role in the mechanical integrity and function of pericellular matrices (PCM) surrounding many cell types and that is becoming increasingly popular in biomedical applications. Elucidating the mechanical properties of the highly hydrated HA-rich matrices would be valuable to understand how PCMs are organized and how they function. For a thorough investigation of the physical principles underlying the biological function of HA-rich pericellular matrices and provided the instrumental limitations in studying these highly hydrated systems *in vivo*, we have studied a model system that is based on films of HA that is end-grafted to a supported lipid bilayer. The major characterization techniques used are atomic force microscopy (AFM) and reflection interference contrast microscopy (RICM), as well as quartz crystal microbalance with dissipation monitoring (QCM-D) and spectroscopic ellipsometry.

In this thesis, we combine AFM, a widely used analytical approach to determine the behavior of molecules or thin films under mechanical force, and colloidal probe RICM, an established microinterferometric technique to determine the thickness of soft hydrated films, into one instrument. The combination provides interaction forces as a function of the absolute distance between the two approaching surfaces, information that may not easily be obtained with either technique alone. We employ the combined setup to quantify the thickness of films of end-grafted HA, and their resistance to compression forces as a function of the external salt concentration. We find a swelling behavior that is consistent with expectations for a polyelectrolyte brush. Through comparison of the experimental data with polymer theory, molecular parameters that govern the swelling and force response are identified and quantified. Intercalation of aggrecan, a HA-binding proteoglycan prominent in the PCM of chondrocytes, drastically increased the thickness and resistance of HA films to compression.

The combined AFM/RICM setup can serve as powerful tool to study the compression and frictional forces of surface-confined, hydrated films in general. The data on the mechanical properties of well-defined HA and HA/aggrecan composite films can be used as a reference point for future studies on the mechanics of PCMs.

Resumen

El ácido hialurónico (HA) es un polisacárido de estructura naturalmente linear y cargado negativamente, que juega un papel de vital importancia en la integridad mecánica y en el funcionamiento de las matrices pericelulares (PCM) que rodean a muchos tipos de células, y que se ha convertido en un material muy popular para aplicaciones biomédicas. El HA pertenece a la familia de los glicosaminoglicanos (GAG), y es el único GAG que no está sulfonado. HA lo sintetizan de forma natural una clase de proteínas integrales de membrana llamadas ácido hialurónico sintasas, que extruyen el HA directamente al espacio extracelular. El HA es un polímero regular compuesto por unidades de disacáridos, cada una formada por ácido glucurónico y N-acetilglucosamina, unidos por medio de enlaces glicosídicos β-1,4 y β-1,3. El número de unidades repetitivas de disacárido en una molécula completa de ácido hialurónico puede llegar hasta 10 000 o más, con un peso molecular alto (10^5-10^7 Da) y pueden llegar a extenderse varios micrómetros en longitud (~10 μm) si la molécula de HA está extendida de extremo a extremo.

El HA es una molécula de magnitud megadalton y sus propiedades físico-químicas y biológicas dependen de su peso molecular. La conformación y las propiedades del HA también pueden verse afectadas por las condiciones del entorno (ej. fuerza iónica), por la unión a superficies, por la exposición a fuerzas mecánicas, y por la presencia de otras biomoléculas que puedan interaccionar con el HA (las llamadas hialadherinas). La sub-familia de hialadherinas extracelulares formada por agrecano, versicano, neurocano y brevicano, son proteínas (o proteoglicanos) ricos en sulfato de condroitina, que pueden formar complejos grandes con el HA, estabilizados por una proteína de unión.

El agrecano es el más largo de los proteoglicanos, y puede ser encontrado predominantemente y en grandes concentraciones en el cartílago. El agrecano está compuesto por un núcleo de proteína, de tres dominios globulares (G1, G2, y G3), y por dos tipos de cadenas de glicosaminoglicanos (GAG) en los extremos: sulfato de condroitina (CS) y sulfato de queretán (KS). La capacidad de los

cartílagos articulares de resistir a la compresión, se debe principalmente a las cadenas de CS GAG. Una interpretación a nivel macroscópico, independientemente de la estructura molecular, es que la alta densidad de cargas negativas fijas de los grupos sulfato y carboxilato en las cadenas de GAG crea una fuerza de repulsión que debe ser neutralizada por los iones móviles con carga positiva del fluido que los rodea. La alta concentración de iones en los tejidos, comparada con la concentración de iones fuera de ellos, genera una presión de hinchazón y arrastra agua dentro de los tejidos. En la ausencia de alguna carga aplicada, la tendencia de hinchazón de los proteoglicanos es moderada por las cadenas de tejidos de colágeno, dando lugar a un comportamiento de compresión del cartílago. En el cartílago, el agrecano interacciona con el HA a través de su N terminal del dominio G1, donde el agrecano se une de forma no covalente al ácido hialurónico. Esta interacción es estabilizada por una proteína de unión, la proteína se une no covalentemente al HA y al dominio G1 del agrecano. La interacción de múltiples complejos de agrecano y proteína de unión con una sola cadena de HA (megadalton), puede generar complejos supramoleculares grandes.

El estudio de las propiedades mecánicas de matrices altamente hidratadas y ricas en HA, es de gran valor para el entendimiento de la organización y función de las PCMs. Para la meticulosa investigación de los fundamentos físicos que sostienen las funciones biológicas de las matrices pericelulares ricas en HA, y para contribuir a las limitaciones instrumentales existentes en el estudio *in vivo* de estos sistemas altamente hidratados, un sistema modelo basado en películas de HA con uno de los extremos unido a un soporte de bicapa de lípidos ha sido estudiado. Este sistema modelo adaptado de ácido hialurónico y rico recubrimiento pericelular, ofrece la posibilidad de estudiar la relación entre la composición, la estructura supramolecular y la dinámica, las propiedades fisicoquímicas y las funciones biológicas de ensamblados de HA en PCM. En este modelo, el peso molecular del HA está bien controlado, y las propiedades fisicoquímicas de las películas de HA en función de factores externos (proteínas de unión del HA) son accesibles para una investigación cuantitativa adecuada por medio de técnicas biofísicas sensibles a superficies.

Las técnicas de caracterización más importantes utilizadas son la microscopía de fuerza atómica (AFM) y la microscopía de contraste por interferencia de reflexión (RICM), así como también la microbalanza de cuarzo con disipación (QCM-D) y la elipsometría espectroscópica.

Cuando se analizan películas de polímero, un problema fundamental en los experimentos de AFM usando una sonda coloidal es la determinación de la distancia entre el coloide y el substrato en el que la película está depositada, cuando están más próximos el uno del otro. La combinación *in situ* de AFM y RICM, permite medir de manera simultánea las fuerzas y las distancias absolutas. En el Capítulo 2 de esta tesis, está descrito un método que combina AFM de sonda coloidal y RICM para caracterizar las propiedades mecánicas de películas poliméricas finas y solvatadas. Utilizando este sistema combinado, fue posible cuantificar la mecánica de compresión de películas de polisacárido de ácido hialurónico único en uno de sus extremos a un soporte formado por una bicapa de lípidos. Los datos experimentales, comparados con la teoría de los polímeros, muestran que las películas de ácido hialurónico pueden ser descritas como cepillos poliméricos elásticos, muy blandos y altamente solvatados. La novedosa combinación *in situ* de AFM de sonda coloidal y RICM desarrollada en esta tesis, permite comprobar las fuerzas de compresión e incluso, potencialmente, las fuerzas de fricción de películas de polímero con una superficie confinada con un estrecho control sobre la distancia entre las dos superficies. Ambas técnicas de caracterización son altamente complementarias: con AFM se obtienen las fuerzas en función de la distancia relativa con alta resolución; mientas que con RICM se obtiene la distancia absoluta, que permite la corrección de las derivas instrumentales lineares de los datos obtenidos por AFM, e incluso, se puede obtener la sensibilidad del cantilever sin ninguna medida extra de referencia. Este método representa una nueva herramienta para la correlación cuantitativa entre la organización supramolecular y las propiedades mecánicas de superficies confinadas de ensamblados de HA, y de películas poliméricas altamente solvatadas como los cepillos poliméricos en general.

Los ensamblados altamente hidratados compuestos del proteoglicano agrecano y del polisacárido ácido hialurónico, son esenciales para las funciones mecánicas del cartílago, y su modificación está relacionada como el origen de patologías como la osteoartritis. Para el mejor entendimiento de cómo surgen las propiedades mecánicas de las estructuras supramoleculares y la dinámica de tales ensamblados, en el Capítulo 3, se estudia el efecto del agrecano sobre las propiedades fisicoquímicas de películas bien definidas y reconstituidas, formadas por una superficie unida a cadenas de HA. De los estudios de interacción por medio de técnicas sensibles a superficies, como QCM-D y elipsometría espectroscópica, y estudios mecánicos mediante el sistema combinado de

AFM de sonda coloidal/RICM, se encontró que el agrecano se intercala fácilmente y de forma reversible dentro de los cepillos de HA. Para el análisis de los datos obtenidos en elipsometría, se aplicó un método de análisis mejorado que toma en cuenta el perfil de densidad parabólico del espesor óptico de las cepillos de HA. El resultado de tal análisis es consistente con las medidas obtenidas de fuerza de compresión.

El agrecano induce una hinchazón drástica en los cepillos de HA, generando así películas auto-ensambladas altamente hidratadas y muy blandas, con varios micrómetros de espesor. El módulo de Young en régimen de compresión linear es por debajo de 100 Pa, y llega a alcanzar algunos kPa cuando la compresión es fuerte. Las implicaciones de los hallazgos para funciones biológicas son citadas. El entendimiento puede ser de interés para otro tipo de complejos de proteoglicanos-HA. El método representa una nueva herramienta para la correlación cuantitativa entre la organización supramolecular y las propiedades mecánicas de ensamblados de HA con superficie confinada.

Para el mejor entendimiento de los fenómenos físicos que gobiernan el comportamiento mecánico de los ensamblados de HA, en el Capítulo 4 se estudia la respuesta del HA unido en un extremo a una película, a la compresión en un rango amplio de fuerza iónica. Las fuerzas de compresión fueron medidas en función de la distancia absoluta entre la sonda coloidal y la superficie plana en la que la película de HA fue construida, utilizando el sistema combinado de sonda coloidal de AFM/RICM. Las películas de HA fueron definidas en el sentido de que se hicieron de cadenas con una distribución de tamaño estrecha, y que fueron unidas a un soporte sólido a densidad controlada. Las películas de HA puras mostraron una pronunciada dependencia a la sal en su espesor sin compresión y la comparación detallada de los datos experimentales con expresiones analíticas derivadas de la teoría de cepillos de polímeros y polielectrolitos, revelaron que las películas con HA se comportan como cepillos de polielectrolitos fuertemente cargados. Para reproducir cualitativamente los datos experimentales, las interacciones de volumen excluido intrínsecas y la rigidez de cadena intrínseca de la columna de polímero, deben ser tomadas en cuenta. A baja fuerza iónica, las cadenas se extienden casi completamente. En nuestro sistema experimental, se formaron películas de varios micrómetros de espesor, que alcanzaron una hidratación cercana al 99.98%, y en las cuales el espesor del cepillo se reduce más de 5 veces al aumentar la fuerza iónica. Desde la perspectiva biológica, los datos generados representan una

referencia de gran valor para futuros estudios cuantitativos de películas más complejas ricas en HA, como las recubrimientos pericelulares. En general, el estudio proporciona predicciones teóricas cuantitativas para determinar el espesor de una película y la respuesta a la compresión en función de la longitud del HA, la densidad de unión y la fuerza iónica. El nivel de control en su método de preparación, hace de los cepillos de HA un sistema modelo experimental útil para futuros estudios y confirma las teorías de cepillos de polielectrolitos fuertemente cargados e intrínsecamente rígidos.

Las conclusiones generales y las perspectivas son detalladas en el Capítulo 5, y el Capítulo 6 trata los materiales y métodos utilizados en esta tesis.

Recapitulando, se combinó AFM, una técnica analítica muy utilizada para determinar el comportamiento de moléculas o películas finas que experimentan una fuerza mecánica, y la sonda coloidal RICM, que es una técnica microinterferométrica bien establecida para determinar el espesor de películas blandas hidratadas, en un único instrumento. El sistema combinado de AFM/RICM sirve de herramienta poderosa para el estudio de la compresión y fuerzas de fricción de superficies confinadas y películas hidratadas en general. A fuerza iónica y pH fisiológicos, las películas de HA puras mostraron una respuesta de compresión elástica con valores acordes a las predicciones teóricas para cepillos poliméricos. Al intercalar agrecano, un proteoglicano unido covalentemente al HA muy importante en la PCM de los condrocitos, el espesor y la resistencia a la compresión de las películas de HA incrementó drásticamente. Los datos obtenidos sobre las propiedades mecánicas de películas bien definidas de HA y el composite HA/agrecano, pueden ser utilizados como punto de referencia para estudios posteriores en la mecánica de PCMs. La película de composite HA-agrecano soportada sobre una bicapa de lípidos, fabricada en esta tesis, representa un sistema modelo *in vitro* muy interesante para el entendimiento de la mecánica del cartílago.

Al emplear el sistema combinado para cuantificar el espesor de películas unidas a HA, y su resistencia a las fuerzas de compresión en función de la concentración de sal en el exterior, se definió un comportamiento de hinchazón consistente con las predicciones para cepillos poliméricos. A través de la comparación de los datos experimentales con la teoría de los polímeros, los parámetros moleculares que gobiernan la hinchazón y la respuesta a la fuerza fueron definidos y cuantificados. Los datos sobre las propiedades mecánicas de películas definidas de HA y el

composite HA/agrecano, pueden ser utilizados como punto de referencia para estudios posteriores en la mecánica de PCMs.

List of Publications

Some of the work in this thesis has been published or is planned to be published.

Paper I

Combining Colloidal Probe Atomic Force and Reflection Interference Contrast Microscopy to Study the Compressive Mechanics of Hyaluronan Brushes

Seetharamaiah Attili and Ralf P. Richter

*Langmui*r **28** (2012) p3206-3216.

Paper II

Films of End-Grafted Hyaluronan Are a Prototype of a Brush of a Strongly Charged, Semiflexible Polyelectrolyte with Intrinsic Excluded Volume

Seetharamaiah Attili, Oleg V. Borisov, and Ralf. P. Richter

Biomacromolecules **13** (2012) p1466-1477.

Paper III

Hyaluronan-aggrecan brush mechanics

Seetharamaiah Attili and Ralf P. Richter

Manuscript in preparation (2012).

Table of Contents

Introduction

1.1 Objectives and Outline

The purpose of my doctoral work was the study of the compressive force response and mechanical properties of hyaluronan (HA) films. Pure films of tethered HA were investigated in detail. The impact of aggrecan, a key component of cartilage and of chondrocyte pericellular coats, on the mechanics of end-grafted HA brushes is also addressed. To enable highly quantitative studies, technical development was required. One part of my work deals with the implementation of a combined colloidal probe atomic force and reflection interference contrast microscopy setup to study the mechanical properties of surface-confined thin films in general. This involved the making of colloidal-probe cantilevers, establishing the combined setup and improvement in the data analysis. Furthermore the experimental data on the mechanical properties of HA films are confronted with polymer theory to gain insights into structure-function relationships.

The reminder of the this chapter contains a general introduction into the biomolecules of interest in the present work, an overview of the different methods used and a brief introduction into the theory of polymers at surfaces. In Chapter 2, a detailed description of the combination of atomic force microscopy (AFM) and reflection interference contrast microscopy (RICM) into one instrument with improved data analysis is provided. Initial results on the compressive mechanics of HA brushes at physiological ionic strength and pH are also presented. Chapter 3 describes the methodology to prepare HA-aggrecan composite films on solid supported lipid bilayers. The films are investigated by quartz crystal microbalance with dissipation monitoring (QCM-D), spectroscopic ellipsometry and the combined colloidal probe AFM/RICM, to characterize the influence of aggrecan on the morphology and compressive resistance of HA films. Chapter 4 is devoted to the polyelectrolyte behavior of HA films, their conformation and mechanical properties at different ionic strength are studied experimentally. The same chapter gives a detailed description of existing theories of polymer and polyelectrolyte brushes and a comparison of experimental data with the theory.

Chapter 5 provides the general conclusions and perspectives for future research, and Chapter 6 provides a description of Materials and Methods used in this work.

The work covered in Chapter 2 and 3 has resulted in two publications, which have been published in peer-reviewed journals. An additional manuscript on the work covered in Chapter 4 is currently in preparation.

1.2 Biological motivation

A substantial volume fraction of most tissues is extracellular space, which is filled with a complex network of macromolecules constituting the extracellular matrix (ECM) and water. The extracellular matrix is composed of a variety of proteins, fibers, and polysaccharides assembled into an organized meshwork. The macromolecules that make up the ECM are produced by cells embedded in the matrix. The cell-associated pericellular matrix (PCM) mediates between the cell and the ECM. It plays important roles in various cellular processes including proliferation and migration. In particular, PCMs have been proposed to be involved in mechanosensing of cells,[1-3] acting as a mechanotransducer of shear stress.[4, 5] For many cell types the PCM is rich in hyaluronan (HA). HA constitutes the backbone of the PCM and thereby plays a crucial role in the structural and mechanical integrity of the PCM. Degradation of HA causes PCM to collapse.[1]

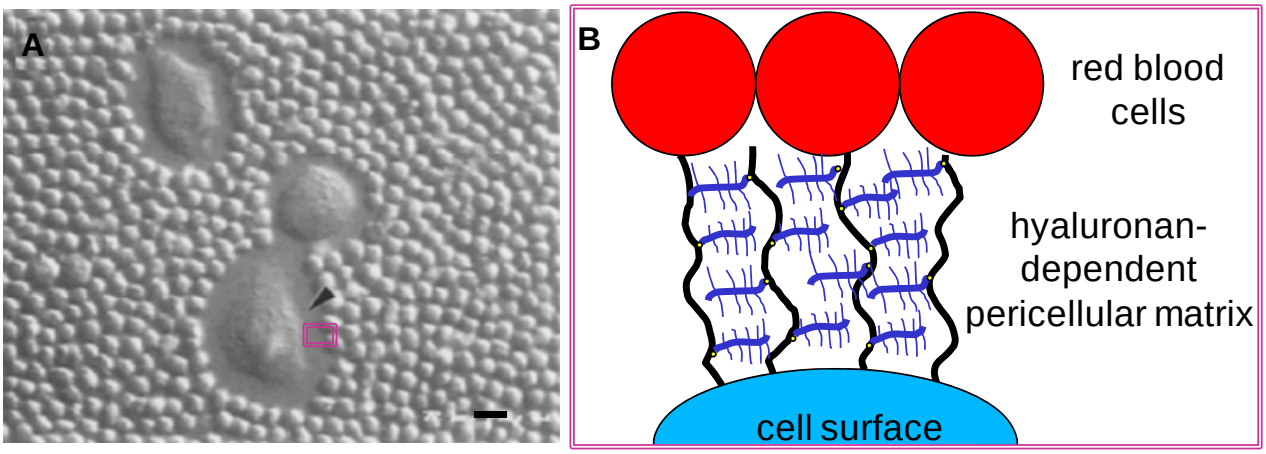

Figure 1.1 (**A**) Hyaluronan dependent matrix (or PCM) of live chondrocytes visualized by a particle exclusion assay (scale bar 10 μm). Adapted from ref. 3 (**B**) Schematic representation of the putative arrangement of HA-aggrecan complexes in PCM.

Because of their strong hydration, PCMs are invisible to conventional light microscopy. The particle exclusion assay (PEA, Figure 1.1) is one of the most common tools to visualize the PCM in cell cultures. In this assay, fixed red blood cells or micrometer sized of similar size are added to the cultured cells at high density; because the particles cannot penetrate the PCM, they outline its periphery.

In articular cartilage, a rather large PCM is surrounding cartilage cells (chondrocytes). The PCM is composed predominantly of aggrecan, a proteoglycan rich in chondrotin sulfate. The chondrocyte

together with the PCM forms a so-called chondron.[6] The PCM influences the biochemical and biomechanical interactions between the cartilage and the chondrocyte. Finite element analysis studies have shown that the mechanical environment of chondrocytes is highly dependent on the relative biomechanical properties of the PCM.[7]

Hyaluronan may remain attached to hyaluronan synthases in the cell membrane. It can also bind to the cell surface though cell surface receptors such as CD44,[8, 9] In a study by Lee and co-workers[3] on chondrocytes, they observed the micrometer thick pericellular coat composed of hyaluronan-aggrecan complexes on live cells isolated from bovine articular cartilage using PEA (Figure 1.1). It was proposed by Lee et al. that the self-organization of aggrecan and cell-surface attached HA is sufficient for the formation of a PCM with a thickness of several micrometers that plays a functional role in the mechanical properties of articular cartilage.[3] Here, aggrecan helps expanding the PCM.[10]

1.3 Hyaluronan

Hyaluronan, also called hyaluronic acid, is a polysaccharide discovered in 1934 by Karl Meyer in the eye clinic of Columbia University.[11] HA is a so-called glycosaminoglycan (GAG). It is unique in being the only non-sulphated member of the GAG family. HA is naturally synthesized by a class of integral membrane proteins called hyaluronan synthases that extrude HA directly into the extracellular space.[12] It is a regular polymer composed of disaccharide units, each consisting of glucuronic acid and N-acetylglucosamine, linked together via β-1,4 and β-1,3 glycosidic bonds (Figure 1.2).[13, 14] The number of repeat disaccharides in a completed hyaluroan molecule can reach 10 000 or more with high molecular weight (10^5-10^7 Da) and could extend up to several micrometers in length (~10 μm), if stretched from end to end.

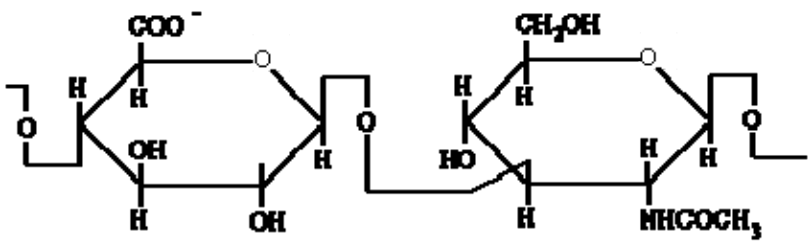

Figure 1.2 The structure of HAs building unit, a disaccharide. HA is a naturally occurring polymer composed of repeated units of glucuronic acid and N-acetylglucosamine (each disaccharide ~1 nm).

A first physical-chemical characterization of hyaluronan dates back to the 1950s and 1960s.[15] The morphology of isolated HA molecules in solutions was described as a stiffened random coil, which occupies a very large volume. The reason for stiffening was proposed to be in part due to hydrogen bonding between adjacent monosaccharides combined with some effect of mutual electrostatic repulsion between carboxyl groups.[16] Later it was argued that self-association of HA through hydrophobic patches chains might play an important role in determining the physico-chemical properties of HA solutions, based on NMR and rotary shadowing electron microscopy data.[13, 17] However, this view of HA molecules has been difficult to reconcile with a range of recent data on the self-diffusion of hyaluronan, which show that no inter-chain associations are required to explain HA solution properties.[18, 19] The current picture of solution properties of hyaluronan is given in recent reviews by Day and Sheehan, and by Hardingham[20, 21], where the molecule is better described as a highly organized extended dynamic random coil, which can locally undergo sharp kinks, bends and folds.

HA is a megadalton molecule and its physico-chemical and biological properties are dependent on its molecular weight. The conformation and properties of HA can also be affected by the local environment (e.g. ionic strength), tethering to surfaces, exposure to mechanical forces, and the presence of other biomolecules that interact with HA (so-called hyaladherins).[22, 23]

HA is predominantly present in the ECM and interacts with a variety of ECM molecules. Newly synthesized HA molecules can interact with several cell surface receptors (such as CD44 and RHAMM). This interaction mediates important physiological processes, including signal transduction, formation of pericellular coats and receptor-mediated internalization.[14, 24] Due to its particular physico-chemical properties, HA can act as a space filler and or lubricant. HA is also known to play a role in physiological and pathological processes, including embryological development, inflammation,[25] and tumor development. On the cellular level, it affects cell proliferation, differentiation, migration and adhesion.[24] In particular, cancer cells have been shown to exhibit altered mobility in the presence of excess hyaluronan.[26] The mechanical properties of HA and its assemblies have been proposed to be functionally important.[27]

HA-binding proteins called hyaladherins mediate many aspects of cell behavior such as cell migration, attachment and metastasis performed by HA.[8, 28] Most hyaladherins share a common structural binding domain called the link module. The link protein, for example, which is commonly found in cartilage, is comprised of an immunoglobulin domain followed by two contiguous link modules, which can both bind independently to HA. The extracellular hyaladherins aggrecan, versican, neurocan and brevican form a hyaladherin sub-family. These proteins (or proteoglycans) are rich in chondroitin sulphate and can form large complexes with HA that are stabilized by link

protein.[29] In cartilage, the complexes formed by aggrecan and HA provide load-bearing function in articular cartilage. Other proteoglycan-HA complexes provide elasticity to blood vessels, and contribute to the structural integrity of tissues such as skin and brain.[30]

1.4 Aggrecan

Aggrecan is the largest proteoglycan, and can be found predominantly in cartilage at high concentrations. It is comprised of a core protein, three globular domains (G1, G2, and G3) and two types of glycosaminoglycan (GAG) side chains: chondrotin sulfate (CS) and keratan sulfate (KS). The KS and CS chains are tethered to the core protein, which is situated between the G2 and G3 domains and assemble into a bottle brush like structure (Figure 1.3B).[31] An inter-globular domain (IGD) connects G1 and G2 domains.

The ability of articular cartilage to resist compression is primarily attributed to the CS GAG chains.[30] A macroscale interpretation, independent of molecular structure is that the high density of fixed negative charges of the sulfate and carboxylate groups on GAG chains creates a repulsion force that must be neutralized by mobile positive ions in the surrounding fluid. The higher concentration of ions in the tissue compared to outside the tissue leads to swelling pressure and draws water into the tissue. In the absence of any applied load the swelling tendency of the proteoglycans is restrained by the collagen fiber network, thus giving rise to the compressive behavior of cartilage.[32] At the molecular scale, it is the electrostatic double layer repulsive interaction forces between the rod-like GAG chains that have been proposed to give rise to compressive stiffness.[33]

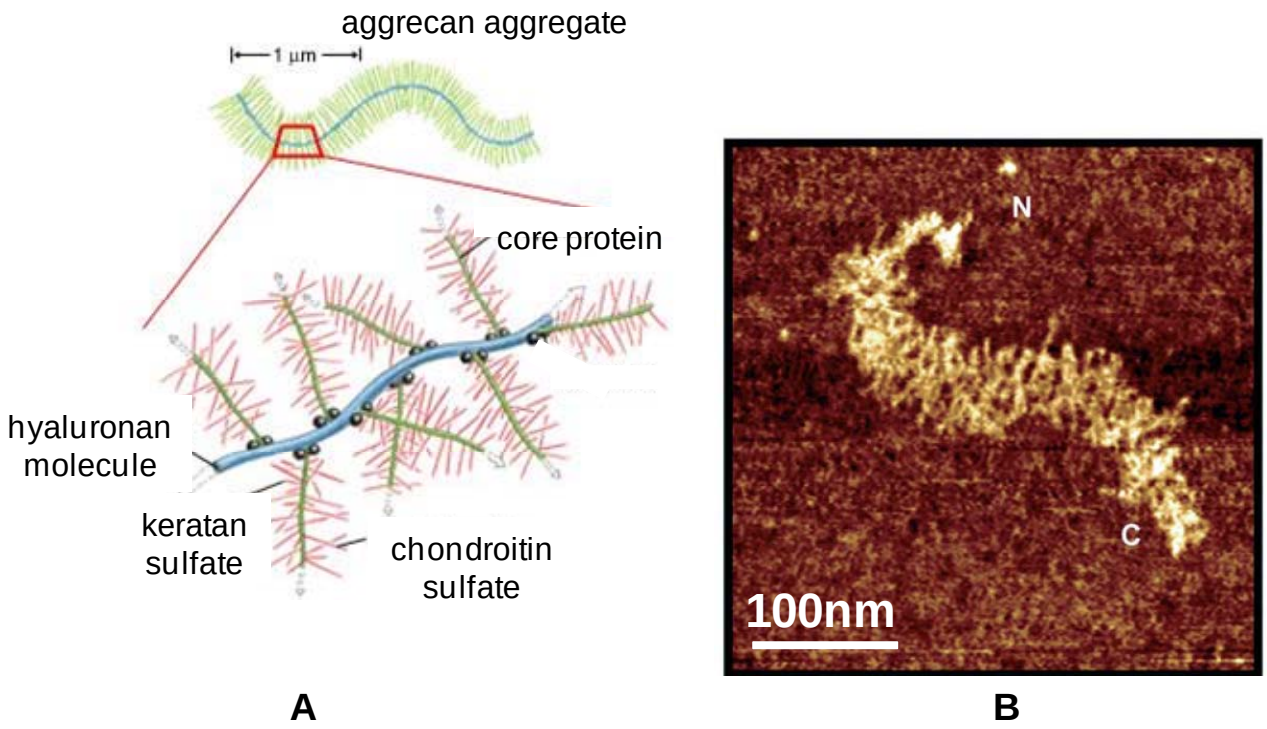

Figure 1.3 (**A**) Schematic illustration of an aggrecan-HA complex and the involved intermolecular associations.[34] HA is drawn in blue, link protein in black, the peptide chain of aggrecan in green and the GAG chains of aggrecan in red. (**B**) Atomic force microscopy image of an isolated molecule of mature nasal aggrecan.[35] The N and C termini are marked. Individual GAG chains can be clearly distinguished.

In cartilage, aggrecan interacts with HA through its N-terminal G1 domain. Aggrecan is non-covalently bound to hyaluronan. This interaction is stabilized by link protein, a protein that binds non-covalently to both HA and the G1 domain of aggrecan.[36] The interaction of multiple aggrecan-link protein complexes with a single megadalton HA chain can give rise to large supramolecular complexes (Figure 1.3A). It has been shown more recently that the aggrecan C-terminal G3 domain can interact with certain matrix proteins containing epidermal growth factor repeats.[37] The KS rich region has been shown to bind with high affinity to collagen,[38] which may play a role in organizing ECM components. In cartilage, the aggrecan aggregates are interspersed with the type II collagen network. Typically, the aggrecan macromolecules are compressed to 20-30 % of the volume they would occupy in physiological solvents when fully expanded. This increases the charge density in the GAG side chains. This increased charged density as well as the numerous partially constrained GAG chains create a swelling pressure on the collagen network that resists compressive loads, a necessary physical property of cartilage.[39]

1.5 Model systems

The PCM is highly hydrated and composed of dynamic assemblies of proteoglycans, polysaccharides, and proteins. Because PCMs are highly hydrated, exhibit a low degree of order and are highly dynamics, direct information about the supramolecular structure is difficult to obtain *in vivo*. For mechanistic studies, for example, to understand how a subset of molecular species and their inter-molecular interactions gives rise to the physico-chemical properties of PCMs, *in vitro* model systems would be useful.

Supported lipid bilayers (SLBs) constitute a surface-based model of the cell surface.[40, 41] Several pathways for the formation of SLBs have been established and the kinetics of formation are described elsewhere.[42, 43]

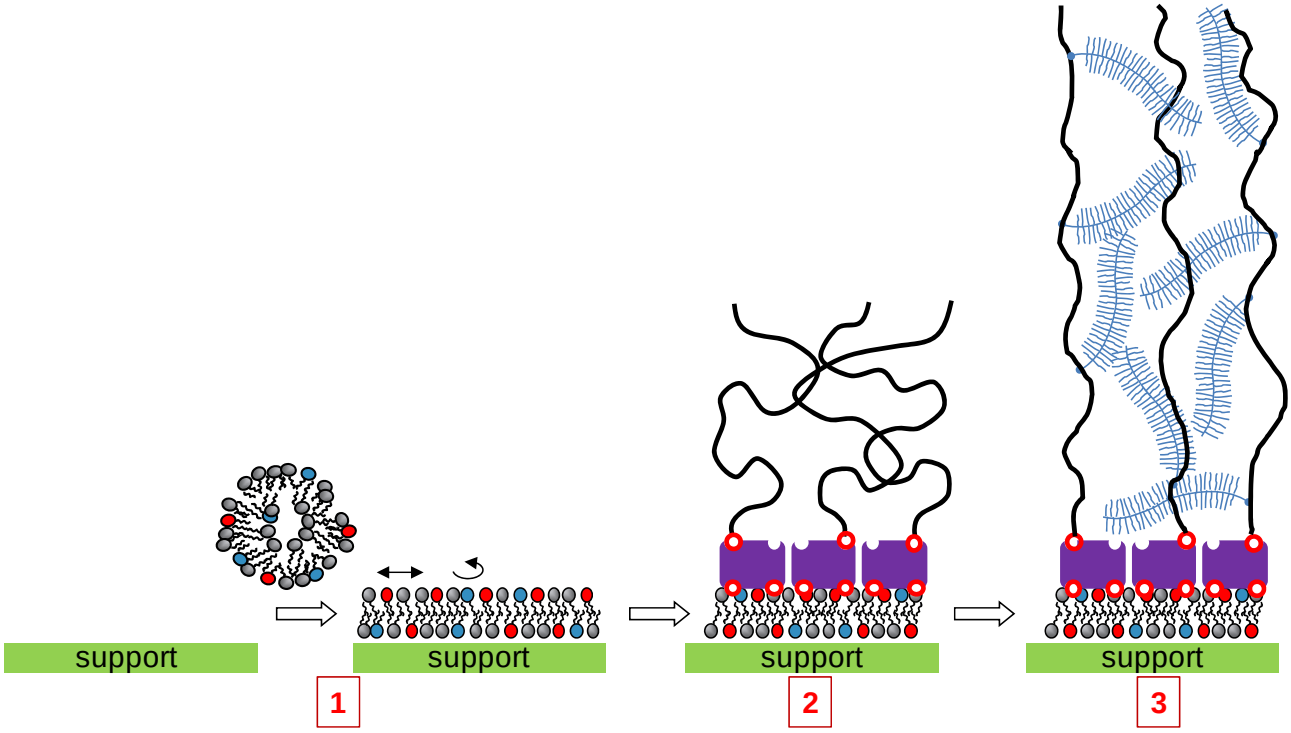

Figure 1.4 Scheme of the formation of SLB based model system resembling HA-rich pericellular coats. (1) Small unilamellar vesicles (containing a small fraction of biotinylated lipids) adhere to a solid support, subsequently rupture and eventually form a confluent SLB.[42] (2) Biotinylated HA is grafted via a streptavidin linker to the SLB. (3) HA-aggrecan complex.

In this work, we make use of SLBs as an *in vitro* platform to graft HA chains, Such a tailor-made model system of hyaluronan-rich pericellular coats offers the possibility to study the relationship between the composition, supramolecular structure and dynamics, physicochemical properties, and biological function of HA assemblies in PCM.[44] In this model system, the HA molecular weight is well-controlled, and the physicochemical properties of HA films as a function of external cues

(hyaluronan binding proteins) become accessible to quantitative investigation by surface-sensitive biophysical techniques.[44, 45]

1.6 Characterization techniques

1.6.1 Atomic force microscopy

Atomic force microscopy (AFM) is a scanning probe technique. Since its invention in 1986,[46] AFM has developed very rapidly and is now used for a plethora of applications in many fields of science. In the past two decades, besides surface topography mapping, AFM has been used to measure a variety of surface and material properties, such as chemical, electrical, magnetic and mechanical properties. In particular, because AFM can be applied in liquid, it has been extensively used to study a variety of biological objects in their native aqueous surrounding.[47]

The principle of AFM is shown in Figure 1.5. The interactive force between the probe and the surface is detected by measuring the deflection of the cantilever using the optical lever technique, where light from a laser source is focused on the cantilever and reflected light is collected on a photodetector, a 4-quadrant photodiode. The readout of the 4-quadrant photodiode can be related to the cantilever deflection, and the cantilever deflection in turn is a measure of the force exerted on the probe, when it interacts with the sample surface.

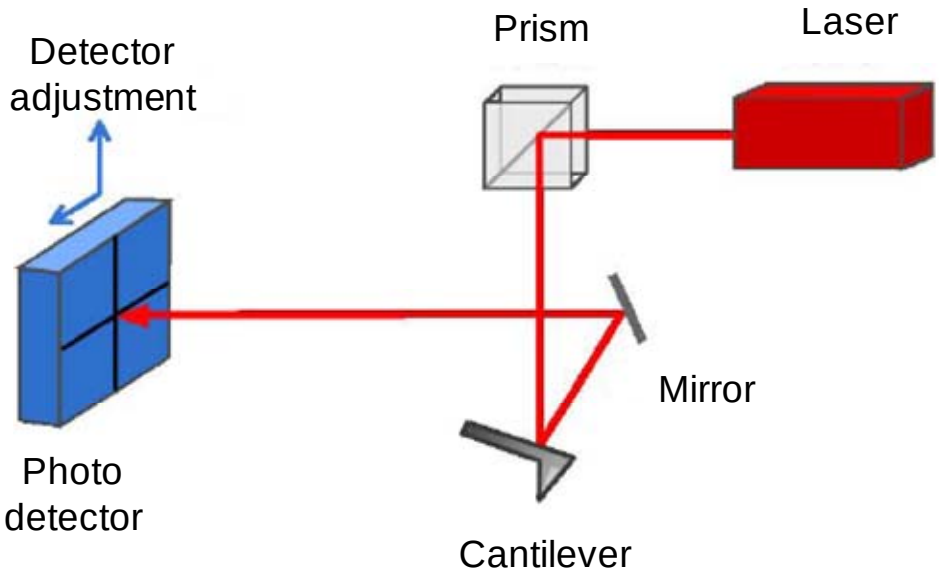

Figure 1.5 Scheme of the optical lever detection setup used to detect cantilever displacements in a typical AFM. (Image taken from NanoWizard AFM User Manual of JPK AG, Berlin, Germany).

When the tip is pushed to the sample surface, the cantilever bends upwards. If the cantilever bending is given by δ, then the force, F exerted on the sample surface is $F = k\delta$, where k is the

spring constant of the cantilever. Through modifying the sharpness and the chemistry of the tip, AFM offers various possibilities in force measurement. A sharp AFM tip usually has an apex radius as small as a few nanometers. In single molecule force spectroscopy experiments, for example, a receptor-coated AFM tip is brought into contact with a sample surface coated with corresponding ligand molecules, the tip adheres and picks up a single molecule from the sample surface. When subsequently retracting the tip from the surface, the interacting molecules are stretched and/or unfolded until receptor and ligand separate again. From a statistical analysis of the recorded force-distance traces, information about the strength and the type of ligand-receptor interaction and/or structural and mechanical information about the molecule under investigation can be obtained.[48, 49]

1.6.1.1 Colloidal probe AFM

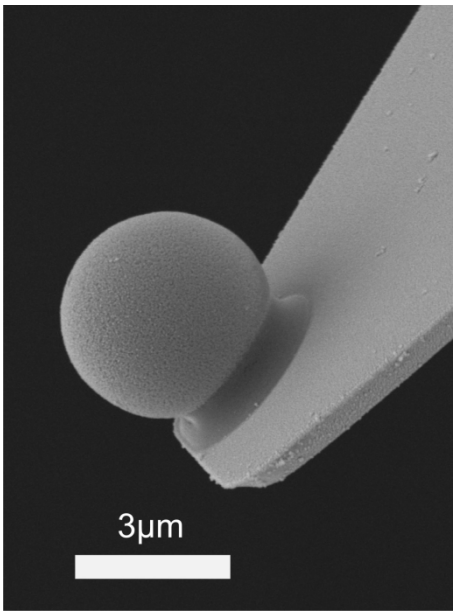

Figure 1.6 Scanning electron microscopy image of a colloidal sphere attached to the apex of a tipless AFM cantilever.[50]

Colloidal probe AFM developed independently by Butt[51] and Ducker et al[52] is a popular and versatile technique for investigating the mechanical properties of thin films and macroscopic materials.[53-56] The name "colloidal probe technique" was coined by Ducker et al in 1991. Colloidal probe AFM measures the forces, with pN resolution, that act on a nanometer or micrometer-sized spherical probe as it interacts with the material of interest. To this end, the spherical particle, a polystyrene latex particle in our case, is glued to the apex of an AFM cantilever (as described in detail in Chapter 6).

An advantage of colloidal probes over conventional AFM tips is that their shape is well defined. This makes the geometry of interaction between probe and sample well-controlled and improves the

reproducibility and comparability of data taken with different probes. In addition, interactions can be quantified with improved sensitivity because the total force increases.[55]

Force measurements using colloidal probe AFM on adsorbed and grafted polymer layers have been reported.[57] Effects of solvent, ionic strength, pH and temperature on end-grafted films have been probed, giving insight into the characteristics of different conformational regimes, such as the brush or mushroom regime (see Chapter 1.7).[58-61]

1.6.1.2 Force measurements by AFM

The applied force *F* can be extracted from a deflection-displacement curve, which is measured when the probe is first approached towards and then retracted from the sample surface (Figure 1.7). The distance *d* may be defined as the difference between the piezo displacement and cantilever deflection in units of length.

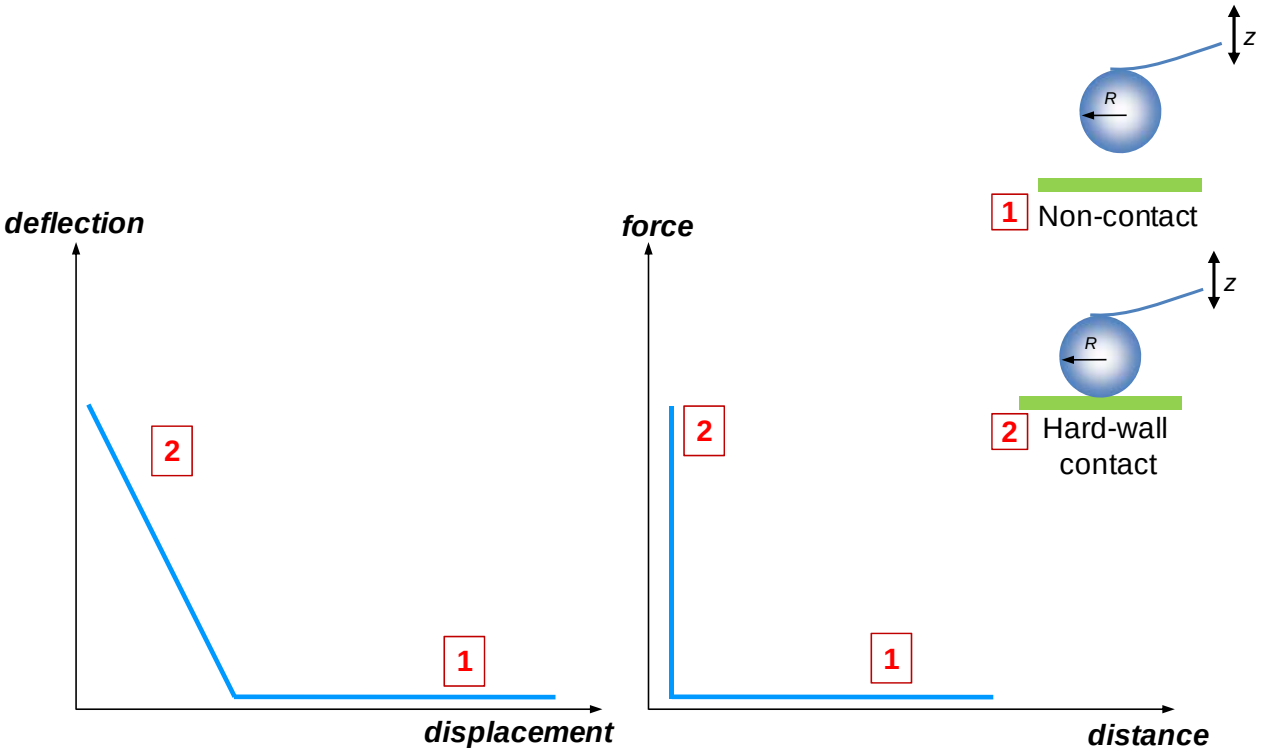

Figure 1.7 The sketches show the probe interaction with the surface in the simple case were both probe and surface are rigid and do neither attract nor repel each other. Deflection, which is the measure of cantilever bending, is converted into force and the displacement of the *z*-piezo into distance.

When working with soft and compressible films, the force curve shows a gradual increase in force instead of the sharp onset of the interactions seen on hard surfaces (Figures 1.7 and 1.8). For thin and soft films on a hard surface, at large deflection, the hard-wall contact regime may be approached when the tip indents the sample enough such that the mechanical properties are

dominated by the supporting surface below. Hysteresis between the approach and retract curves may be seen, if the sample is not perfectly elastic or if adhesion between probe and sample occurs.

The absolute distance *d* between the probe and the surface on which the sample is deposited can be readily determined from AFM data, when the AFM tip can be brought into direct contact with the surface. In the case of thin polymer films, this is usually not the case, even though it is often desirable to be able to relate the response to compression to the film's thickness and to the precise location of the probe within the film. This is a fundamental limitation of colloidal probe AFM. For the characterization of polymer films, the consequence is that only relative changes in distance are accessible to experiment whereas the absolute probe-substrate distance remains unknown. This urges the need of complementary techniques that can measure the absolute probe-substrate distance while not destroying the sample surface.

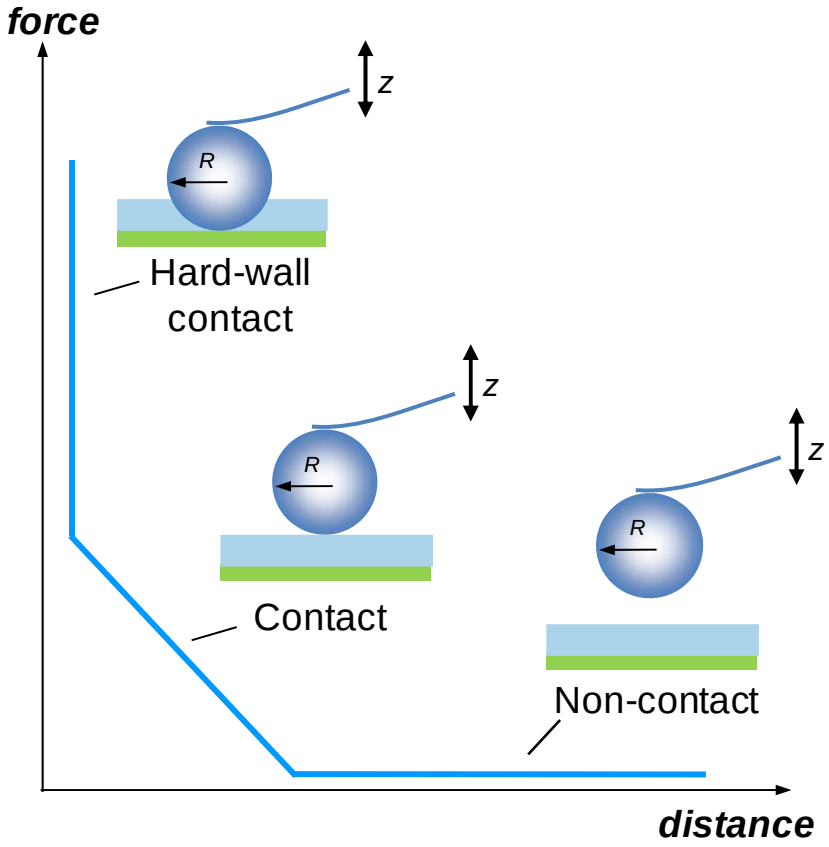

Figure 1.8 Schematic representation of a force *vs* distance plot on a soft compressible sample. The probe indents the sample, indicated by a simplified linear increase in the force. At very strong compression, hard wall contact may be reached.

To compare force curves taken with probes of different radius, it is useful to normalize the forces by the radius. The reason becomes apparent from the so-called Derjaguin's approximation. It can be shown that the interaction force between a flat surface and a sphere with radius *R* is related to the interaction energy *E* per unit area between two parallel flat surfaces as:[62]

$$F(d) = 2\pi R\, E(d), \qquad [1.1]$$

where d is the separation distance between the two surfaces. Rewriting the equation, we get:

$$\frac{F(d)}{R} = 2\pi\, E(d). \qquad [1.2]$$

Hence, through normalization of the forces, a measure for interaction energies can be obtained that is independent of the interaction geometry.

1.6.2 Reflection interference contrast microscopy

Optical interferometry is certainly not new, and has been in used to study distances, displacements and vibration, for several hundred years. Interference, the basic principle of interferometry is a well known optical phenomenon caused by the superposition of light waves. Commonly seen examples of interference in our daily life are the colors of an oil slick or a soap bubble. In the latter case, light is reflected at the two interfaces of the soap film. As the thickness of the film changes, the optical path difference between the two reflected light beams changes. In visible light, since the wavelength is small (half a micrometer in case of green light), very small changes in the optical path differences can produce measurable changes in the intensity of the interference pattern. As a result, optical interferometry permits very accurate measurements of distances through the analysis of interference fringes.

Reflection interference contrast microscopy (RICM) is an interferometric technique that was initially devised to study the interaction of cells with a planar glass substrate. Adam Curtis in 1960s introduced this technique to cell biology using the name interference reflection microscopy (IRM).[63] In his work, Curtis used this technique to characterize the distance between the glass substrate and the underside of a living cell. Later, Ploem et al greatly improved the method by introducing the antiflex method to enhance the image contrast.[64, 65] Considerable refinements in the image analysis continued since then, but a lack of knowledge of the optical properties of the objects under study, in particular the presence of many partially reflecting interfaces in living cells, pose a challenge in the quantitative analysis of the RICM images to study cell-substrate interactions.[64]

Work by Sackmann and co-workers starting in the 1980s demonstrated that RICM with improved contrast has excellent potential to study inter-surface distances between a planar transparent substrate and a spherical object hovering on top of it.[66, 67] In this case, a pattern of concentric rings, known as Newtonian rings, will form. From this interferometric pattern, the distance between sphere and substrate can be extracted with a resolution up to 2 nm.[64] In addition, the lateral position of the bead can be determined with similar resolution. In recent years, the development of dual and triple wavelength RICM has provided a mean to deal with ambiguities in distance determination that are intrinsic to the periodicity of interferometric responses. This has

enabled the determination of absolute distance measurements with accuracy levels down to ±3 nm over a distance range of 1 micrometer.[44, 68]

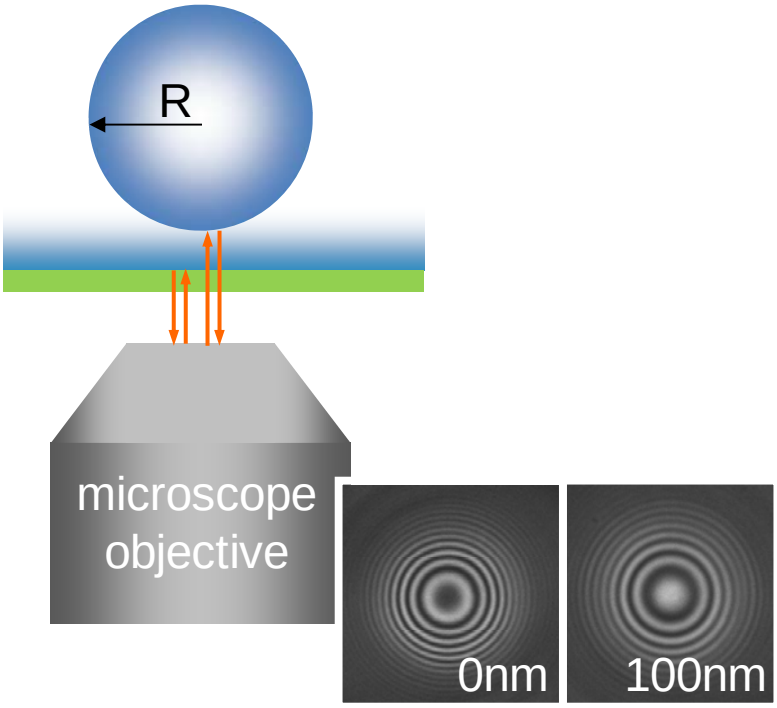

Figure 1.9 Schematic representation of the RICM working principle. The incident and reflected light beams are illustrated by orange arrows. The interferographs shown are taken with a colloidal probe at approximately 0 and 100 nm, respectively, distance from the substrate.

The basic principle of colloidal probe RICM is shown in the Figure 1.9. The incoming light is first partly reflected at the glass/medium interface. The transmitted light is further partly reflected at the probe/medium interface. The two reflected beams interfere with each other, giving rise to a Newtonian ring pattern with intensity maximum (I_{max}) and intensity minimum (I_{min}). In a simple approximation, where the incident and reflected rays are parallel to the optical axis, the relation between intensity distribution and distance $d(x,y)$ is given by:

$$I(d(x,y),\lambda) = I_{min} + I_{max} + 2\sqrt{I_{min}I_{max}}\cos\left[\frac{4\pi n d(x,y)}{\lambda} + \varphi\right] \qquad [1.3]$$

where $d(x,y)$ is the *distance* at a given lateral position with coordinates x and y. n is the refractive index of the medium and φ is the phase shift of the reflected light from the probe and λ is the wavelength of light.

For the case, where the intensities for two wavelengths (for example green and blue light) are available, then a parametric representation of the blue light intensity is given by:

$$I_{blue} = D_{\text{green}} - S_{\text{blue}} \cos\left(\frac{\lambda_{\text{green}}}{\lambda_{\text{blue}}}\right) \cos^{-1}\left(\frac{D_{\text{blue}} - I_{\text{green}}}{S_{\text{green}}}\right) \quad [1.4]$$

where $D_{\text{green}} = I_{\text{green}}^{\max} - I_{\text{green}}^{\min}$, $S_{\text{green}} = I_{\text{green}}^{\max} + I_{\text{green}}^{\min}$, and $D_{blue} = I_{\text{blue}}^{\max} - I_{\text{blue}}^{\min}$, $S_{blue} = I_{\text{blue}}^{\max} + I_{\text{blue}}^{\min}$. Figure 1.10 displays the parametric plot of two wavelengths.

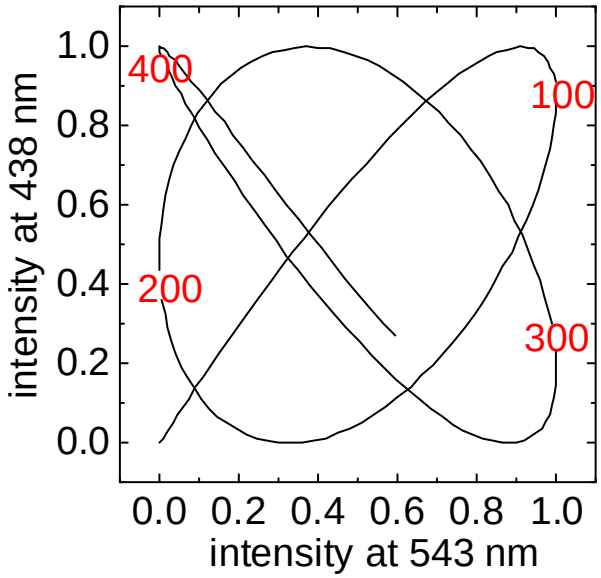

Figure 1.10 Parametric plot of blue light intensity *vs* green light intensity of RICM data over a thickness range of approximately 500 nm. For a given pair of intensities (at both wavelengths) a unique *d* can be assigned for most distances. The numbers in red indicate *d* in nanometers. The maximal intensities are normalized to 1.0.

For reflecting objects of known geometry, the distance can be determined from extrema in the fringe pattern. In particular, for spherical beads, the bead substrate *distance d* can be calculated from radially averaged intensity profiles arising from the circular symmetry of the interferographs arising from the spherical symmetry[46] of the beads. *d* can be derived from the radial position, $x_{\text{ext}}^{(i)}$, of a selected extremum, *i* in the intensity profile through:

$$d_{\text{min}}^{(l)} = \frac{\lambda l}{2n} - R + \sqrt{R^2 - x_{ext}^{(i)^2}} \qquad \text{if the extremum } i \text{ is minimum} \qquad [1.5]$$

and

$$d_{\text{max}}^{(l)} = \frac{\lambda(2l+1)}{4n} - R + \sqrt{R^2 - x_{ext}^{(i)^2}} \qquad \text{if the extremum } i \text{ is maximum} \qquad [1.6]$$

where *R* is the probe radius and *l* is fringe order.

As can be seen from the last two equations, the radius *R* of the bead has a strong influence on the determination of *d*. Usually bright-field microscopy is used to estimate the bead radius. Accurate determination of the absolute probe radius by bright field microscopy is a non-trivial task, because the optical image of the bead is affected by the refraction of light at the bead-solution interface. In

addition, the exact position of the interference fringes does also depend on the focus position of the microscope objective. To correct for the errors in the determination of *d* due to improper focus position and probe radius we have established a *novel* method that relies on the determination of an effective bead radius through correlation of AFM and RICM data. This method will be decribed in detail in Chapter 2.

1.6.3 Quartz crystal microbalance with dissipation monitoring (QCM-D)

The quartz crystal microbalance (QCM) is a surface-sensitive acoustic wave technique known to measure surface-bound masses (per unit area). It measures the changes in the resonant frequency of a quartz crystal disc sandwiched between two metal electrodes. Application of an external alternating electric field causes an oscillatory shear deformation of the quartz disc due to its piezoelectric nature. Upon deformation, the two disc surfaces move in parallel but in opposite direction, thereby generating acoustic waves in the direction perpendicular to the sensor surface. Resonance is excited when the frequency of the applied AC voltage is close to the resonant frequency of the crystal (Figure 1.11). The resonant frequency depends on the thickness of the quartz crystal and is typically on the order of a few MHz.

The dissipation factor that accounts for the viscous and elastic contributions to the *frequency* change in liquid phase is addressed by QCM-D, initially developed by Rodahl and co-workers in the 1990s.[69] The technology, commercialized by Q-Sense in 1996 has been widely used, for example, to study the self-assembly of solid-supported lipid bilayers (SLBs).[42, 70, 71]

The adsorption of proteins/polymers at the liquid/sensor interface can be followed by the changes in the *frequency*, and changes in the *dissipation* can be related to the mechanical properties (e.g. viscoelasticity) of the adsorbed material. The QCM-D allows to measure changes in *frequency* and *dissipation* at multiple overtones (n = 3, 5…) with sub-second time resolution.

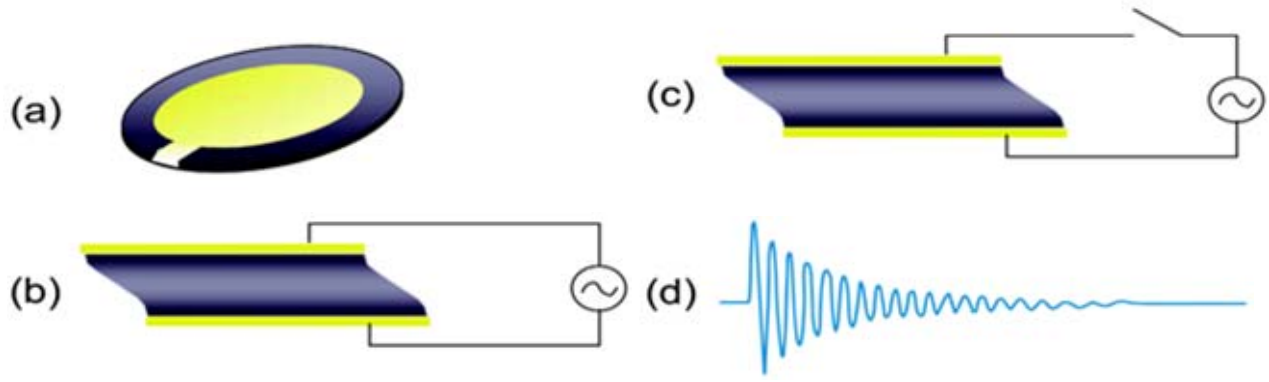

Figure 1.11 Schematic representation of (a) typical QCM-D sensor sandwiched between gold electrodes. (b) Shear deformation of the crystal with application of alternating current. (c) Switching off the circuit. (d) Oscillatory decay of the crystal.

1.6.4 Spectroscopic ellipsometry

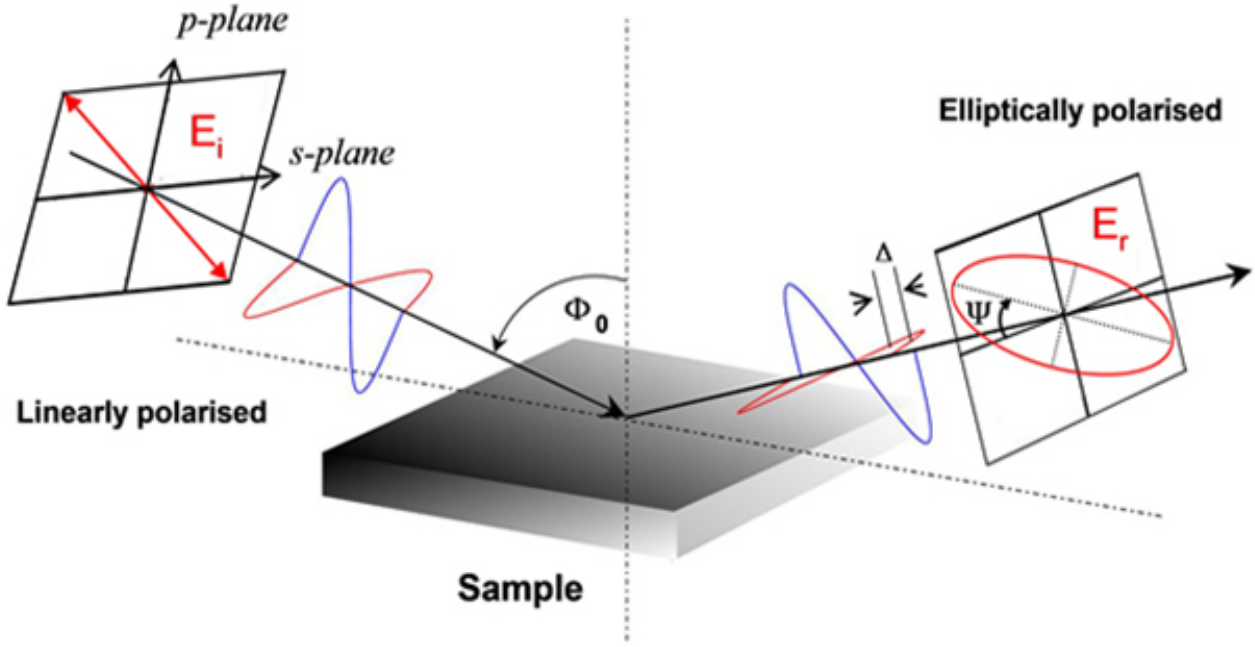

Figure 1.12 Cartoon showing the light path in a typical ellipsometer setup. The basic principle relies on the fact that the polarization of light changes upon reflection from a surface, and that the polarization is very sensitive to the presence of thin transparent layers at the interface.[72]

Spectroscopic ellipsometry is an optical technique in which the changes in polarization upon reflection of light from a sample surface are determined. The reflection is in general associated with changes in the amplitude and in the phase difference of different components of a polarized light wave. By determining the state of polarization on both the bare surface and a surface covered by a layer of biomolecules, it is possible to convert the change in polarization into a refractive index and a thickness of the adsorbed layer by using an optical model of the surface, adsorbed layer(s) and the solution.

The reflectance and transmission of polarized light at an interface is quantitatively described by the Fresnel formalism. The Fresnel reflection coefficient r defines the ratio of the amplitude of the reflected wave to the amplitude of the incident wave. The reflection coefficients of the p- and s-polarized components are r_p and r_s. The fundamental equation of ellipsometry is:[73]

$$\tan \Psi e^{i\Delta} = \frac{r_p}{r_s} \qquad [1.7]$$

The quantities Ψ (psi) and Δ (delta) are measured directly by the ellipsometer where, $\tan \Psi$ is defined as the ratio of the amplitude between p- and s-polarized components of light upon reflection and Δ is defined as the phase difference between them. The information about the film thickness (L)

and the refractive index (n) of a surface adlayer is given by fitting an appropriate layer model to the experimental data (Figure 1.13). For biomolecular films in aqueous solution, the areal biomolecular mass density can then be obtained from n and L, with a sensitivity of about 1 ng/cm^2, using de Feijter's equation.[74]

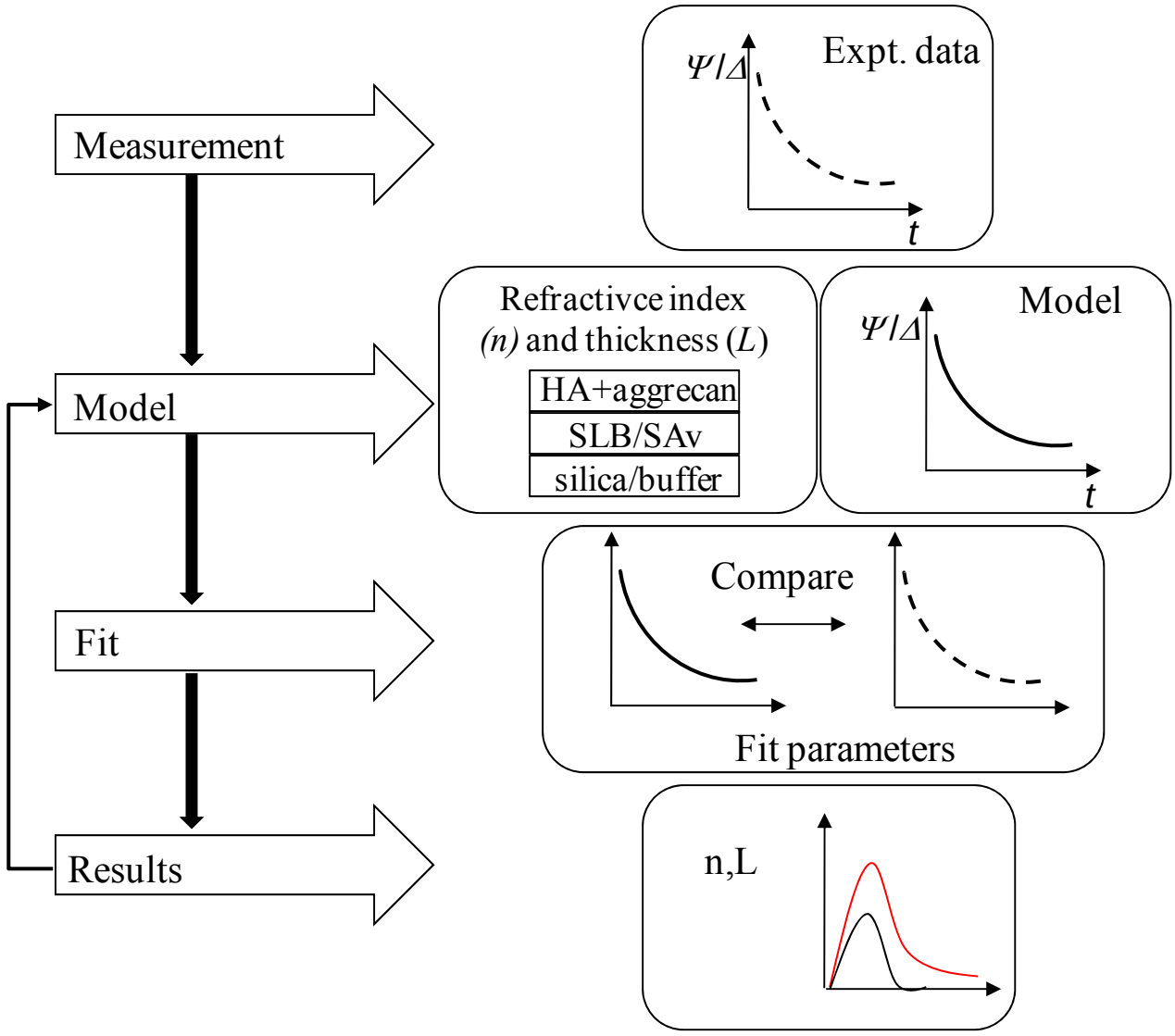

Figure 1.13 Flow chart for an ellipsometry experiment with data analysis. The optical properties and thickness of adlayers are obtained by fitting a model to the experimental data (Ψ and Δ).

The hyaluronan films under study in this thesis represent unusually thick monomolecular layers. For these films, we have applied a modified ellipsometric model that explicitly considers the density profile within the film. Such an approach became possible, and necessary to adequately model the data, because the film thickness approaches (or even exceeds) the wavelength of the probing light. This approach is applied in Chapter 3 and described in detail in Chapter 6.

1.7 Basic physical concepts of polymer brushes

1.7.1 Polmers at interfaces

Polymers end-grafted to surface are of great interest due to their versatile applications in adhesives, biosurfaces, lubrication and polymer coatings.[75-77] Grafted polymer chains can adopt three distinctly different conformations as shown in the Figure 1.14. The chosen conformation depends on the magnitude of the radius of gyration of the polymer R_g in solution compared to the mean distance between grafting sites s. If s is greater than R_g, a so-called mushroom like conformation is adopted, provided that the interactions between the polymer segments and the surface are weak. Here, the conformation of the grafted chain is similar to the conformation of a free isolated chain in solution. If the polymer segments are attracted by the surface, than the chain assumes a flat, pancake-like conformation. If s is smaller than R_g, then the crowding of polymer chains will lead to stretching of the chains due to inter-segment repulsion, and a brush-like conformation can be observed. By decreasing the spacing between grafting points, polymers chains transit from mushroom or pancake conformations to the brush conformation.

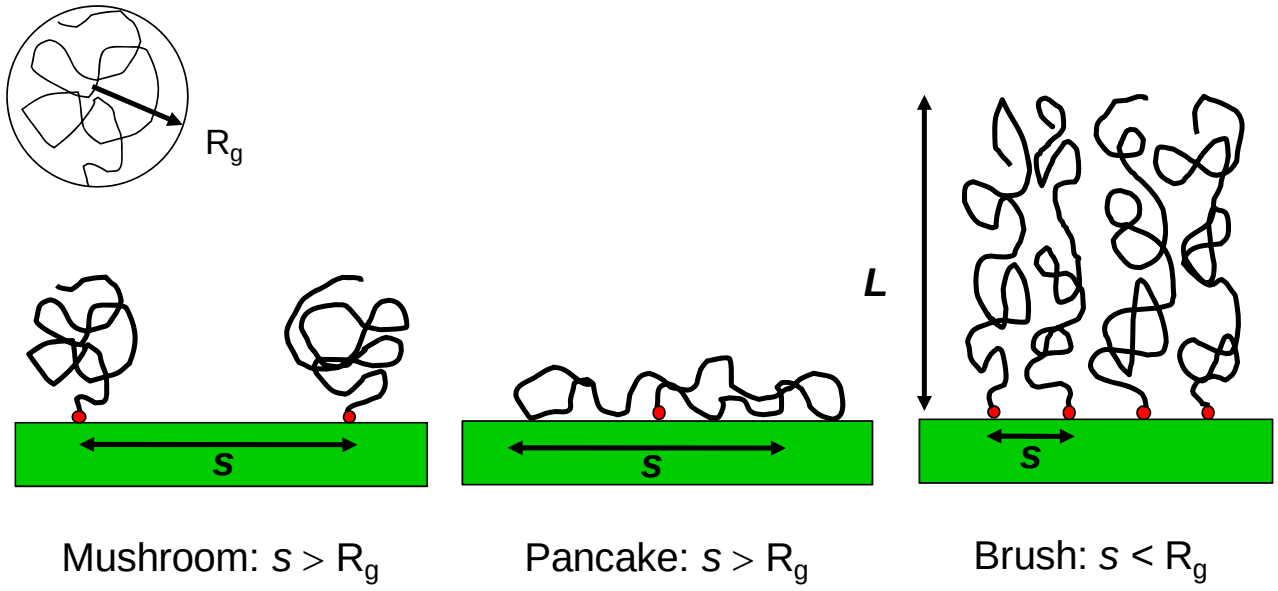

Figure 1.14 Schematic representation of three different conformations a polymer might adopt when grafted onto a flat interface.

Alexander and de Gennes gave a first theoretical description of polymer brushes grafted onto a flat surface and immersed in a good solvent. The equilibrium thickness L of the tethered chains in good solvent, using Flory arguments, is given by the energy balance between the interaction energy (osmotic repulsion) between the statistical segments on the one hand and the energy of chain stretching on the other.[78] The Alexander-de Gennes (AdG) brush model assumes that the free ends of the (monodisperse) chains are all located at the same distance L away from the grafting surface.

This assumption implies that all chains are stretched equally and that the segment density profiles is described by a step-function (Figure 1.16). In the AdG model,[79] chains are replaced by a series of virtual blobs as depicted in Figure 1.15. The concept of blobs provides a separation of length scales: within the blobs the polymer can be approximated as behaving as a free unstretched polymer whereas the string of blobs is fully stretched. For planar brushes, the average distance between neighboring grafting points dictates the size of the blobs. The equilibrium layer thickness L is then given by:

$$L \propto Na^{5/3}s^{-2/3}, \qquad [1.9]$$

where N is the number of statistical monomer units of length a. It is noted here that there is a linear dependence of L on the chain size. Alexander and de Gennes is based on scaling theory, this equation is only accurate to within a prefactor of order unity.

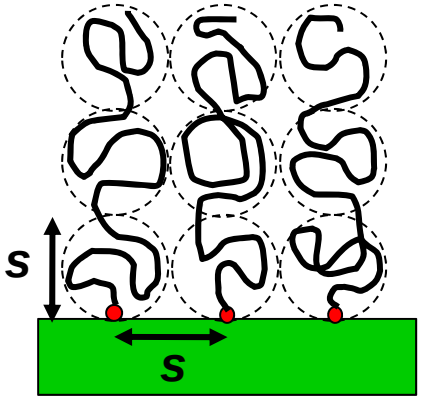

Figure 1.15 Schematic illustration of the scaling model by Alexander and de Gennes for a grafted polymer film. Each chain is matched to a string of blobs each of size s. The model assumes monodisperse polymer chains and that all free chain ends are located at the outer edge of the brush. This implies a constant polymer density throughout the brush (box profile).

Later Milner, Witten, Cates[80, 81] and Zhulina and co-workers[82, 83] independently used another approach, self-consistent mean-field theory, to describe dense polymer brushes. This approach takes advantage of the fact that in a sufficiently stretched system, local fluctuations around monomers can be neglected to a first approxim*ation. They relax the assumption that the free ends of the chain are positioned exclusively at the extremity of the brush and instead determine their distribution self-consistently. In this case, the expressions for free energy also include all numerial prefactors. A key prediction from this theory is that the chain segment density profile is parabolic (Figure 1.16).

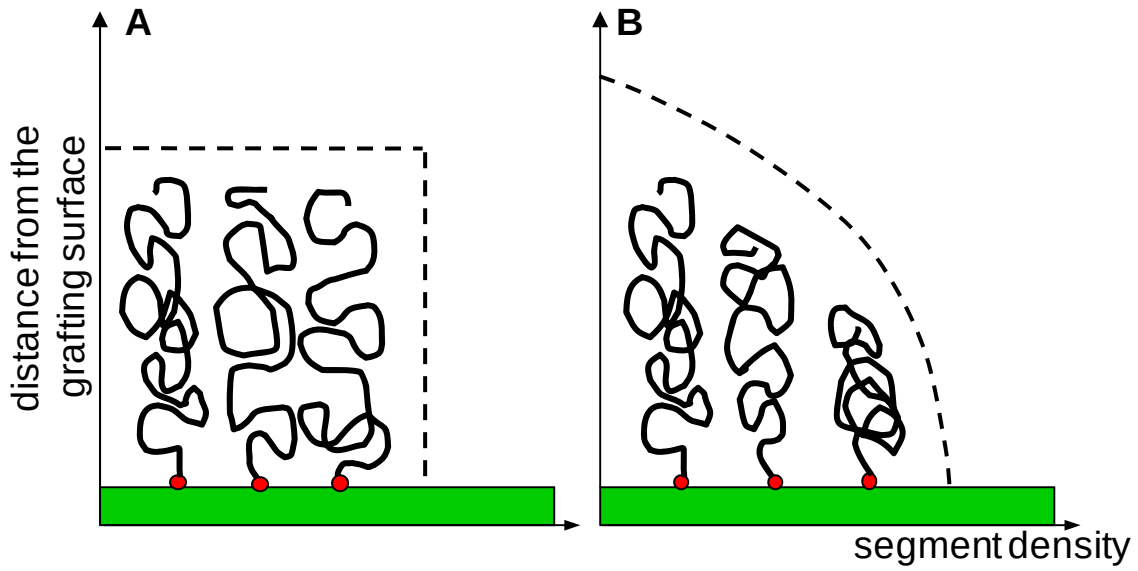

Figure 1.16 Distribution of the polymer segment density profiles in the polymer brush. (**A**). step function profile or box profile where the polymer segment density is uniform, and (**B**). represents the parabolic profile.

The approach with a parabolic profile incorporates the stretching energy through a Gaussian stretching term, which implies that the chains would be infinitely extensible. This is expected to be a good approximation for moderate chain distortions, but it is not appropriate when the thickness of the brush approaches the chain contour length (as discussed in detail in Chapter 4). In spite of the differences between scaling and self-consistent field theories, their common use of a Gaussian stretching term and a second virial coefficient excluded volume term in the free energy results in equivalent scaling of the thickness of the brush.

1.7.2 Polyelectrolyte brushes

The situation for brushes of charged polymer chains - polyelectrolyte (PE) brushes - is different; in this case different scaling behaviors appear. The behavior of a PE brush depends on the charge density on the polymer chain and the ionic strength of the surrounding solution, in addition to the grafting density. If charge density and graft density are sufficiently high and the ionic strength is low, the brush thickness scales linearly with N, but is independent of the grafting density.

This situation is referred to as osmotic brush. Here, the concentration of counterions inside the brush is greater than the external salt concentration in solution. The driving force of chain stretching is the osmotic pressure of the counterions. In the osmotic regime the balance between the elastic pressure generated by the stretching of chains and the counterion osmotic pressure leads to the equilibrium thickness of the uncompressed brush. The graft density does not affect the balance

between the two pressures, so the brush thickness is independent of graft density. The scaling for the thickness in the osmotic regime was presented by Borisov et al. and by Pincus:[84, 85]

$$L \propto Na\alpha^{1/2} \quad [1.10]$$

When the external salt concentration c_s exceeds the counterion concentration in the brush, the added ions will diffuse into the brush and screen the repulsive electrostatic interactions between chains. As a result, the brush thickness decreases, following the power law.

$$L \propto c_s^{-1/3} \quad [1.11]$$

This regime is called salted brush regime. The response of PE brushes to added electrolytes has been investigated experimentally and the predicted power law dependence has been experimentally validated in a few cases.[86, 87] At very high salt concentrations, the charge screening becomes so strong that the intrinsic excluded volume of the polymer chain becomes important and the brush approaches the behavior of a neutral brush. This regime is called the *quasi*-neutral brush regime.[88]

A quantitative comparison between experimental data for HA brushes and polymer and polyelectrolyte brush theory is the subject of Chapter 4. This chapter also contains a more detailed description of the different theoretical models. In particular, effects of finite chain stretching, intrinsic chain stiffness and excluded volume, which have been neglected here but are all important for the particular case of HA, are explicitly treated.

2. Combining colloidal probe atomic force and reflection interference contrast microscopy to study the compressive mechanics of hyaluronan brushes

We describe a method that combines colloidal probe atomic force microscopy (AFM) and reflection interference contrast microscopy (RICM) to characterize the mechanical properties of thin and solvated polymer films. When analyzing polymer films, a fundamental problem in colloidal probe AFM experiments is to determine the distance at closest approach between the probe and the substrate on which the film is deposited. By combining AFM and RICM in situ, forces and absolute distances can be measured simultaneously. Using the combined setup, we quantify the compressive mechanics of films of the polysaccharide hyaluronan that is end-grafted to a supported lipid bilayer. The experimental data, and comparison with polymer theory, show that hyaluronan films are well-described as elastic, very soft and highly solvated polymer brushes. The data on these well-defined films should be a useful reference for the investigation of the more complex hyaluronan-rich coats that surround many living cells.

2.1 Introduction

Highly solvated polymer films have naturally evolved as multifunctional interfaces in a number of biological systems, for example as mucosal films in the lungs, the gastro-intestinal or reproductive tracts, as cellular coats around many cells[89] or in bacterial biofilms. Surface-confined polymer films are also becoming increasingly popular in a variety of applications in (bio)technology, as anti-fouling[75] or low-friction coatings,[76] for colloidal stabilization, as substrates for cell culture,[90] in biomaterials and for sensing, etc.[91] To generate such polymer films, individual polymer chains are attached to or grown from surfaces, in one or multiple steps to form a single or multiple layers. Attachment can occur either *via* multiple contact points along the polymer chain or *via* one of the chain ends. In the latter case, and if the chains are grafted at sufficiently high density, repulsion between chains induces the formation of a so-called polymer brush.[92, 93] In addition, the polymer chains may be interconnected by covalent or more transient non-covalent interactions, forming (hydro)gel films. The mechanical response of such polymer films is not only important for functional performance, but it can also provide valuable information about their internal organization, interactions and dynamics.

Colloidal probe atomic force microscopy is a popular and versatile technique for investigating the mechanical properties of thin films and macroscopic materials.[55, 56, 94] In force spectroscopy mode of operation, the cantilever attached probe is made to indent the material of interest. Forces are calculated from the deflection of the cantilever as a function of the relative position between probe and sample. In the following section we emphasize on the constraint of AFM in determining the absolute probe-substrate separation distance, in particular with soft hydrated surface confined films and describe how this limitation can be overcome by the combination of AFM with a microinterferometric technique. We develop a robust data analysis method for the combined setup.

To illustrate the use of the setup, we study the mechanical properties of films of end-grafted hyaluronan as a model of pericellular matrices. The resistance of HA films to compression forces under physiological ionic strength and pH is measured and the results analyzed in terms of simple polymer brush theory. The films Young modulus is also determined. This initial study on HA films is a prelude for the more systematic and detailed study presented in Chapter 4.

2.1.1 Limitation of AFM in probing absolute probe-sample separation distances

In the case of thin polymer films, it is often desirable to be able to relate the response to compression or shear forces to the film's thickness and to the precise location of the probe within the film. Ideally, one would want to measure the *absolute* distance between the probe and the solid substrate at the same time as the probe interacts with the film. A fundamental limitation of colloidal probe AFM is that the distance between the surfaces is not measured explicitly but inferred from the force measurement. For the characterization of polymer films, the consequence is that only *relative* changes in distance are accessible to experiment whereas the *absolute* probe-substrate distance remains unknown. In some cases, the probe-substrate distance can be inferred indirectly. For example, film thickness can be estimated by local removal (scratching) of the film with the aid of the AFM probe and subsequent analysis of the scratch depth.[95] This method though bears the risk of contaminating or even damaging the AFM probe. Patterned surfaces, in which the film and the bare surface are presented side by side,[33] provide useful means to perform reference measurements in the immediate vicinity of the film, from which the film thickness can then be deduced. This approach, however, requires surface functionalization methods that are not always easily applicable, e.g. for films that are built on supported lipid bilayers containing laterally mobile lipids.

2.1.2 RICM provides absolute distances and can be combined with AFM

Optical techniques such as reflection interference contrast microscopy (RICM) or total internal reflection microscopy present an interesting way to determine the distance between a colloidal probe and a planar substrate, because they can be used in a liquid environment and are compatible

with AFM.[96] RICM in particular can provide absolute distances with a resolution of a few nanometers and detect small-scale distance fluctuation with down to sub-Angstrom precision.[44, 64, 66, 67, 97] In this chapter, we present a novel method that combines AFM and RICM *in situ* to quantify the interaction forces between a colloidal probe and a (coated) planar substrate as a function of their absolute distance (Figure 2.1**A**). With the ability to measure forces and absolute distances simultaneously, the method resembles another well-known technique, the surface force apparatus (SFA, reviewed in ref. [98]). This method, although demanding and mastered by only a few research groups worldwide, has over the past three decades been very successfully used for the investigation of forces between surfaces and surface-confined polymer films.[62, 76, 99] With the commercial availability of combined atomic force and optical microscopy, AFM and RICM can now be quite easily combined into one instrument,[100-104] and the approach that we propose can hence in the future be readily adopted by many research groups.

2.2 Results

2.2.1 Combined colloidal probe AFM/RICM measurements

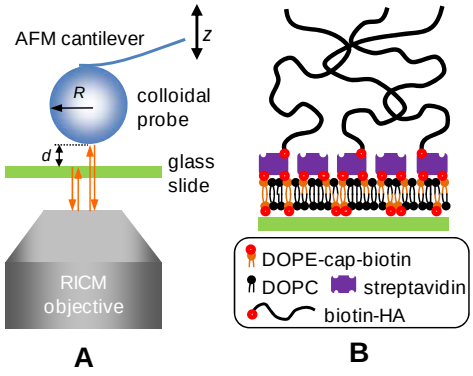

Figure 2.1 **(A)** Scheme of the combined colloidal probe AFM/RICM setup. **(B)** Scheme of the architecture of HA films. The size of streptavidin and the thickness of the supported lipid bilayer are drawn to scale; the mean anchor spacing and contour length of HA, and the thickness of the HA film are further reduced in size for illustrative purposes.

The combined AFM/RICM setup is schematically shown in Figure 2.1**A** (see Chapter 6.4.1 for a detailed description of the setup. The preparation and mounting of the liquid chamber is described in Chapter 6.4.2). The AFM was operated in conventional force mode: the cantilever was first approached towards and then retracted from the sample surface at a constant speed by the *z*-piezo, and the AFM's laser detection system recorded changes in the deflection of the cantilever. At the same time, a series of dual-wavelength RICM images (representative images are shown in Figure

2.2**A-B**) was taken. AFM force curves were acquired in closed-loop mode at an approach speed of v_{piezo} = 100 nm/s, and with a maximal load on the order of typically 10 nN.

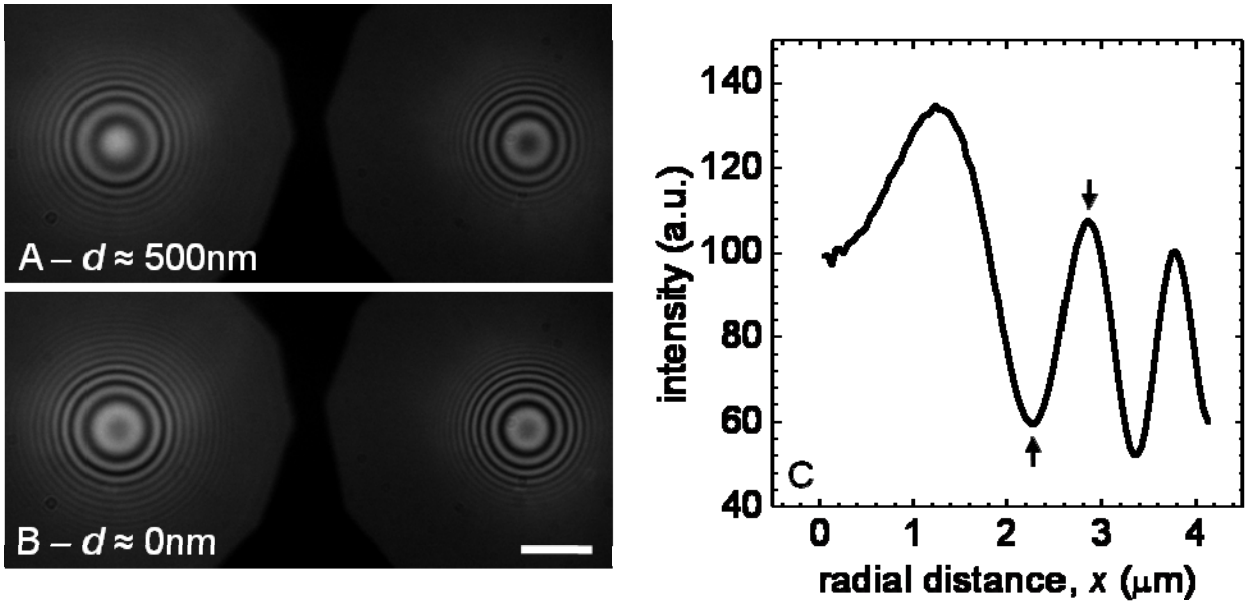

Figure 2.2 **RICM data. (A-B)** Dual wavelength interferographs at λ = 543 nm (*left*) and 438 nm (*right*) of a colloidal probe that was attached to an AFM cantilever and positioned at a distance of approximately 500 nm from a clean glass surface (**A**) and in close proximity to the surface (**B**). The characteristic set of concentric rings (Newtonian rings) is formed by the interference of light beams that are reflected at the glass/liquid and liquid/probe interfaces, respectively. A part of the edge of the field diaphragm that is used to focus the image is visible in the image centers. Scale bar: 5 μm. (**C**) Representative radially averaged intensity profile (λ = 543 nm) computed from the Newtonian rings in **B** (*left*). Two extrema that were used for the determination of the probe-surface distance *d* according to the *R*-adjustment method are marked (*arrow*s).

2.2.2 Analysis of RICM data

Different theoretical models have been reported in the past to extract the glass-probe distance *d* from RICM images.[64, 66, 97] For our purposes, we found the simplest model – the parallel plate approximation with incident light parallel to the surface normal[66] – most suitable. According to this model, *d* can be derived from the radial position of a selected extremum of the radially averaged intensity profile (a representative profile for λ = 543 nm is shown in (Figure 2.2**C**) of the Newtonian ring pattern (Figure 2.2**A-B**). In fact, multiple extrema provide multiple solutions, and detailed analysis reveals that the correlation of two carefully chosen solutions can be used (i) to reliably determine *d* without *a priori* knowledge of the exact probe radius and (ii) to correct for an imperfectly adjusted focus position. This method, which we call "*R*-adjustment", is described in detail below. Considering that colloidal probes typically exhibit a rather large variation in their diameter, and that the accurate determination of the bead radius by light microscopy is not trivial (in

particular for a probe attached to an AFM cantilever), the *R*-adjustment method simplifies data acquisition and evaluation, when compared to established methods.[64]

2.2.3 The "R-adjustment" method

We used a custom-developed algorithm, implemented in Matlab, to analyze RICM images. Each image was split into two halves, corresponding to interferographs at $\lambda = 438$ and 543 nm, respectively, and the two interferographs were analyzed independently. We use a set of interferographs at $\lambda = 543$ nm to demonstrate the analysis principle. First, the radially averaged intensity profiles of the Newtonian ring patterns were computed. A pattern for a selected interferograph is shown on the left side of Figure 2.2**B**, and the intensity profile in Figure 2.2**C**. The glass-probe distance, *d*, can be derived from the radial position, $x_{\mathrm{ext}}^{(i)}$, of a selected extremum, *i*, in the intensity profile:[66]

$$d_{\mathrm{min}}^{(l)} = \frac{\lambda l}{2n} - R + \sqrt{R^2 - {x_{\mathrm{ext}}^{(i)}}^2} \qquad \text{if the extremum } i \text{ is a minimum,} \qquad [2.1]$$

and

$$d_{\mathrm{max}}^{(l)} = \frac{\lambda(2l+1)}{4n} - R + \sqrt{R^2 - {x_{\mathrm{ext}}^{(i)}}^2} \qquad \text{if the extremum } i \text{ is a maximum.} \qquad [2.2]$$

Here, *R* is the probe radius, *n* is the refractive index of the aqueous medium between the probe and the glass surface ($n = 1.334$), and *l* is the fringe order (1, 2, …).

According to the simple model, and if *l* is selected properly, *d* should not depend on the choice of the extremum. Significant deviations are though expected to occur if the extremum is situated too far from the center, because corrections to the parallel plate approximation that arise from the finite curvature of the colloidal probe become important.[68] On the other hand, we observed that the accuracy in the determination of the extremum position decreased significantly for distances below 1.3 μm from the center, due to a limited number of pixels available for evaluation. For these reasons, we computed *d* only from the two extrema situated closest to but not closer than 1.3 μm from the center (arrows in Figure 2.2**C**). In the following, the radial positions of these extrema, and the resulting distances will be denoted as $x_{\mathrm{ext}}^{(\mathrm{I})}$ and $x_{\mathrm{ext}}^{(\mathrm{II})}$, and as $d^{(\mathrm{I})}$ and $d^{(\mathrm{II})}$, respectively.

Figure 2.3**A** shows the evolution of $d^{(\mathrm{I})}$ and $d^{(\mathrm{II})}$, calculated from $x_{\mathrm{ext}}^{(\mathrm{I})}$ and $x_{\mathrm{ext}}^{(\mathrm{II})}$ in a series of RICM images with a nominal $R = 12.5$ μm, during the acquisition of an AFM force curve on a clean glass surface in the presence of 10 mM NaCl. Approach and retraction rates of 100 nm/s and an exposure time of 100 ms imply that each interferograph, and the calculated distances, represent

averages over a probe travel of up to 10 nm. Initially, the distances decrease roughly linearly, as expected for approach at constant rate of the probe towards the surface. The plateau at intermediate times corresponds to 'hard-wall' contact between colloidal probe and glass surface, and the linearly increasing part to the retraction at constant rate. Overall, the curves for $d^{(I)}$ and $d^{(II)}$ are quite similar, as expected. A plot of the differences $\Delta d = d^{(I)}-d^{(II)}$ (Figure 2.3**B**) though revealed significant deviations. In the particular measurement in Figure 2.3**A-B**, Δd exhibited a mean value of 24 nm. Periodic variations in Δd with about 8 nm amplitude as a function of the probe-sample distance were also observed.

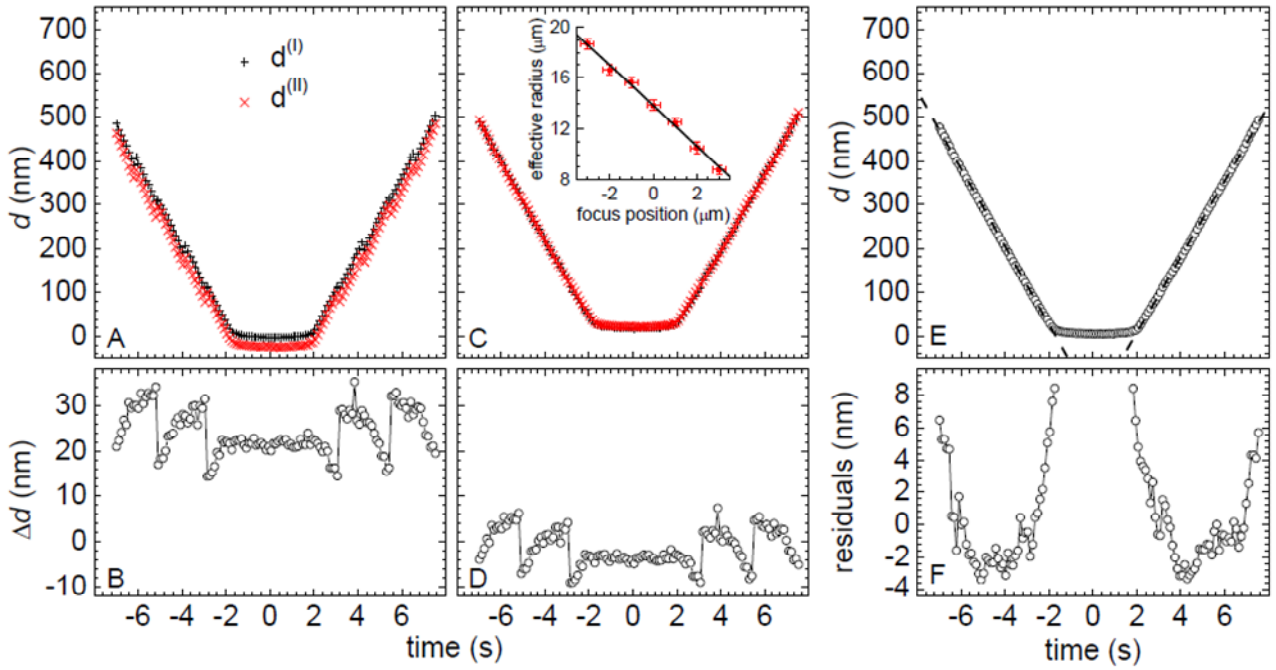

Figure 2.3 ***R*-adjustment method.** (**A**) Representative plot of the probe-surface distance *vs.* time, reconstructed from a series of interferographs ($\lambda = 543$ nm) that were taken while a colloidal probe cantilever approached (decrease in d), contacted (plateau) and retracted (increase in d) from a glass surface in a solution of 10 mM NaCl in ultrapure water. $d^{(I)}$ (×) and $d^{(II)}$ (+) correspond to the distances calculated from two extrema of radially averaged intensity profiles (see Figure 2.2**C**) and the nominal probe radius $R = 12.5$ µm. (**B**) Corresponding plot of $\Delta d = d^{(I)}-d^{(II)}$ *vs.* time. (**C** and **D**) The same data after minimization of $\chi^2 = \sum_t \Delta d(t)^2$ by adjustment of R (to 15.6 µm). (**E**) Plot of $d = [d^{(I)} + d^{(II)}]/2$ *vs.* time. The apparent distance at "hard wall" approach is not zero. A mean distance at "hard wall" approach of 15±5 nm was found for 5 different beads. Most likely, this systematic error is due to the simplified model and the surface roughness of the colloidal probe. To correct for the error, all data were offset by 15 nm. *Dashed lines* are linear fits to the approach and retract curves at distances >60 nm. (**F**) Residuals from the fits. The standard deviation is 3 nm.

One parameter that had a strong influence on the deviations was R. Adjustment of R such as to minimize $\chi^2 = \sum_t \Delta d(t)^2$ (Figure 2.3**C-D**) decreased the mean value to zero. It also decreased the amplitude of the periodic variations, albeit only weakly. The effective probe radius was found to be

15.6±0.2 μm, where the error in R corresponds to the range within which χ^2 increased by less than two-fold above its minimum.

Another parameter that we found to sensitively affect $d^{(I)}$, $d^{(II)}$ and Δd was the position of the focus of the microscope objective with respect to the sample. To quantify the impact of the focus position on our data, we acquired several series of RICM images while systematically varying the focus position within a range of ±3 μm around the optimal focus. Interestingly, the final values for $d^{(I)}$, $d^{(II)}$ and Δd for all image sets within the range of ±2 μm around the optimal focus agreed well, to within ±3 nm, after application of the above described R-adjustment method (data not shown). Furthermore, the effective probe radius depended linearly on the focus position (Figure 2.3**C** inset). These experimental results imply that variations in the focus position have the same effect as variations in the probe radius on the extrema positions in the radial intensity profiles of RICM images. We note in passing that the data for Figure 2.3**A-D** was intentionally acquired with too low a focus position, to better illustrate the method of R-adjustment. This explains why the effective probe radius is somewhat larger than the value specified by the manufacturer (25±3 μm). Effective probe radii measured at optimal focus position agreed to within 500 nm with values estimated from bright field microscopy images taken prior to attachment of the probes to the AFM cantilever.

The periodic variations in Δd could not be completely removed by the R-adjustment method (Figure 2.3**D**). Within the ranges of constant approach or retract rate, the length of the period was approximately 2 s, corresponding to 200 nm in distance. The latter value matches the period $\lambda/2n$ of the RICM response (which is 204 nm for $\lambda = 543$ nm). Close inspection of the data confirmed that the jumps in Δd at -5, -3, 3 and 5 s (Figure 2.3**D**) correlate with a transition to another fringe order. Apparently, these variations reflect limitations of the simple model. Fortunately, they largely disappear once $d^{(I)}$ and $d^{(II)}$ are averaged.

Figure 2.3**E** shows the distance d, obtained by averaging $d^{(I)}$ and $d^{(II)}$ after adjustment of R. It is notable that the apparent distance between the colloidal probe and the glass surface at hard-wall contact was significantly larger than zero. Additional measurements with a total of 5 different colloidal probes revealed a reproducible apparent distance of 15±5 nm, even though parallel AFM measurements clearly indicated hard-wall contact. We believe that the overestimation of the distance originates in part from the simplified assumptions that underlie Equation 2. Indeed Kühner and Sackmann[66] have previously found that a simple theory with similar assumptions overestimates the distances by 10 nm. The nm-scale roughness of the polystyrene beads is likely to be responsible for the remaining difference. To account for these systematic deviations, we have applied an offset of 15 nm to all distances determined by RICM. The R-adjusted data with 15 nm offset was then

further used to compute force-distance curves, or to extract the absolute distance at closest approach.

The RICM response is inherently periodic, and distances can therefore be determined without ambiguity only within a range of $\lambda/2n$, or 204 nm for $\lambda = 543$ nm in water, unless additional information is available. In the example in Figure 2.3, we had used the knowledge about the approximate approach speed, v_{piezo}, and the fact that the colloidal probe must touch the bare glass surface at closest approach, to unambiguously reconstruct the distances over a range of more than 500 nm. This method fails if an approximate knowledge about the probe-glass distance at closest approach is not available. This is the case, for example, if a rather thick film of *a priori* unknown thickness (e.g. an HA film) is to be investigated. For a given wavelength, several distance-time curves that are offset in d by integer multiples of $\lambda/2n$ would be consistent with the data. To remedy this shortcoming, RICM images were acquired at two wavelengths simultaneously. By correlating the data at 438 and 543 nm, most of the potential solutions can be discarded, and a unique solution remains within a range of approximately 1 μm, as previously described in the literature.[44, 64, 68]

At large enough distances from the surface, the evolution of the bead position should be dictated by the constant approach and retract speed of the AFM ($v_{piezo} = 100$ nm/s). Straight lines indeed fitted the data at distances larger than 60 nm well (Figure 2.3**E**). The residuals (Figure 2.3**F**) revealed minor systematic deviations, which are likely due to limitations of the simple model used to calculate the heights.[66] The standard deviation over a distance range of 500 nm was 3 nm. The accuracy of our method in measuring relative distances over a large distance range is comparable to values reported with other RICM-based methods.[64, 68] To obtain a measure of the resolving power of our setup, we performed sets of interferometric distance measurements with colloidal probes that were immobilized on a glass cover slip. The standard deviation for a given bead was typically smaller than 0.2 nm, again similar to what is commonly reported,[64, 66] although by an order of magnitude larger than in recent work by Heinrich et al.[97] The absolute slopes, v_{tot}, of such linear fits were similar to v_{piezo}, but not always identical. They scattered significantly between measurements, even for measurements that were performed with the same setup at different times. These observations imply that, in addition to the actuation of the probe by the z-piezo, drifts contribute to probe-substrate distance variations. Thermal drift in the deflection of the AFM cantilever is readily detected by the AFM, and typically accounted only for a part of the discrepancy. We conclude that drifts of the position of the glass slide (and/or other components in the setup) do also affect the probe-surface distance. Discrepancies were typically within a few percent for the open fluid cell, but occasionally reached remarkable 30% for the closed fluid cell setup. Apparently, during approach and retract cycles, the silicone rubber seal of the AFM liquid cell exerts enough pressure

to induce elastic deformation of the glass cover slip up to a few 100 nm. This type of drift cannot be detected by AFM alone, and would hence lead to erroneous force curves. It can, however, be readily detected and corrected by correlating AFM and RICM data, as we will outline in the following.

2.2.4 Determination of force vs. absolute distance curves from AFM and RICM data

It is worth noting that, in principle, force-distance curves can be extracted independently from RICM distance-time curves (Figure 2.3**E**) alone as well as from AFM deflection-displacement curves alone. In praxis, however, it proves useful to correlate both datasets, in order to be able to correct for drifts, to determine absolute distances and to maximize the resolution. Figure 2.4**A** and Table 2.1 define parameters that will be used in the description of the further data analysis process. Figure 2.4**B** displays a schematic force-distance curve that features three typical regimes of probe-sample interaction: a first regime in which the cantilever deflection is not affected by the sample (‘non-contact`), a second regime in which probe-sample interactions result in cantilever deflection (‘contact’), and a third regime in which the probe senses the rigid sample support (‘hard-wall contact’). In practically relevant cases, the AFM data covers the non-contact and contact regimes, and optionally the hard-wall contact regime. The RICM data covers the repulsive regime, and optionally the non-contact and hard-wall contact regimes. Depending on whether or not the RICM data covers a sufficiently large part (i.e. spanning a range of several 100 nm in d) of the non-contact regime, different analysis strategies can be used to compute deflection *vs.* distance curves. These are schematically outlined in Figure 2.4**C**-**D** and described in the following.

Case 1 – RICM data in the non-contact regime is available (Figure 2.4C). In the non-contact regime, the cantilever deflection δ is zero and the changes in displacement z and probe-substrate distance d are hence identical ($\Delta z = \Delta d$). The displacement rate v_{tot} can therefore be readily determined from the slope of a linear fit to the RICM distance-time data in this regime. RICM data are then easily converted into force-distance curves by a set of simple transformations (steps 1-3 in Figure 2.4**C**; in step 2, δ is offset to zero in the non-contact regime). Analysis of the AFM data is slightly more involved. First, the readout of the 4-quadrant photodetector voltage U_{PD} needs to be corrected for thermal drift in the cantilever deflection δ_{drift} (step 4). This is done by subtracting the slope in the non-contact regime from U_{PD}, followed by offsetting U_{PD} in the non-contact regime to zero. Second, the z-displacement is corrected for drifts in the cantilever deflection, δ_{drift}, and for drifts in the positioning of the glass slide relative to the probe, z_{drift}, according to $\Delta z = z_{\mathrm{piezo}} + z_{\mathrm{drift}} - \delta_{\mathrm{drift}} = \left(v_{\mathrm{piezo}} + v_{\mathrm{z\text{-}drift}} - v_{\mathrm{c\text{-}drift}}\right)\Delta t = v_{\mathrm{tot}}\Delta t$ (step 5), where v_{tot} is taken from the RICM data. Third, the drift-corrected deflection voltage U is converted into cantilever deflection through $\delta = US$ (step 8). In conventional AFM measurements, determination of the sensitivity S requires a

separate reference measurement on a rigid substrate. If RICM data from the non-contact region is available, such a reference measurement is dispensable, because the RICM-derived force-distance curve can be used as an internal reference to determine sensitivity. To this end, AFM and RICM data are compared after simple transformations (steps 6-7). From δ (RICM data) and U (AFM data) at time t_1 (selected from data in the contact or hard-wall contact regimes) the sensitivity is given by $S = \delta(t_1)/U(t_1)$. Fourth, a simple transformation, based on $z = d - \delta$ and an appropriate offset in d provide deflection as a function of absolute distance (step 9). Here, the distance at closest approach, as determined by RICM, is used to offset d if data from the hard-wall contact regime is not available. Otherwise, the distance at closest approach is simply set to zero. Eventually, force *vs.* absolute distance curves are obtained through $F(d) = k\delta(d)$ (step 10).

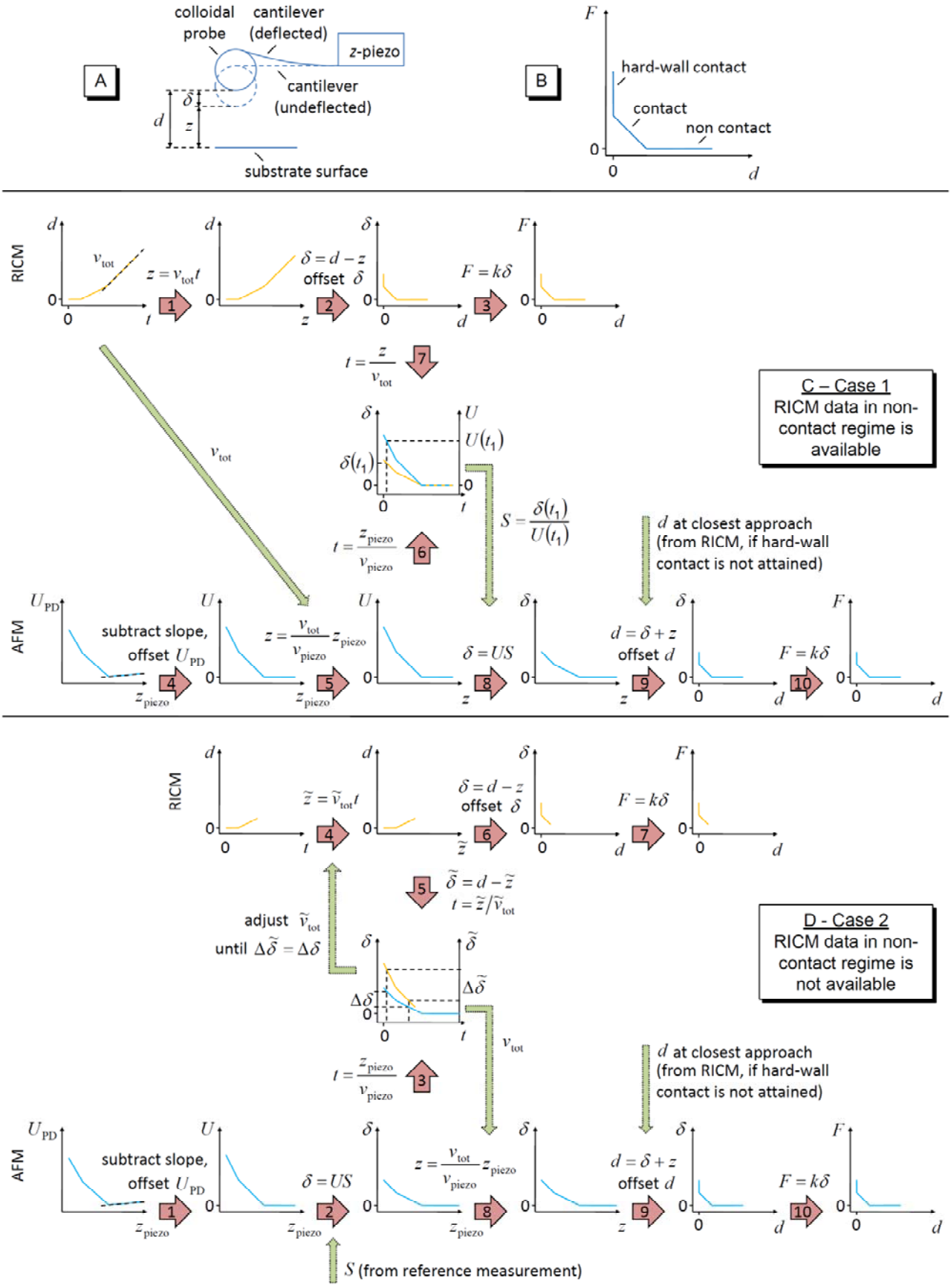

Figure 2.4 Process of determination of deflection-distance curves from RICM and AFM data. (**A**) Scheme of the setup with definition of parameters z, d and δ. (**B**) Scheme of an idealized force−distance curve with distinct noncontact, contact and hard-wall contact

regimes. Each regime is represented by a straight line. (C and D) Idealized curves (RICM, orange lines AFM, blue lines) are used to illustrate th data analysis process. (**C**) Case 1: If sufficient RICM data from the noncontact regime is available, then the accurate displacement rate vtot can be determined from the slope of a linear fit to the data in this regime. The RICM data can then also be used as an internal reference to calibrate the sensitivity S. (**D**) Case 2: If sufficient RICM data from the noncontact regime is not available, then vtot can be determined iteratively by correlating RICM and AFM deflection data. The sequence of data transformation steps is indicated by numbers inside the pink arrows. See Table 2.1 for the definition of additional parameters, and the main text for a detailed description of the analysis schemes.

Table 2.1 Overview of parameters employed in Figure 2.4

Distance parameters (in nm)	
probe-substrate distance	d
Deflection	δ
(total) displacement	$z = d - \delta$
piezo-displacement	z_{piezo}
z-displacement drift	z_{drift}
cantilever deflection drift	δ_{drift}
Rate parameters (in nm/s)	
total displacement rate	v_{tot}
z-piezo displacement rate	v_{piezo}
z-displacement drift rate	$v_{\text{z-drift}}$
cantilever deflection drift rate	$v_{\text{c-drift}}$
AFM laser detection parameters	
sensitivity (in nm/V)	S
photodetector voltage (in V)	$U_{\text{PD}} = (\delta + \delta_{\text{drift}})/S$
deflection voltage (in V)	$U = \delta/S$
cantilever spring constant (in N/m)	k
force (in nN)	$F = k\delta$

Case 2 – RICM data in the non-contact regime is not available (Figure 2.4D). The data analysis is similar to Case 1, but the analysis steps proceed in a different order (as indicated), and S and v_{tot} are determined in a different manner. S now needs to be provided *via* a separate reference measurement on a rigid substrate. v_{tot} is determined through an iterative procedure: starting with the estimate $\tilde{v}_{\mathrm{tot}} = v_{\mathrm{piezo}}$, $\tilde{v}_{\mathrm{tot}}$ is adjusted through steps 4 and 5 until the deflections δ (from AFM data) and $\tilde{\delta}$ (from RICM data) coincide.

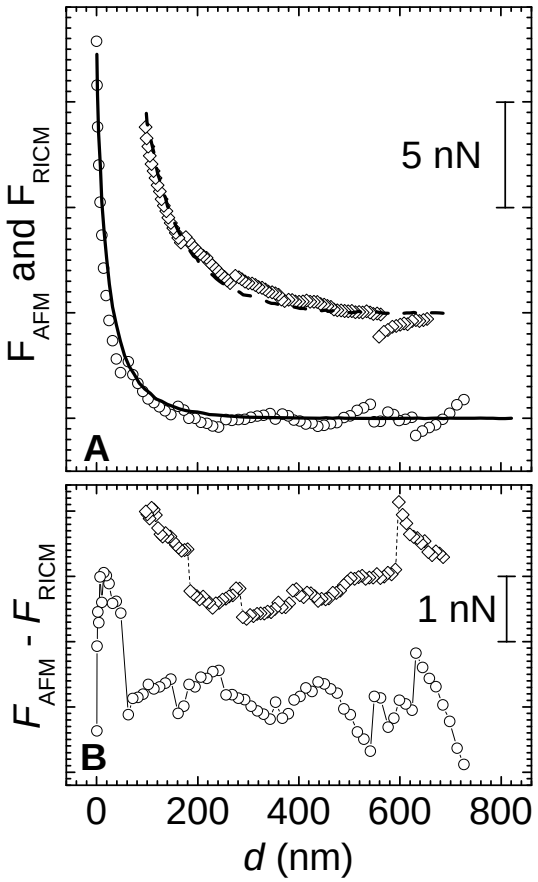

Figure 2.5 Comparison of force−distance curves by colloidal probe AFM and RICM. (**A**) Force−distance curves derived from AFM (lines) and RICM (symbols) data, respectively, acquired simultaneously during the approach of a colloidal probe to a bare glass surface in 10 μM NaCl (solid line, circles) and to an HA film (dashed line, lozenges, offset by 5 nN). RICM data were used to adjust the AFM data for linear drifts in probe-sample separation, to determine the AFM cantilever sensitivity (on bare glass) or the distance at closest approach (on the HA film). (**B**) Difference plots of the two sets of curves in panel A.

Two sets of representative AFM and RICM-derived force-distance curves, one with and another without hard-wall contact, are shown in Figure 2.5**A**. Overall, the AFM and RICM curves agree well. Most of the residual differences (Figure 2.5**B**) fall within a range of ±0.4 nN in F, or 4 nm in δ. This is close to the experimental error that we had established for the RICM data. Mildly

increased residuals (up to 2 nN) were sometimes found at very small distances, the origin of which remains obscure. Increased data scatter, with a magnitude of 1 nN, can also be observed at distances above 500 nm in the RICM data. We suspect that this originates from the limited coherence of the employed light which makes the contrast of the interferographs decrease with increasing distance. We note that the resolution of the AFM in terms of relative distances and forces, as well as the distance range accessible to AFM, are superior to RICM. In praxis, it is hence preferable to make use of the AFM data, combined with a quantification of the distance at closest approach by RICM, to compute forces as a function of absolute distance.

2.2.5 Compression of HA films

HA films were built on a streptavidin-coated supported lipid bilayer, *via* a biotin anchor at one of the ends of the HA molecules (Figure 2.1**B**). Details of the formation of HA films on glass slide, are given in Chapter 6.4.3. Figure 2.6**A** shows a representative force-distance curve on such a grafted HA film. The interaction was purely repulsive. Both HA and polystyrene are negatively charged, and the absence of adhesion is hence not unexpected. In addition, the approach and retract curves superposed very well, indicating that the compression was purely elastic. The elastic response indicates (i) that the chains can rearrange rapidly, within seconds, without significant dissipative losses and regain their original conformation if external stress is released, and (ii) that concomitant liquid flow in and out of the compressed area occurs with relative ease, without significant energy dissipation. The force curves upon repeated compression of the same spot, and upon compression of different spots on the same sample, were highly reproducible (typically to within the line thickness in Figure 2.6). Independent measurements with different samples or probes also generated very similar curves, although with slightly larger deviations, which we attribute to minor variations in sample preparation.

Defining $F_{th} = 50$ pN, which is just above the noise level, as a threshold force, we estimated a film thickness of about 518±30 nm from Figure 2.6**A**. This is about 6-fold more than the radius of gyration ($R_g = 88$ nm) and 6-fold less than the contour length ($l_c = 2.86$ μm) of 1.08 MDa HA.[44, 105] The appreciable stretching of the grafted chains is a first indicator for the presence of a polymer brush. To test how well our film conforms to brush behavior, we compared the data with a simple model of neutral polymer brushes. For a single brush of equilibrium thickness L that is compressed between a planar and a spherical surface of radius $R \gg L$, scaling theory by Alexander and de Gennes[79] (AdG) predicts:[62]

$$\frac{F}{R} \cong \frac{8\pi}{35} kT \frac{L}{s^3} \left[7(L/d)^{5/4} + 5(d/L)^{7/4} - 12 \right] \quad \text{for } d/L < 1. \qquad [2.3]$$

Here, $kT = 4.1\times10^{-21}$ J (at 25°C) is the thermal energy and s the characteristic spacing between grafting points (i.e. s^2 is the surface area per chain). According to the Derjaguin approximation, F/R is proportional to the compression energy ($W = F/(2\pi R)$ between two planar surfaces, i.e. independent of the probe radius.[62] Within a rather large distance range, this equation can be approximated by an exponential:[62]

$$\frac{F}{R} \cong 100 kT \frac{L}{s^3} e^{-2\pi d/L} \qquad \text{for } 0.2 < d/L < 0.9. \qquad [2.4]$$

The right-hand side of both equations is accurate to within an unknown numerical prefactor of order unity.

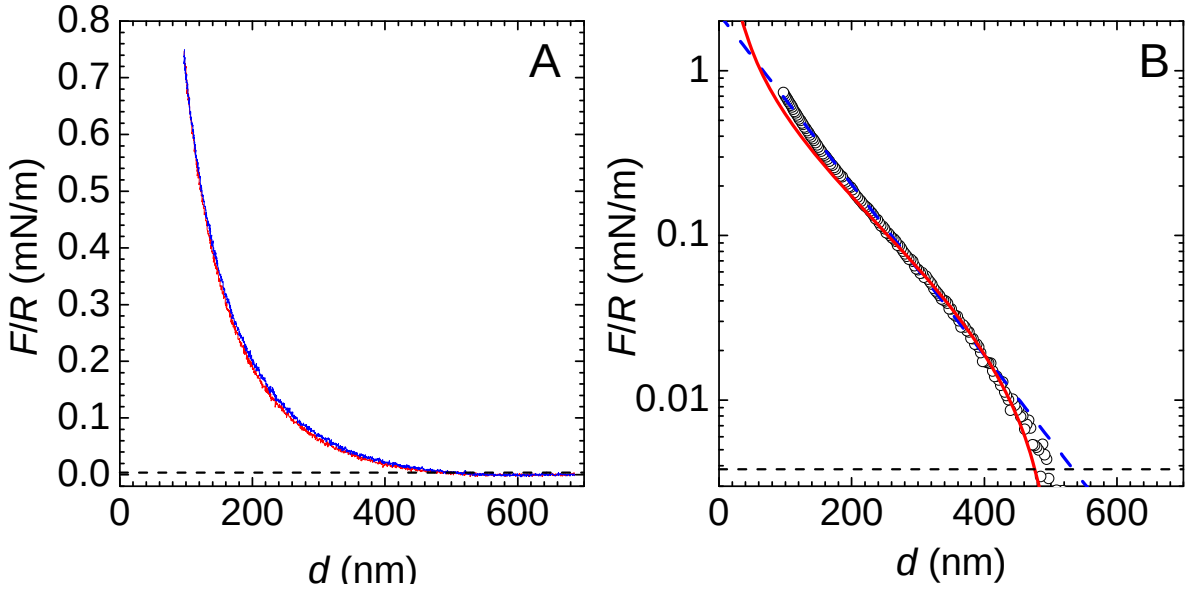

Figure 2.6 Compressive response of HA films. (**A**) Force *vs*. distance curves (approach, red line; retract, blue line) for the compression of a film of end-grafted HA in the presence of 150 mM NaCl (Debye length 0.8 nm) at pH 7.4. Forces were normalized by the probe radius of 13.0 µm, obtained through the R-adjustment method at optimal focus position. (**B**) Approach data from **A** in a log−linear presentation (black circles) with fits from polymer brush models (Equation 2.3 with L = 511 nm and s = 46 nm, red solid line; eq 2.4 with L = 501 nm and s = 50 nm, blue dashed line). Dashed horizontal lines indicate the threshold force F_{th}.

Both equations fitted the experimental data well (Figure 2.6**B**). A fit with Equation 2.3 over the range $0.5L \leq d \leq L$ resulted in L =511 nm and s =46 nm (Figure 2.6**B**). The thickness agrees well with the value that was directly extracted *via* F_{th} = 50 pN, and with a previously reported value of 530 ± 20 nm for a similarly prepared HA film.[44] In that study, we had also determined a mean anchor spacing of 60 nm on a hexagonal lattice, which corresponds to a characteristic spacing of

$s = 3^{1/4}/2^{1/2} \times 60\text{nm} = 56\text{nm}$, by reflectometry. Here, the quantitative agreement is also reasonable, if one considers the uncertainty due to the unknown prefactor of order unity in Equation 2.3. A fit with Equation 2.4 gave L = 501 nm and s = 50 nm (Figure 2.6**B**), which is also in agreement with the above-mentioned values. The quality and the results of the fits provide further evidence that HA films behave as polymer brushes at physiological ionic strength.

Minor yet significant deviations were though noticeable at weak ($d > 0.9L$) and strong ($d < 0.5L$) compression. We suggest that these deviations come about because the Alexander-de Gennes model is a simplified representation of reality. For example, it neglects higher-order (e.g. ternary) interactions between chains, which may become important at high compression. It also assumes a constant density profile, rather than a more realistic gradually decaying density profile,[80, 106, 107] which is likely to affect the regime of weak compression. We noticed that L and s exhibited some sensitivity to the choice of the compression range: when the data at $d < 0.5L$ was included in the fit with Equation 2.3, L and s were about 13% smaller. The deviations at weak compression, on the other hand, had no appreciable effect on the fitting results. We remind also that HA is a charged polymer. A rigorous investigation of the impact of charge and density profile on HA brush behavior is presented in Chapter 4. Here we confine us to note that at physiological ionic strength, the Debye length (0.8 nm) is much smaller than s, i.e. electrostatic interactions are short-ranged, and can be treated to good approximation as effective excluded volume interactions within the framework of polymer brush models.[84]

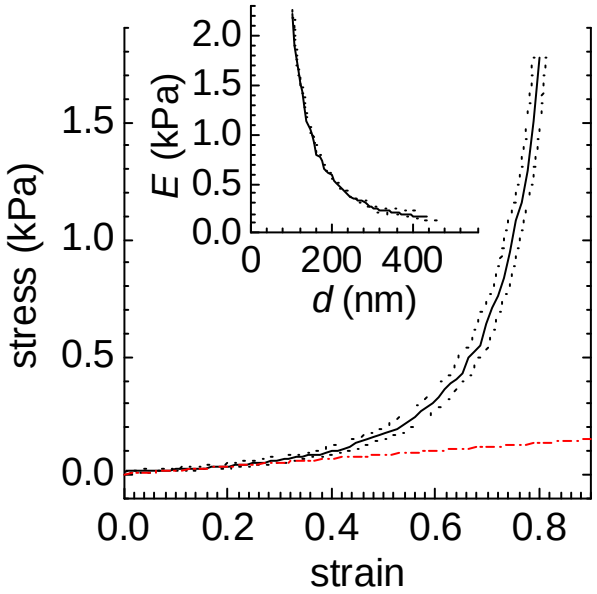

Figure 2.7 Stress *vs.* strain curve for the approach data from Figure 2.6**A**, assuming L = 518 ± 30 nm. Dotted curves represent the error due to the uncertainty in L. The slope of the red dash-dotted line (0.17 kPa) indicates the Young modulus, E = stress/strain, at low strain. The inset shows the evolution of E as a function of distance for strains above 0.15.

A material parameter of common interest, the Young modulus E, can be determined from the force *vs.* distance curve in the following way. The pressure or stress acting on an HA film between two co-planar surfaces of distance d is given through Derjaguin's approximation as $P = \mathrm{d}W/\mathrm{d}d = (2\pi)^{-1}\mathrm{d}(F/R)/\mathrm{d}d$.[62] Stress as a function of strain, $1-d/L$, is displayed in Figure 2.7. To obtain meaningful derivatives of the force *vs.* distance data, the curve was first smoothened by interpolation with a cubic B-spline algorithm. The Young modulus is given as the ratio of stress and strain, i.e. $E = P/(1-d/L)$. It is approximately constant up to a compression of 25%, with a value of 0.17 kPa (Figure 2.7, red dash-dotted line). For higher strains, E increases progressively, and reaches 2 kPa at 80% (Figure 2.7, inset).

2.3 Discussion

We have developed a novel method to determine forces between a colloidal probe and a planar surface as a function of their absolute distance. With this method we could quantify the compressive response of HA brushes under physiological ionic strength and pH conditions.

2.3.1 Instrumental development

Our technical approach is based on the *in situ* combination of colloidal probe AFM and RICM. A purpose-designed algorithm for the analysis of RICM images provides absolute distances with an accuracy of a few nanometers. The technique is robust in several regards. First, and in contrast to methods described earlier,[64, 103] the RICM image analysis method can correct for inaccuracies in probe radius and/or focus position. Second, linear drifts in the probe-sample distance can be detected and corrected for. Third, the sensitivity of the AFM deflection detection can in some cases (i.e. when RICM data for the non-contact regime is available) be calibrated without a separate reference measurement on a bare surface.

In the past, the surface force apparatus (SFA),[98, 108, 109] has been very successful for the investigation of forces between surfaces. A comparison with our setup is worthwhile. With a force resolution of the AFM of about 10 pN and typical bead radii above 10 μm, the resolution of our setup in terms of normalized normal force is $F/R \approx 1$ μN/m. This value is comparable to the best force resolution that can be obtained by SFA.[98, 110] The current resolution in d remains by one to two orders of magnitude below that of the SFA.[98] Further refinements in the data analysis[64, 66, 97] might improve this value somewhat, but ultimately the nm-scale roughness of the colloidal bead and the surface will present limitations that currently remain hard to overcome. On the other hand, the combined AFM/RICM setup has practical advantages: the setup can be readily implemented on

commercially available combinations of AFM and optical microscopy; and the chamber volume is approximately 200 µl, or about 2 orders of magnitude less than the SFA, which is desirable if the amount of available sample is limited.

The combined AFM/RICM setup should in the future prove useful to investigate soft and solvated transparent films of thicknesses between a few 10 nm and a few micrometers. The method is versatile. The planar surface and the colloidal probe can be functionalized independently, and the interaction between two surfaces with different adlayers can readily be probed. The approach rates accessible by AFM are typically faster than those of the SFA, and our setup should hence be particularly useful to investigate compression dynamics out of equilibrium. With the sensitivity of AFM to cantilever torque, the AFM/RICM combination can also be used to study the friction between polymer films as a function of normal load.

2.3.2 Mechanical properties of hyaluronan films - biological implications

Hyaluronan is produced and extruded into the extracellular space by hyaluronan synthases, and it is known that the glycosaminoglycan can stay attached with one of its ends to these cell surface membrane proteins. Our model films recapitulate this mode of attachment. From $L = 518$ nm and $s = 56$ nm, we find that the film has a remarkable hydration of ~99.9% and a mean HA concentration of 1.1 mg/mL.[44] Similar concentrations have been found *in vivo*, e.g. in synovial fluid.[111] Indeed, HA has been proposed to adopt a brush-like conformation around cells, in different topologies.[2, 112-114] Our results may hence have direct relevance for the mechanical properties of the cellular environment of, e.g., chondrocytes in cartilage[112] or of the endothelial cell surface.[115-117] They should present an interesting reference for future mechanical studies on real cellular coats, which are likely to be more complex.[114, 118]

To our knowledge, this is the first study on the mechanical properties of films of (end-)grafted HA chains. The Young moduli of our HA brushes, 0.2 to 2 kPa, are representative for very soft gels. A 0.4% agarose gel, for example, has a Young modulus of approximately 1 to 2 kPa.[119] From a polymer physics point of view,[79, 92, 93, 120] the behavior of HA brushes is expected to be drastically different from HA chains that are physisorbed, specifically bound or covalently attached *via* several points along the chain, as investigated in earlier studies.[99, 121-124] More specifically, the latter are expected to exhibit a thickness comparable to the radius of gyration whereas brushes can become much thicker. Indeed, the thickness of our HA brushes is 5 to 10-fold larger than what has been reported previously for side-attached HA-films of similar molecular weight under near-physiological ionic strength.[121, 123, 124]

The colloidal probes that we have used in this study are large enough to interact with many chains simultaneously. For example, if the film is compressed to a strain of 0.8, the contact area would cover about 10000 HA chains, as can be easily estimated from *s* and *R*. With HA-rich pericellular coats being present around a large number of cell types, one might expect that such coats perturb the imaging of the cell surface by mechanical techniques such as AFM.[125] The size of the probes that are typically used for imaging, however, is much smaller than what we have used here. Rescaling our results (Figure 2.6) to a probe radius of 25 nm, we can estimate that a force of 50 pN, comparable to the forces that are typically used for AFM imaging, would suffice to achieve 90% compression. In fact, it is likely that the compression forces are even smaller, because the sharp imaging probes interact with a rather small number of chains (e.g., a few 100 for a cone-shaped tip with 70° opening angle) and these can evade compression by bending to the side.[126] This rationalizes why imaging of cell surfaces can be possible despite the presence of a thick pericellular coat.

We remind that our HA brushes were formed on fluid supported lipid bilayers, and one might argue that the compression should result in the lateral displacement of HA out of the compression zone. This has indeed been reported for films of HA molecules that were either physisorbed to surfaces[122] or covalently bound to SLBs *via* multiple attachment points along the chain.[121] The good agreement of our data with polymer brush models suggests that lateral displacement is negligible in our case. The reason is likely to lie in the details of our experimental approach. First, we used streptavidin to graft HA to the SLB. This protein is known to form two-dimensional crystalline domains on glass-SLBs.[127] Some, if not all, of the HA anchor points are hence likely to be immobile. Second, the approach speed in our study was rather high, compared to previous SFA studies.[121, 122] The lateral disentanglement of HA chains in the brush might be significantly slower than the compression in our case.

Future studies that systematically vary the grafting density, molecular weight and lateral mobility of HA, external conditions such as divalent ions or pH, and the compression rate should allow to further refine our understanding of the behavior of HA assemblies in and out of equilibrium. Our study illustrates that the experimental data for such a system can be quantitatively compared with predictions from polymer theory. The complexity of the studied system can now be systematically increased by including other macromolecules of interest, such as hyaladherins.[45]

2.4 Conclusions

We have developed a novel method, based on the *in situ* combination of colloidal probe AFM and RICM that enables to probe the compression forces, and potentially even friction forces, of surface-confined polymer films with tight control on the distance between the two surfaces. The two techniques are highly complementary: AFM provides forces as a function of relative distance with high resolution; RICM supplies absolute distances, enables the correction of AFM data for linear instrumental drifts, and can even give cantilever sensitivity without an extra reference measurement. The method was used to investigate the compressive response of films of end-grafted HA. The films showed a compressive response in good quantitative agreement with a simple theoretical model of polymer brushes. The method represents a novel tool for the quantitative correlation between the supramolecular organization and the mechanical properties of surface-confined HA assemblies, and highly solvated polymer films such as polymer brushes in general.

3. Hyaluronan-aggrecan brush mechanics

Strongly hydrated assemblies made of the proteoglycan aggrecan and the polysaccharide hyaluronan are essential for the mechanical performance of cartilage, and their modification is suspected to be at the origin of related pathologies such as osteoarthritis. To better understand, how mechanical properties arise from the supramolecular structure and dynamics of such assemblies, we have studied the effect of aggrecan on the physico-chemical properties of a well-defined, reconstituted model system: films of surface-grafted HA chains. From interaction studies by QCM-D and spectroscopic ellipsometry, and mechanical studies by a combined colloidal probe AFM/RICM setup, we find that aggrecan readily intercalates into HA brushes in a reversible manner. Aggrecan induces a drastic swelling of HA brushes, generating self-assembled films of several micrometers in thickness that are highly hydrated and very soft. The Young modulus in the linear compression regime is below 100 Pa, and reaches several kPa at strong compression. The implications of these findings for biological function are discussed. The insights should also be of interest to other types of proteoglycan-HA complexes.

3.1 Introduction

Pericellular coats (PCCs) do also contain proteins that bind specifically to HA, called hyaladherins. Depending on their nature and abundance, they may crosslink, collapse, stiffen or swell individual HA chains, and thereby modify the morphology and physico-chemical properties of HA assemblies.[2, 21, 24, 25, 28, 29, 45, 128] Perhaps the most remarkable hyaladherin in terms of its molecular design is aggrecan. Aggrecan is a large bottle-brush shaped proteoglycan.[30, 35, 36] The contour length of the core protein is typically 350 nm and the multiple glycosaminoglycan side chains extend about 30 nm from the core protein.[35] Aggrecan and HA can assemble into large multimolecular complexes, which are an essential component of cartilage, and the pericellular space around chondrocytes.

Numerous biological functions of PCCs have been related to their mechanical properties.[25, 112, 117] Over recent years, methods have been emerging to assess the mechanics of native PCCs, e.g. for cells in culture[114, 118, 129, 130] or for the endothelial cell surface in blood capillaries.[117] Such studies provide meaningful information about variations in PCC properties between cell types (e.g. in disease) or as a function of cell or environmental stimuli. It remains challenging, however, to

understand how the mechanical properties of the PCCs are connected to its supramolecular structure and dynamics. This is so because the composition of the PCC around living cells is difficult to quantify and the supramolecular organization of PCCs is difficult to image at high resolution – due to the strong hydration, imaging contrast is very low and the assemblies are destroyed upon drying.

Tailor-made model systems that contain a selected subset of the PCC's components and that recapitulate the two-dimensional confinement and the self-assembly properties of the PCC can be used to address this challenge.[44] Here, we make use of the HA brushes characterized in Chapter 3 to study the effect of aggrecan on the morphology and mechanical properties of HA assemblies. Due to the confinement of the HA assembly to a solid support, the physico-chemical properties of the HA films as a function of external cues become accessible to investigation by surface-sensitive biophysical techniques.[44, 45] We employ quartz crystal microbalance with dissipation monitoring (QCM-D) and spectroscopic ellipsometry to monitor film formation and to quantify the binding kinetics of aggrecan. Because the HA and composite HA-aggrean films are optically thick, ellipsometry becomes sensitive to the density profile of such films, and we therefore consider a parabolic density profile when extracting film thickness and optical properties from the ellipsometric data. Furthermore, the compression forces and mechanical properties of HA brushes in the presence of aggrecan were measured by the combined colloidal-probe AFM/RICM technique and compared with HA brushes alone.

3.2 Results

3.2.1 Binding of aggrecan to hyaluronan brushes monitored by QCM-D

QCM-D was used to monitor the formation of the HA film and the binding of aggrecan to HA-brushes. The experimental setup and its operation are described in Chapter 6.5. A mass uptake by the sensor surface causes a decrease in the resonance frequency of the oscillating sensor crystal, whereas the dissipation shift provides information about the viscoelastic properties (i.e. rigidity or softness) of the adsorbed layer. Figure 3.1 shows QCM-D data at selected overtones (n = 5, 9, 13, corresponding to resonance frequencies of ~25, 45, 65 MHz) during the assembly of an HA film with aggrecan.

The first assembly step, i.e. the formation of a supported lipid bilayer (SLB) upon exposure of biotinylated small unilamellar vesicles (b-SUVs) at 50 μg/mL final concentration to a silica-coated sensor is shown in Figure 3.1**A** and **C.** The two-phase QCM-D response is characteristic for SLB formation, and has been analyzed in detail by others.[42, 71] A decrease in frequency and an increase in

dissipation is observed, when b-SUVs first adsorb to the surface. As coverage increases, vesicles start to rupture and transform into bilayer patches. The main reason for the increase in the frequency in the second phase is the loss of solvent mass in the lipid film: as surface-bound vesicles rupture and spread, water trapped inside or hydrodynamically coupled to the vesicles is released. At the same time, a planar bilayer appears more rigid than a vesicular layer and hence dissipation goes down. Ultimately, frequency and dissipation equilibrate, indicating that the SLB formation process is complete. The observed final frequency and dissipation shifts were within the limits of $\Delta f = -25 \pm 1$ Hz and $\Delta D < 0.3 \times 10^{-6}$, respectively, consistent with the formation of an SLB of good quality.[131]

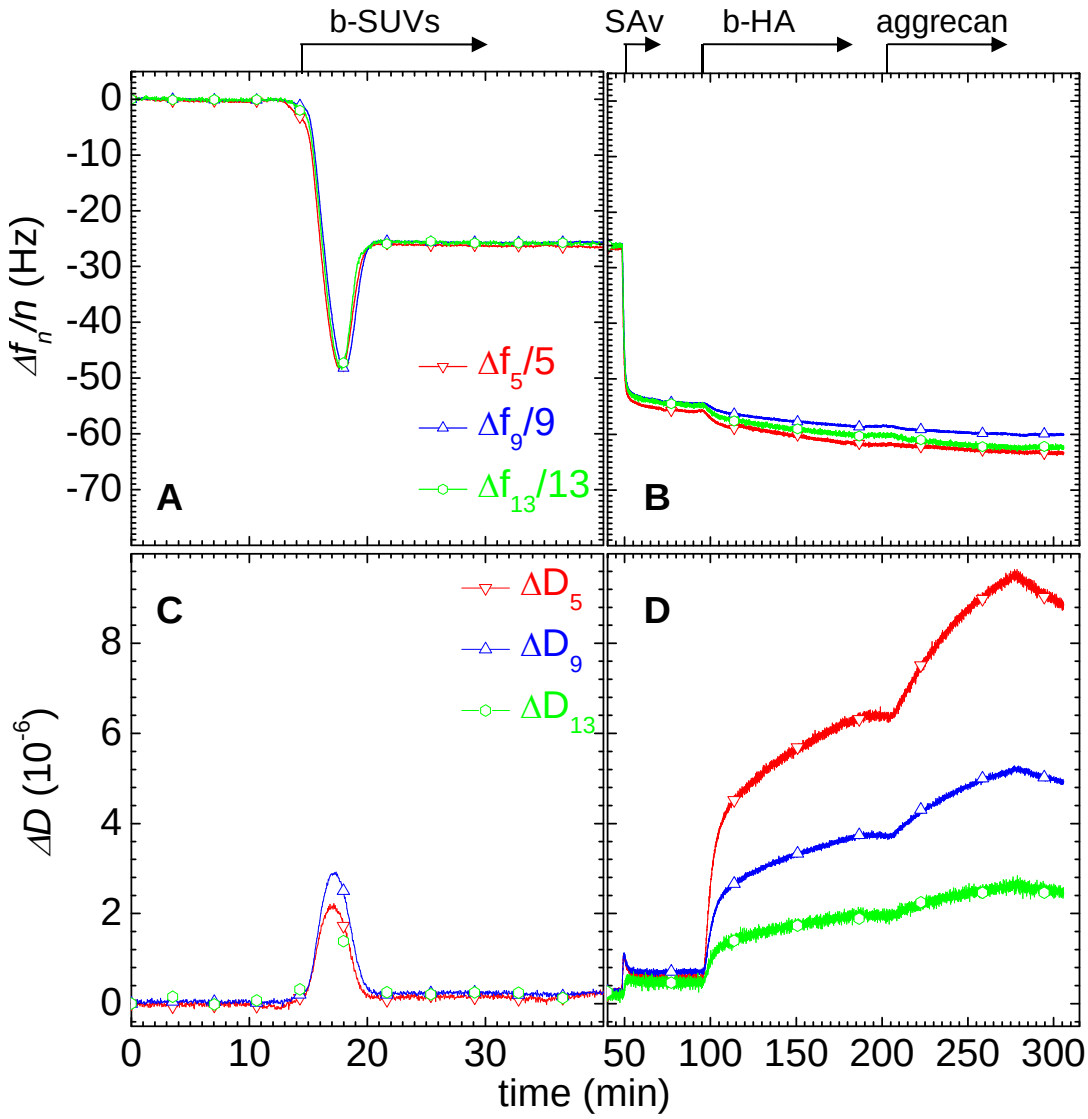

Figure 3.1 **Formation of an aggrecan-containing HA film monitored by QCM-D.** F*requency* (*Δf*) and *dissipation* (*ΔD*) shifts at different overtones (as indicated) during film assembly. The start and duration of incubation steps with sample solutions is indicated by the arrows on top of the panels. During remaining times, the sensor surface was rinsed with pure buffer solution.

A further decrease in the frequency (Figure 3.1**B** and **D**), with a measurable increase in the dissipation (about 0.3×10^{-6} at 80 min), was noticed upon addition of streptavidin (SAv) at a final concentration of 20 μg/mL to the biotinylated SLB. After 15 min, a plateau was reached. The frequency shift of -28 Hz upon exposure to SAv is consistent with the formation of dense monolayer of proteins. The binding of SAv was irreversible, as would be expected from specific immobilization through strong biotin-SAv bonds. Overall, the pattern of frequency and dissipation shifts agrees very well with earlier reports for the formation of a SAv monolayer on a solid-supported lipid bilayer.[44, 132]

Subsequent grafting of biotinylated HA (b-HA) to the SAv layer occurred by incubating a 20 μg/mL b-HA (molecular mass of 837 ± 42 kDa) solution for 90 min. This incubation step resulted in detectable but small changes in the frequency and large shifts in dissipation. The pronounced spreading of the dissipation responses as a function of overtone, the elevated changes in the dissipation shifts and the small changes in frequency indicate the formation of a very soft and hydrated film, as expected for an HA brush and reported earlier.[44] No further changes were observed after rinsing, indicating that HA was stably grafted to the surface.

When aggrecan was added to the HA film at a final concentration of 400 μg/mL, no major changes in frequency but a large increase in dissipation occurred, indicating interaction. The clear similarity in response compared with the HA film formation provides evidence that the HA remains very soft and hydrated even after incorporation of aggrecan. Rinsing with buffer did not result in measurable changes in the frequency response, but the dissipation decreased. This indicates that binding of aggrecan to the HA film is reversible.

3.2.2 Quantification of adsorbed amounts by spectroscopic ellipsometry

In situ spectroscopic ellipsometry was employed to quantify the areal mass density of lipids, streptavidin, HA and aggrecan throughout the film formation process. A silica wafer was used as support in ellipsometry experiments. As the QCM-D sensor, the wafer exposes silicon oxide on its surface. The experimental setup and sample preparation are described in detail in Chapter 6.6. To extract the film properties from the measured ellipsometric parameters, data were fitted with a model of multiple laterally homogenous layers (see Chapter 6.6.2). Briefly, the supported lipid bilayer and streptavidin monolayer were treated as a single biomolecular layer (index SLB/SAv), and treated as a homogeneous and transparent Cauchy medium with the first Cauchy parameter $A_{SLB/SAv}$ (A is a measure for the refractive index). The HA film with or without aggrecan was treated as a separate second biomolecular layer (index HA), and treated as a transparent Cauchy medium with a parabolic refractive index profile (here, the first Cauchy parameter $A_{HA,0}$ refers to the optical

properties at the base of the layer). The film thickness L and the optical properties of these biomolecular layers were determined as a function of incubation time (Table 3.1).

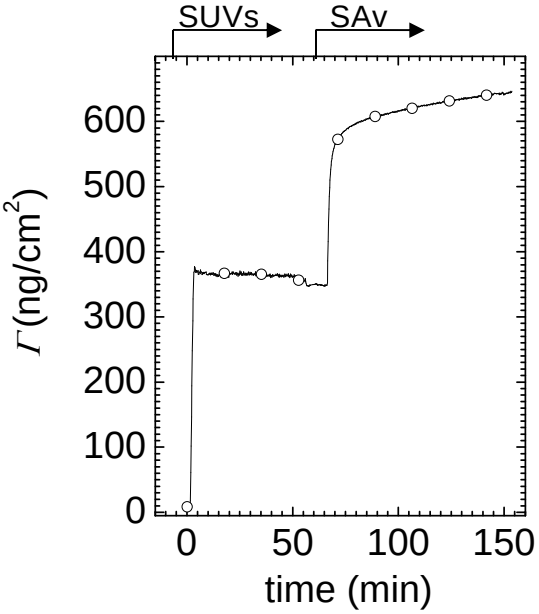

Figure 3.2 **Binding kinetics of b-SUVs and SAv by Ellipsometry**. Areal mass density, determined by ellipsometry, during the adsorption of b-SUVs and SAv. Sample incubation times are indicated by arrows.

An incubation protocol similar to the one used for the measurements in QCM-D was followed for the formation of the supported lipid bilayer and the streptavidin monolayer, with identical concentrations and 45 and 50 min of incubation time, respectively. Figure 3.2 shows the adsorbed amounts of biotinylated lipids during the process of SLB formation and of streptavidin. The areal mass density after incubation with lipids was 350 ng/cm^2, close to expected values for an SLB.[133] The areal mass density of SAv at the end of incubation was 294 ng/cm^2. Binding of SAv was stable to rinsing in buffer as expected already seen by QCM-D. In fact, close inspection of the binding curve revealed a small but steady mass increase even after rinsing (~0.36 ng/cm^2/min), the origin of which remains unclear.

Table 3.1 Areal surface mass density Γ, thickness L and ΔA determined by ellipsometry at the end of the respective sample incubation processes.

biomolecular layer	*SLB*	*SLB+SAv*	*HA*	*HA+aggrecan*
$\Delta A = A_{\text{film}} - A_{\text{buffer}}$	0.071	0.109	0.00018 [a]	0.00055 [a]
L (nm)	5.2	10.4	505	1080
Γ(ng/cm^2)	350	350+294	56	56+500

[a] The values for HA and aggrecan refer to the optical properties at the base of the layer with parabolic refractive index profile.

The adsorption kinetics of HA binding is shown in Figure 3.3**A**-**D**. HA (1083±60 kDa) was incubated at a bulk concentration of 20 μg/mL, and left to incubate for 100 min. The chamber was rinsed to remove unbound HA present in the bulk solution. Binding of HA was stable as expected for the biotin-streptavidin link. The thickness of the HA brush was 505 ± 18 nm, where the error corresponds to the confidence interval extracted with the fitting software. Several observations suggest that the error on the thickness is considerably larger, if one takes systematic measurement errors into account. First, L_{HA} was very sensitive to the choice of $L_{SLB/SAv}$. The value of L_{HA} = 505 nm was obtained when simultaneously fitting $L_{SLB/SAv}$. When $L_{SLB/SAv}$ was instead fixed to a value that deviated by as little as 0.4 nm (corresponding to the drift that we observed over a time scale of 1 h, or 22 ng/cm^2 of SAv) from the best fit, a thickness of 451 nm was obtained. Second, three different experiments under similar experimental conditions yielded brush thicknesses between 480 and 600 nm (*data not shown*). In Chapter 4, we had determined the thickness of an HA brush made with similar experimental conditions from a fit to experimental force curves with a model based on self-consistent mean-field theory that predicts a parabolic profile. The value with that approach was 619 nm, and the results are in reasonable agreement if one considers the large error associated with the determination of L_{HA} by ellipsometry.

The areal HA mass density after rinsing was 56 ng/cm^2. Based on a molecular mass of 1.083 MDa, the surface area per chain s^2 can be calculated as 3.2×10^3 nm^2, corresponding to s = 57 nm, which is in excellent agreement with the value of 57 nm obtained in Chapter 4 through the fitting of force curves.

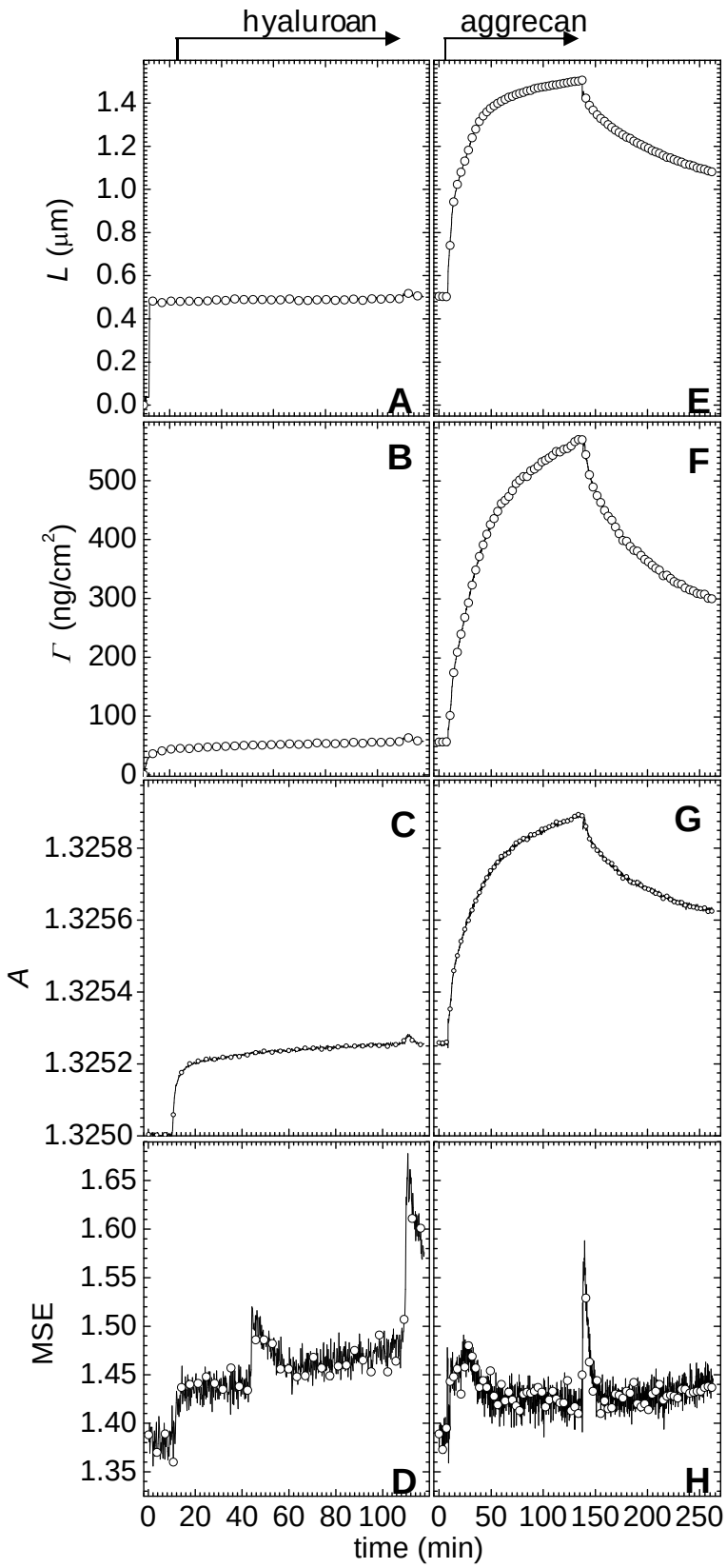

Figure 3.3 **Film thickness *L*, areal mass density Γ, first Cauchy parameter *A* and MSE values during incubation of HA and aggrecan, as measured by ellipsometry.** Incubation times are indicated by *arrows*. The reason for the jump in the MSE values in the binding of b-HA at 45 min is not known, but does not seem to have an impact on the determination of *A* and *L*.

Throughout the fitting, the mean-square error (MSE, Figure 3.3**D** and **H**) varied only moderately and it was always below 2. This indicates that the model can reproduce the data well (for an optimal fit, the MSE should scatter around 1).

In the next step, aggrecan at a bulk concentration of 500 μg/mL was introduced to the HA film and left to incubate. The thickness of the HA film with intercalated aggrecan after 2 hours of incubation was found to be approximately 1500 nm. Clearly, aggrecan induces a drastic swelling of the HA film. It is notable that the initial binding of aggrecan was slow when compared, for example, with the binding of streptavidin to an SLB. Even after 2 h of incubation, aggrecan binding did not reach equilibrium. Presumably, as more aggrecan molecules bind to the HA brush, steric hindrance increasingly limits the access of aggrecan to the HA film and slows the adsorption. The maximal bound amount of aggrecan was (Figure 3.3**E**-**F**) approximately 556 ng/cm^2 after 2 h of incubation. Based on an aggrecan molecular mass of about ~2.75 MDa[134] and the surface density of HA, this would correspond to an average of approximately 4 aggrecan molecules per HA chain.

The ellipsometric data confirmed the previous observation by QCM-D that binding of aggrecan to HA is reversible. Aggrecan binds to HA through its N-terminal G1 domain. The affinity of this interaction is rather weak (binding constants of 0.23 μM have been reported[135]). Binding can though be stabilized with the help of the so-called link protein through the formation of a ternary complex with HA and the aggrecan G1 domain. In our case, we did not use link protein and the reversible interaction is hence not surprising. The film thickness gradually decreased upon desorption of aggrecan, to approximately 1.1 μm at 2 h after rinsing. At this time, approximately 50% of the aggrecan had desorbed from the film.

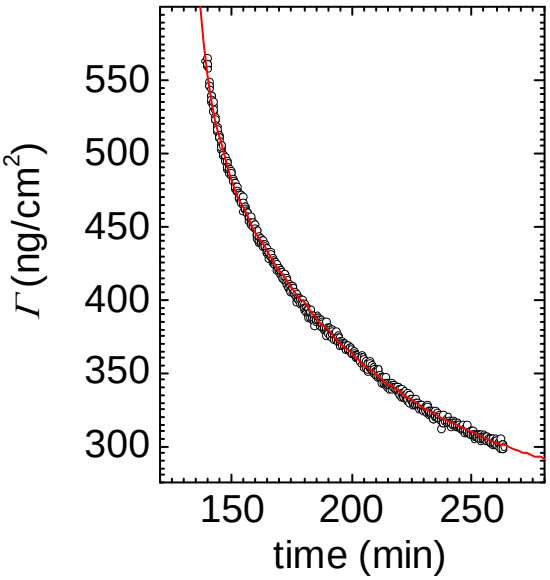

Figure 3.4 **Dissociation of aggrecan from HA brushes**. Desorption of aggrecan from HA films after rinsing with buffer. Experimental data (from Figure 3.3**F**, *circles*) are fitted by a double exponential (equation 3.1; *solid line*) to determine the desorption rate constant.

To estimate the dissociation rate of aggrecan, we fitted the areal mass density data (Figure 3.3**F** and Figure 3.4) after rinsing with a double exponential (Equation 3.1):

$$\Gamma = \Gamma^{(1)} e^{-k_{off}^{(1)} \Delta t} + \Gamma^{(2)} e^{-k_{off}^{(2)} \Delta t} \qquad [3.1]$$

where Γ is the areal mass density of aggrecan, Δt is the rinsing time, $k_{off}^{(1)}$ and $k_{off}^{(2)}$ are desorption rate constants and $\Gamma^{(1)}$ and $\Gamma^{(2)}$ the associated areal mass densities. The quality of the fit was good. The first dissociation rate constant was 8.5×10^{-4} s^{-1}. The second dissociation rate constant was 4.9×10^{-5} s^{-1}, that is, one order of magnitude smaller. The associated areal mass densities were $\Gamma^{(1)} = 123$ and $\Gamma^{(2)} = 430$ ng/cm^2, respectively, i.e. binding was dominated by $k_{off}^{(2)}$. In the simplest interpretation, one may associate the two different rate constants with two discrete unbinding processes. The data, however, is also consistent with the presence of a spectrum of unbinding processes with many different dissociation rates.

To confirm that aggrecan binds specifically to HA, we tested its interaction with a streptavidin monolayer in the absence of HA (Figure 3.5). Only a minor increase of less than 10 ng/cm^2 in the areal mass density was noticed which is negligible compared to the response on HA brushes.

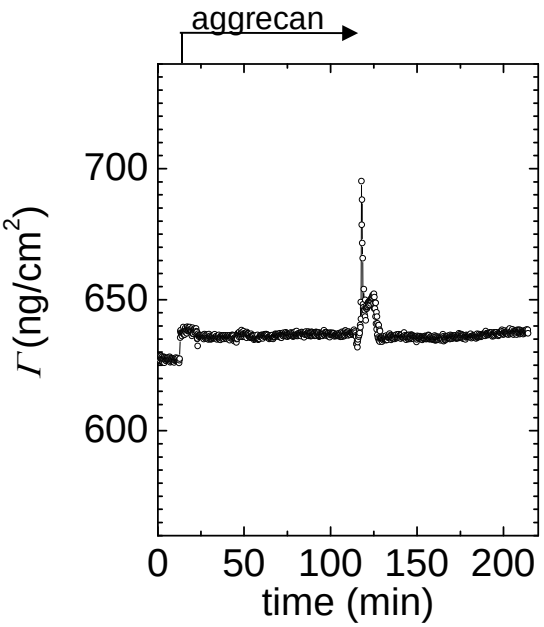

Figure 3.5 **Aggrecan does not bind to a streptavidin monolayer.** Exposure of aggrecan at 500 µg/mL to a SAv monolayer in the absence of HA led to minor adsorption (<10 ng/cm^2).

3.2.3 Effect of aggrecan on the compression of HA brushes

The impact of aggrecan on the resistance of HA brushes to compression was examined by the combined colloidal probe AFM/RICM setup. Aggrecan at a final concentration of 1 mg/mL was exposed to the HA film and left to incubate for one hour at physiological ionic strength of 150 mM NaCl, in a buffer with 10 mM HEPES and 3 mM NaN_3 at pH 7.4. Unbound aggrecan was then removed, and force curves were taken with approach and retract rates of 100 nm/s. The time between rinsing in buffer and acquisition of force curves was a few hours. Based on the ellipsometric data above, we estimate that the aggrecan content in the film corresponded to a few aggrecan molecules per HA chain. A representative force curve is shown in Figure 3.6. For comparison, a force curve on a pure HA brush is also shown (see Chapter 2, for details).

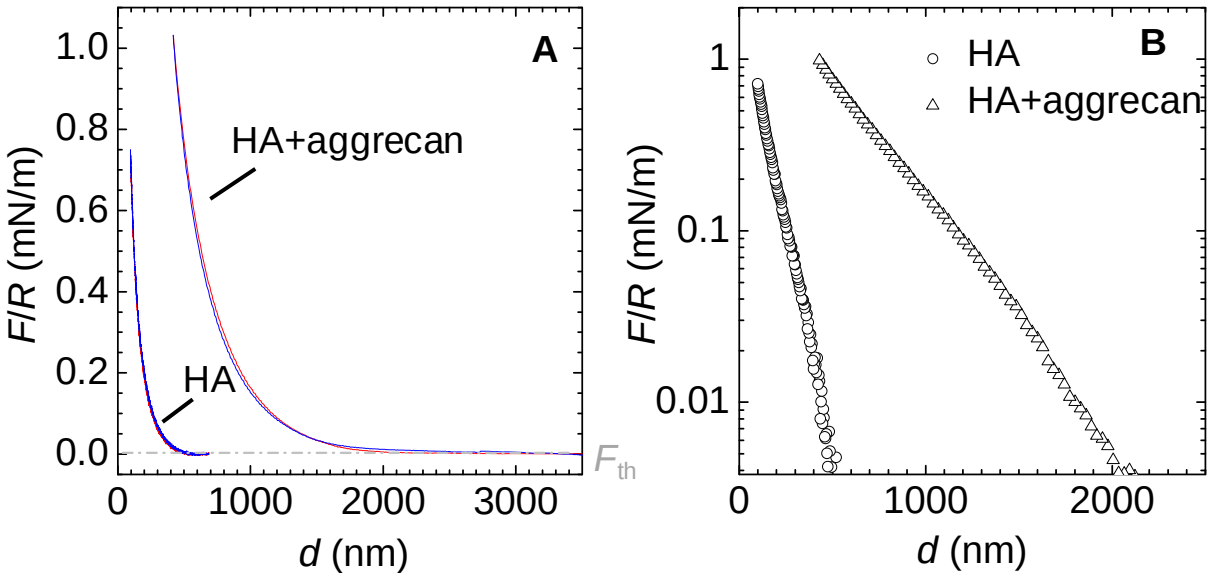

Figure 3.6 **Compressive response of HA films.** (**A**) Force *vs.* distance curves (approach - *red line*, retract - *blue line*) for the compression of a film of end-grafted HA, alone and with aggrecan, as indicated. The *grey dashed line* indicates the force threshold of 50 pN that was used to estimate the onset of repulsion and film thickness. (**B**) Approach data from **A** in a log-linear presentation (HA alone - *circles*, HA+aggrecan - *triangles*). Only data above the force threshold are presented. Data for HA alone was taken from Figure 2.6.

A remarkable increase in film thickness was observed after incubation of HA films with aggrecan. Repulsive interactions ≥50 pN started at a distance of $L = 2053 \pm 20$ nm, or about 4 fold more than what was observed on pure HA films. We did also observe a strong thickness increase by ellipsometry, although of lower magnitude (to 1500 nm). Clearly, the intercalation of aggrecan induced further stretching of the surface-grafted HA chains. There was also a strong enhancement in the resistance of the film to compression. At a distance of 420 nm (i.e. the point of closest approach for the aggrecan film), the compression force in the presence of aggrecan was more than 50-fold higher than for HA alone. As for pure HA films, the interactions were purely repulsive. Deviations between the approach and retract curves were significant but small, suggesting that the compression remained predominantly elastic. To check the reproducibility of the data, force curves were acquired repeatedly at the same spot and subsequently at different positions within 20 µm distance on the same surface. All curves were very similar, with differences not exceeding those shown between approach and retract curves in Figure 3.6**A**.

3.2.4 Mechanical properties of HA-aggrecan films

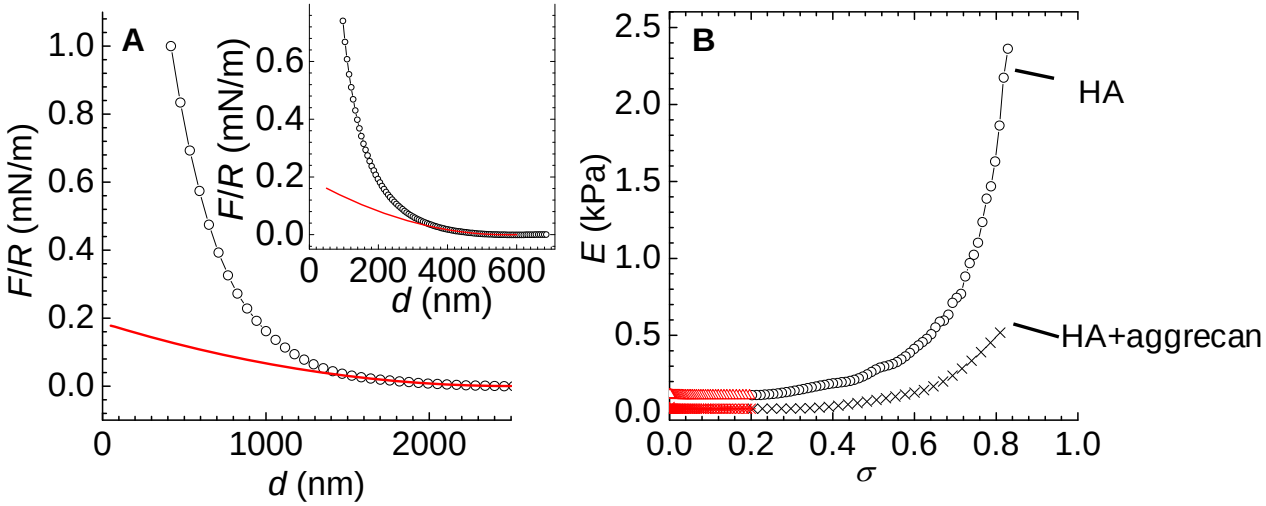

Figure 3.7 **Young moduli of HA-aggrecan composite films**: (**A**) Extrapolated fit with equation.3.2 (red solid lines) to a compression force profile (black solid line with circles) on an HA-aggrecan composite film (data from Figure 3.6). The fit over a range of d = 1992 to 2486 nm, for HA with aggrecan (corresponding to $\sigma < 0.2$) provided L = 2504 nm and E = 24 Pa. The inset shows the same fit for pure HA brushes for comparison. The fit provided L = 569 nm and E = 108 Pa for the fit range $\sigma < 0.2$. (**B**) Young modulus E *vs* strain σ for pure HA and composite HA-aggrecan films derived from the approach curves in Figure 3.6. Values for $\sigma < 0.2$ were obtained through the fit to equation.3.2 (symbols Δ and **),* values for $\sigma \geq 0.2$ as described in Chapter 2 (symbols *o* and *×* connected by *solid line*).

To obtain the Young modulus E at low compression (i.e. in the linear elastic regime) we fitted the force curves close to the onset of compression with:

$$F/R = \pi L E(1 - d/L)^2 \qquad [3.2]$$

The formula is derived from $E = P/\sigma$ with the pressure (or stress) P and the strain $\sigma = 1\text{-}d/L$. The compression energy between two co-planar surfaces can be derived from the compression forces in a sphere/plane geometry using Derjaguin's approximation as $W = F(d)/2\pi R$. Pressure is $P = \mathrm{d}W/\mathrm{d}d$. In the linear elastic regime, E is constant, and the fitting formula is obtained by integrating both sides of $E\sigma = P$ with respect to d, with the boundary condition $F(L) = 0$. Figure 3.7**A** shows an (extrapolated) fit to the approach curve on a HA-aggrecan composite film. Data up to 20% compression were fitted, giving E = 24 Pa and L = 2504 nm. The thickness obtained through the fitting was larger than the thickness obtained through the force threshold of 50 pN. We note that the selected fit range had a marked influence on the values of L and E, for example we obtained L = 2286 nm and E = 40 Pa with the fit over a range of d = 1440 to 1800 nm (*data not shown*). The inset shows the fit over a range of d = 453 to 570 nm for a pure HA film, giving E = 108 Pa and L = 569 nm.

At strains above 0.2, the fit underestimated the experimental data, indicating that the elastic response becomes non-linear. In this regime, stress can be determined from force as outlined in Chapter 2. The Young modulus as a function of strain is shown in Figure 3.7**B**, where L = 2504 nm was used to calculate the strain. Comparison with the data for pure HA brushes (L = 569 nm) shows that intercalaction of aggrecan makes the HA films somewhat softer: the Young's modulus decreases by 3-4 fold for all strains.

3.3 Discussion

3.3.1 Quantifying the amount of aggrecan in the HA films

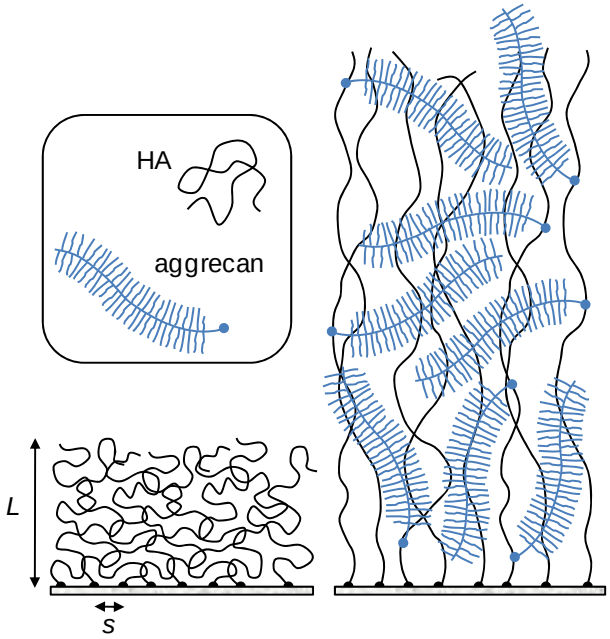

Figure 3.8 **Scheme of the putative morphology of HA brushes, alone or with aggrecan**. The cartoon is based on our data and the known molecular interaction between aggrecan and HA. Film thickness, the contour lengths of HA, aggrecan and its glycosaminoglycan (GAG) side chains are drawn approximately to scale. The diameter of the polymer chains, the grafting distance of HA and aggrecan´s GAG chains are enlarged for illustrative purposes.

We developed a model system where aggrecan, a negatively charged proteoglycan which plays a vital role in the mechanical properties of cartilage, is attached to a HA film via its G1 binding domain. At a first instance, the assembly of the model system was monitored using QCM-D. Formation of a supported lipid bilayer, a streptavidin monolayer and a HA brush were consistent with previously published results.[44] The QCM-D data provided first information about the kinetics and stability of aggrecan binding, and revealed that the film remained soft and hydrated upon proteoglycan incorporation. To complement the QCM measurements, in situ ellipsometry experiments were carried out. For quantitative data analysis, a new model was used that explicitly considers the parabolic density profile of the HA brush. With this model, we obtained a brush thickness and a grafting density in good agreement with the values obtained from the force measurements using combined colloidal probe AFM/RICM (Chapter 4). Incorporation and release of aggrecan proceeded rather slowly. Even after 2 h of incubation, the coverage remained sparse. . For comparison, maximal occupancies as high as one aggrecan per 20 nm HA chains have been reported for isolated complexes comprising HA, aggrecan and link protein.[136]

The incorporation of aggrecan drastically increased the thickness of our HA films. It is remarkable that the HA film swells by several times its original thickness, even though the aggrecan coverage remains rather sparse. Most likely, this change in morphology is driven by the intercalation of the bulky proteoglycan into the HA brush, as shown schematically in Figure 3.8: multiple aggrecan molecules can attach *via* their G1 domains to a given HA chain[136] and a combination of electrostatic repulsion and steric hindrance drives stretching of the HA chains. The result of this self-organization process is a hierarchical assembly, i.e. a planar brush of bottle brushes of bottle brushes. Such a conformation has been proposed in the past[3, 8, 128] for reconstituted pericellular coats around chondrocytes. Our *in vitro* reconstituted system provides evidence that the combination of grafted HA and aggrecan is indeed sufficient to generate such a hierarchical organization under near physiological conditions, and allowed to assess the mechanical properties of composite HA/aggrecan brushes.

3.3.2 Impact of aggrecan on HA brush mechanics

The mechanical properties of pure aggrecan assemblies have previously been investigated by Dean et al.[33, 137] In their case, aggrecan was covalently grafted *via* one end of its core protein to a planar support.[138] The resulting assembly is similar to our films in that a hierarchical brush (i.e. a planar brush of bottle brushes) is formed, although the number of hierarchical levels is one degree lower. The shape of the force-distance curves for pure aggrecan brushes is similar to what we found for pure HA and composite HA/aggrecan brushes: re-plotting Figure. 8 in ref. 33 on a log-linear

scale, one obtains a straight line, i.e. force depends approximately exponentially on distance. The elasticity of pure aggrecan brushes at a given strain was though more than 2 orders of magnitude higher.[33] Most likely, this difference is the result of a much higher packing density of the proteoglycan in the pure aggrecan brushes.[33] We note in passing that the force response for our HA/aggrecan brushes is very similar in shape and magnitude to what Sokolov et al.[114] measured by colloidal probe AFM on epithelial cells. The authors attributed this response to a combination of a polysaccharide-rich coat on the cell surface and cell membrane corrugations. The frequent occurrence of exponential force profiles for polysaccharide-rich films is intriguing, and deserves further investigation. HA/aggrecan assemblies are a key component of cartilage. At 90% compression, the pressure in our composite HA/aggrecan brushes would be ~0.5 kPa. This is up to four orders of magnitude weaker than the macroscopic pressure that can be attained in joint cartilage (up to 20 MPa),[139, 140] i.e. the HA/aggrecan film would become extremely compressed when exposed directly to the macroscopic pressure in joints. This implies that additional mechanisms must exist to absorb the compressive load. First, a fibrous collagen network with a rather large mesh size of typically several 100 nm is known to supplement the HA/proteoglycan meshwork in cartilage.[141] The microscale stiffness of the collagen network has been estimated to be on the order of 1 MPa,[142, 143] i.e. collagen could indeed carry most of the compressive load, and attenuate compression of the HA/proteoglycan meshwork.[143] Stolz et al.[142, 143] estimated a nanoscale stiffness of a few 10 kPa for the proteoglycan meshwork between the collagen fibres. This number approaches the young moduli measured in our brushes, although it is still more than an order of magnitude larger. Second, our reconstituted HA/aggrecan films lack a third component, cartilage link protein, that is known to stabilize the bond between aggrecan and HA.[144] Future studies that incorporate link protein into the model films should provide insight as to how strongly an increase in aggrecan density and film stability can enhance the compressive resistance of composite HA/aggrecan brushes. Third, peak pressures of 20 MPa in cartilage typically occur transiently under high strain rates. Under such non-equilibrium conditions, the resistance to pressure can increase drastically due to delayed drainage of water and ions.[141] Future studies at higher loading rates may provide interesting insight into the dynamics of fluid retention in HA films.

3.4 Conclusions

We have developed an *in vitro* supported lipid bilayer based model system to study the mechanical properties of HA-aggrecan composite films. An improved analysis method for ellipsometric data was applied that takes the parabolic density profile of the optically thick HA

brushes into account. The results from this analysis were consistent with those obtained by compression force measurements. We make use of the combined colloidal probe AFM and RICM that enables to probe the compression forces with tight control on the distance between the two surfaces to investigate the compressive response of films of grafted HA-aggrecan brushes. Incorporation of aggrecan, induced drastic film swelling and the formation of a hierarchical brush. The method represents a novel tool for the quantitative correlation between the supramolecular organization and the mechanical properties of surface-confined HA assemblies.

4. Films of end-grafted hyaluronan are a prototype of a brush of a strongly charged, semi-flexible polyelectrolyte with intrinsic excluded volume

To gain further insight into the physical phenomena that govern the mechanical behavior of HA assemblies, we have studied the response of films of end-grafted HA to compression over a large range of ionic strength. Compression forces were measured as a function of the absolute distance between a colloidal probe and the planar surface on which the HA film was constructed, using a combined atomic force microscopy and reflection interference contrast microscopy setup. The HA films were well defined in the sense that they are made of chains with a narrow size distribution that are grafted at controlled density to a solid support. Detailed comparison of the experimental data with analytical expressions derived from polymer and polyelectrolyte brush theory reveals that films of end-grafted HA behave as strongly charged polyelectrolyte brushes. In order to quantitatively reproduce the experimental data, intrinsic excluded volume interactions and chain stiffness of the polymer backbone must be taken into account. At low ionic strength, chains become almost fully stretched. In our experimental system, several micrometer thick films are formed that reach a hydration of up to 99.98%, and the brush thickness decreases by more than 5-fold with increasing ionic strength. More generally, the study provides quantitative theoretical predictions for the film thickness and compressive response as a function of HA length, grafting density and ionic strength.

4.1 Introduction

The polysaccharide hyaluronan (HA) is ubiquitous in the pericellular and extracellular space of vertebrates. It is also becoming increasingly popular in biomedical applications, as surface coating[145] and in tissue engineering.[146, 147] HA is a linear polymer of disaccharides, made of glucuronic acid and N-acetylglucosamine, that are linked via alternating β-1,4 and β-1,3 glycosidic bonds. Each disaccharide has a length of 1 nm,[148] and carries one chargeable group, in the form of a carboxylic acid. For polymeric HA, the pKa is approximately 3,[149] and HA is hence negatively charged above pH ≈ 3. *In vivo*, HA is expressed by HA synthases at the cell membrane and extruded into the extracellular space. These HA molecules have a molecular mass of typically a few million Daltons,[28] or a contour length of several micrometers. Once produced, they can stay grafted

to the synthases and/or bind to other HA receptors at the cell surface, such as CD44[123] and form so-called pericellular coats (PCCs), or they can be released into solution to serve other functions in the extracellular space. Numerous biological functions of PCCs[25, 112, 117, 150] and extracellular assemblies of HA in general (e.g. in cartilage) have been related to their mechanical properties. To better understand, how the mechanical properties of PCCs are connected to their supramolecular structure and dynamics, measurements on well-defined model systems that recapitulate the two-dimensional confinement and the self-assembly properties of the PCC are desirable.

In the present chapter, we systematically examine the influence of ionic strength, over a range from 50 μM to 500 mM NaCl, on the thickness and compressive mechanics of end-grafted HA films. To be able to access low ionic strengths, the measurements were performed in the absence of buffer. We compare experimental results with several theoretical models of polymer and polyelectrolyte brushes. By doing so, we confirm that films of end-grafted HA exhibit polyelectrolyte brush behavior and we are able to quantitatively predict the thickness and force response as a function of ionic strength, HA length and grafting density. Using the HA films as a well-defined experimental model, we also test how well the different theoretical approximations can reproduce the real data quantitatively.

For the experiment, we employed a setup that combines colloidal probe atomic force microscopy (AFM) and reflection interference contrast microscopy (RICM). With this setup, interaction forces can be quantified at the same time as the absolute distance between the colloidal probe and the substrate on which the brush was built.[151] The latter is not readily available by AFM alone, because the distance at closest approach remains unknown when analyzing polymer films. The combined setup provides the level of control on the absolute distance that is needed for a rigorous comparison of experiment and theory.

The employed theoretical models are based on different mean-field, self-consistent mean-field as well as scaling approaches as they have been developed throughout the past three decades. They provide a description of the morphology and force response of films of end-grafted polymers or polyelectrolytes as a function of general properties of the individual chains – contour length, charge density, stiffness, excluded volume – and the grafting density. Intentionally, the models are kept simple enough such that analytical expressions for the film thickness and for the compression forces as a function of inter-surface distance can be derived.

The particularity of HA is that it is a rather stiff polymer. From solution-based studies, persistence lengths between 4 and 8 nm have been reported,[105, 152-154] exceeding the size of the disaccharide repeat unit by 4 to 8-fold. In comparison, the intrinsic persistence length tends to be close to the monomer unit size for most water-soluble synthetic polymers and polyelectrolytes, and

for biopolymers such as single-stranded DNA or natively unfolded peptide chains. Hydrogen bonds between adjacent saccharide units and water caging of the glycosidic linkages have been proposed to be responsible for the increased stiffness of HA.[148]

As we will see, the intrinsic excluded volume (i.e. the volume from which a segment of a macromolecule effectively excludes all other segments of the same macromolecule or other macromolecules in solution) and the intrinsic stiffness of the polymer backbone are crucial for a satisfactory quantitative description of the properties of HA brushes. Therefore, and in contrast to earlier work by others[62, 126, 155, 156] and us[151] on the compression of planar polymer or polyelectrolyte brushes, we consider both parameters explicitly in our theoretical models. From fits to the experimental data, we can extract a refined value of the persistence length and estimate the intrinsic excluded volume of HA.

4.2 Results

4.2.1 Experimental data

HA was grafted to a streptavidin-coated glass-supported lipid bilayer *via* a biotin anchor at one of the ends of the HA molecules (see Chapter 6.4.3). The formation of the HA brushes proceeded in 150 mM NaCl. Compression forces as a function of absolute distance were measured with a setup that combines colloidal probe AFM and RICM *in situ* (see Chapter 6.4.1-2). The force-distance curve in Figure 4.1**A**, acquired in the presence of 100 mM NaCl, is representative in its qualitative features for all acquired force curves. First, the interaction was purely repulsive. Only in rare cases did we observe minor adhesion forces upon retraction (data not shown), indicating that adhesion of HA to the polystyrene did not affect the force curves appreciably. This is not surprising, given that both HA and polystyrene are negatively charged. Second, the approach and retract curves superposed very well, indicating that compression was purely elastic. Third, the force curves upon repeated compression of the same spot and upon compression of different spots on the same sample were highly reproducible: variations between curves were on the order of the line thickness of the curve in Figure 4.1**A**.

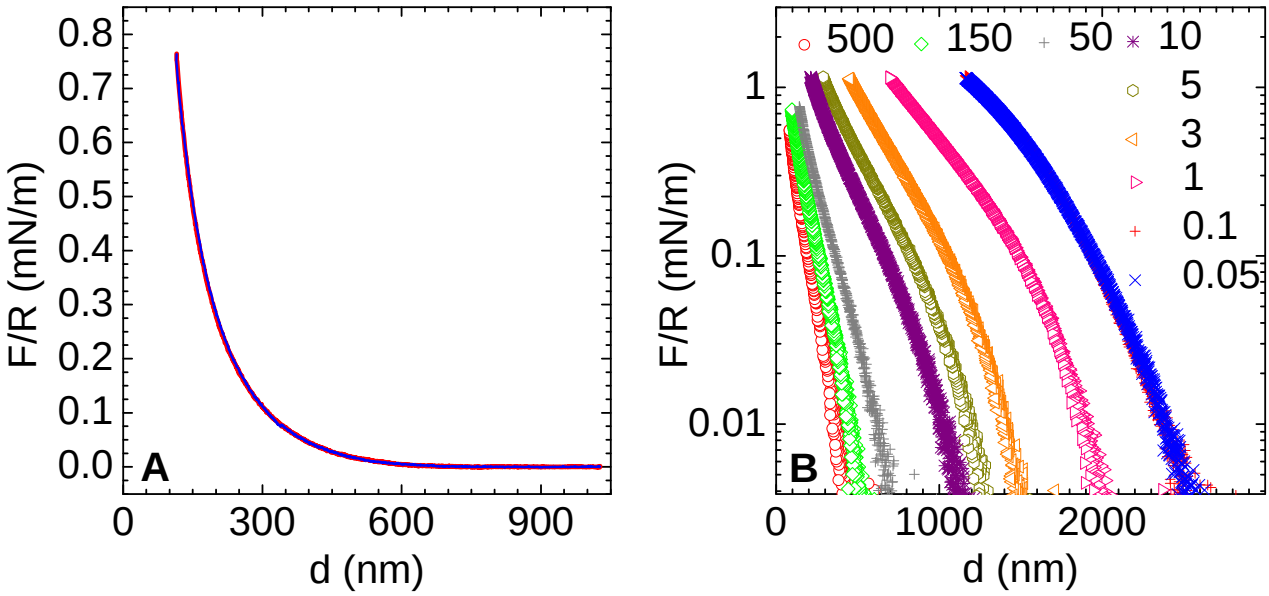

Figure 4.1 **Compression of HA films.** (***A***) Force-distance plot for a film of end-grafted HA at a bulk concentration of 100 mM NaCl, measured with the combined colloidal probe AFM/RICM setup. Approach (*red line*) and retract (*blue line*) curves overlap well, indicating that the compression is elastic. (***B***) Force-distance curves in log-linear presentation of the same HA film at various NaCl concentrations in the bulk solution. Only approach curves are shown; retract curves were identical. Forces rise above baseline at progressively larger distances with decreasing NaCl concentration. The forces required to reach a given distance do also increase monotonously with decreasing NaCl concentration. All forces are normalized by the radius *R* of the colloidal probe.

To study the influence of ionic strength on the conformation and compressive response, the HA brush was first incubated in ultrapure water and force curves were then acquired in water with gradually increasing NaCl concentrations, between 0.05 and 500 mM. After each addition step, the system was left for 8 to 10 min to equilibrate in the new ionic strength environment. Figure 4.1**B** shows selected approach curves. The interaction range and the forces required to compress the film to a given thickness decreased gradually with increasing salt concentration. To assess reversibility of the HA film's response to ionic strength, forces curves were taken on the same spot by switching the solution from 500 mM NaCl to ultrapure water and vice versa. The force curves at 500 mM NaCl before and after exposure to ultrapure water were similar, indicating that the salt-dependent collapse and swelling of HA films was fully reversible (data not shown). In the following, we will analyze the ensemble of force curves in the context of polymer and polyelectrolyte brush theories.

4.2.2 Brush thickness

To rationalize the response of HA brushes to compression, we start by examining the dependence of the interaction range on ionic strength. To quantify the interaction range *L* in a simple way, we determined the distance *d* at which the repulsive force increased beyond a threshold

level of F_{th} = 50 pN. The choice of this threshold is somewhat arbitrary. It is dictated by the force resolution of our experimental data, i.e. slightly above noise level. L is also a first measure for the thickness of the HA brush. With increasing salt concentration, L decreased monotonically (Figure 4.2). This is not unexpected: the hyaluronan chains are charged, and with increasing ionic strength the electrostatic interactions are increasingly screened, i.e. inter-chain repulsion decreases. Close inspection of the data reveals three regimes. At low ionic strength (≤ 0.5 mM NaCl) the brush thickness is approximately constant. The measured thickness, about 2.5 µm, was remarkably close to the contour length of HA (2.86±0.15 µm), indicating that at least a part of the chains became very strongly stretched. At higher ionic strength (≥ 1 mM NaCl) the thickness decreased gradually. Up to 150 mM NaCl, the decrease in the log-log plot in Figure 4.2 is well-approximated by a straight line with slope -0.26 (not shown), i.e. there is an apparent power-law dependence between brush thickness and ionic strength. Above 150 mM, the salt-dependence of thickness becomes progressively weaker.

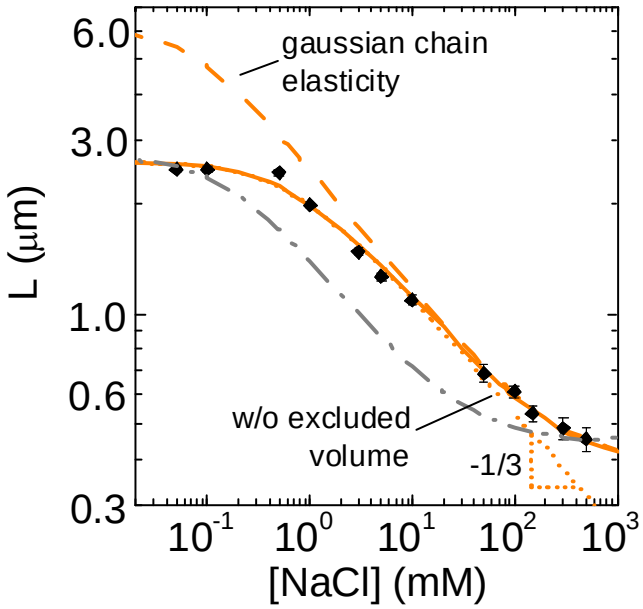

Figure 4.2 **Brush thickness as function of bulk NaCl concentration.** HA brush thicknesses L were obtained from the force-distance curves in Figure 4.1**B** and additional curves on the same HA film (*not shown*), using a force threshold of F_{th} = 50 pN (*black lozenges*). Error bars relate to noise of the data. The *solid line* is a fit with Equation 3.4.3A for s = 57 nm and p = 14, yielding A_1 = 1.1 and $A_2\nu_0$ = 1.8 nm^3. The *dashed line* was simulated using the same parameters but assuming Gaussian chain extensibility (Equation 4.4.3B). The *dotted line* was simulated using Equation 4.4.3A with ν_0 = 0. Finite chain extensibility and intrinsic excluded volume significantly affect the data at low and high salt concentrations, respectively. The best fit with Equation 4.4.3B (*grey dash-dotted line*, obtained with A_1 = 0.2 and $A_2\nu_0$ = 2.6 nm^3) clearly cannot reproduce the experimental data.

Qualitatively, these three regimes match with theoretical predictions for polyelectrolyte brushes.[84, 88, 157, 158] For brushes of sufficiently high charge and grafting density, essentially all counterions can be considered trapped inside the brush.[158] At low added salt, the brush thickness is then determined by the balance between the osmotic pressure of the trapped counterions and the entropic losses upon stretching of the HA chains.[84] In this "osmotic brush" regime,[88] the brush thickness is virtually unaffected by ionic strength. Added salt will affect the brush thickness when the ionic strength of the solution becomes larger than the concentration of mobile counterions inside the brush. In this "salted brush" regime,[88] the thickness decreases with increasing ionic strength, as the electrostatic interactions between chain segments become partially screened. Here, theory predicts a power law dependence on the external salt concentration with an exponent of -1/3,[84, 88, 158] as long as intrinsic excluded volume interactions can be neglected. Towards high salt concentrations, when the electrostatic interactions become increasingly screened, the excluded volume of the polymer backbone will increasingly determine the brush behavior. A positive excluded volume leads to an increased thickness and towards very high salt concentrations, the "quasi-neutral brush" regime, a plateau would be expected.[88, 159, 160] Even though this plateau is not attained experimentally, the progressive deviation from the power law between 150 and 500 mM NaCl (Figure 4.2) provides a first indication that HA exhibits a positive intrinsic excluded volume.

For a quantitative fit of the experimental results for the brush thickness and compression force profiles as a function of added salt concentration, we apply a mean-field theory of polyelectrolyte brushes. The approach[161, 162] is based on representing the (Helmholtz) free energy of the brush confined between two planar surfaces as:

$$E(d) = E_{\text{ion}}(d) + E_{\text{ev}}(d) + E_{\text{elastic}}(d) \qquad [4.1]$$

where E_{ion}, E_{ev} and E_{elastic} are the contributions of ionic and excluded volume interactions and of the conformational entropy of the chains, respectively, and d is the distance between the surfaces. Below, we use mostly an approximation that assumes equal and uniform stretching of the chains, implying a constant monomer density within the brush ("box profile"). However, in our discussion of the compression force profiles we shall also refer to results of the more advanced self-consistent mean-field theory of polymer[80, 106, 107, 163, 164] and polyelectrolyte[83, 158] brushes.

Within the box-profile approximation, the brush is characterized by its thickness d or, equivalently, by the concentration $c = l_c/(bs^2d)$ of monomer units in the brush. Here, l_c and b are the contour length and the monomer unit length, respectively. s is the characteristic spacing between adjacent grafting points, or s^2 the surface area per chain. The thickness L of the free (uncompressed) brush is found from minimization $[\partial E(d)/\partial d]_{d=L} = 0$ of the free energy given in Equation 4.4.1.

The box-profile approximation for polyelectrolyte brushes is usually coupled to the local electroneutrality approximation (LEA), introduced in ref. 157. The LEA assumes that the charge density created by monomer units of grafted polyelectrolyte chains is locally compensated by the (excess) concentration of mobile counterions. It is assumed that the brush is in equilibrium with the reservoir of solvent with fixed concentration c_s of monovalent salt ($2c_s$ is the number of positively and negatively charged ions per unit volume).

The ionic contribution to the free energy (per unit surface area) is presented as:[161]

$$E_{\mathrm{ion}}(d)/kT = \frac{\alpha l_{\mathrm{c}}}{bs^2}\left(\frac{1-\sqrt{1+\left(\frac{\alpha c}{2c_{\mathrm{s}}}\right)^2}}{\frac{\alpha c}{2c_{\mathrm{s}}}} + \operatorname{arcsinh}\frac{\alpha c}{2c_{\mathrm{s}}}\right), \qquad [4.2A]$$

with α the fractional charge per monomer unit length. $kT = 4.1\times10^{-21}$ J is the thermal energy (at 25°C). The free energy of excluded volume interactions is presented as:

$$E_{\mathrm{ev}}(d)/kT = \frac{l_{\mathrm{c}}}{bs^2} v_0 c, \qquad [4.2B]$$

if we consider binary interactions but neglect higher order interactions. $v_0 = A_{v_0} b^3$ is the "bare" excluded volume (second virial coefficient) of a monomer unit. A_{v_0} is a numerical prefactor of order unity that depends on the monomer unit shape and the solvent quality. Gaussian chain elasticity:

$$E_{\mathrm{elastic}}(d)/kT \approx 3d^2/(2l_{\mathrm{c}}pbs^2) \qquad [4.2C]$$

provides a good approximation for the elastic contribution at moderate stretching. Here, the ratio $p = a/b \geq 1$ characterizes the intrinsic chain stiffness, or the anisotropy of the intrinsic statistical (Kuhn) segment of the uncharged chain, where a is the segment length. Because our HA chains become close-to-fully stretched towards low ionic strength, finite chain extensibility needs to be considered.[159, 160, 165] To this end, we follow an approach suggested by Chen et al.[159] and use the elastic term in the form of a finitely extendible nonlinear elastic (FENE) potential, which we chose as:

$$E_{\mathrm{elastic}}(d)/kT = -3l_{\mathrm{c}}/(2pbs^2) \times \ln[1-(d/l_{\mathrm{c}})^2]. \qquad [4.2D]$$

At weak chain extension ($d \ll l_{\mathrm{c}}$) it is equivalent to Equation 4.2C, and its derivative describes linear Hooke's law for elastic chain elongation. However, the elastic term given by Equation 4.2D and its derivative diverge at $d \to l_{\mathrm{c}}$. Hence, the corresponding elastic force tends to infinity and prevents chain stretching beyond the contour length. We remark, that Equation 4.2D as well as a

similar expression used by Chen et al.[159] $E_{\mathrm{elastic}}(d)/kT = -l_c/(pbs^2) \times \{(d/l_c)^2/2 - \ln[1-(d/l_c)^2]\}$ capture the effect of finite extensibility, but lead to a stronger increase in the elastic force upon approaching the $d \to l_c$ limit, $\partial E_{\mathrm{elastic}}/\partial d \propto (1-d/l_c)^{-1}$, than rigorous treatments in the freely-jointed chain (where $\partial E_{\mathrm{elastic}}/\partial d \propto \mathrm{L}^{-1}(d/l_c)$, with the inverse Langevin function $\mathrm{L}^{-1}(x)$) or the worm-like chain models.

Minimization of the free energy defined by Equations 4.4.1 and 4.4.2A, B and D leads to an expression for the thickness L of the uncompressed brush:

$$\left\{2A_2c_s\left[\sqrt{1+\left(\frac{\alpha c}{2c_s}\right)^2}-1\right]+A_1v_0c^2-\frac{3}{pbs^2}\frac{d/l_c}{1-d^2/l_c^2}\right\}_{d=L}=0, \qquad [4.3A]$$

in which we have also introduced two numerical prefactors, A_1 and A_2. At this point, it is worth reminding that the local electroneutrality and box-profile approximations enable reproducing correctly the trends in terms of the dependence of brush thickness on brush architectural parameters and salt concentration. However, the internal structure of the brush (i.e. the distribution of the polymer density) as well as the distribution of co- and counterions between the interior of the brush and the adjacent solution are not taken properly into account. Therefore, one should not expect that these approximations provide an exact quantitative description of any experimentally measurable brush thickness. The empirical adjustable parameters A_1 and A_2 were introduced to account for these limitations. They ensure matching of the measured brush thickness at high (A_1) and at low (A_2) salt concentrations, when the brush swells predominantly due to excluded volume repulsions or osmotic pressure of counterions, respectively. A similar approach has been taken by Chen et. al.[159] for fitting results from molecular dynamics simulations, with the difference, that v_0 was used as an adjustable parameter instead of A_1.

For the HA brushes, we employed the following values. $b = 1.0\mathrm{nm}$ is the length of a disaccharide unit.[148] l_c = 2860±150 nm can be calculated from the polymer molecular weight (1083±53 kDa), and the length and molecular weight (378 Da) of the disaccharide repeat unit. Each disaccharide has one chargeable group - a carboxyl group on the glucuronic acid – which is likely to be fully ionized under the experimental conditions. Counterion condensation[166] is unlikely, because the distance between chargeable groups is larger than the Bjerrum length (0.7 nm in aqueous solution), i.e. $\alpha = 1$. $p = a/b$ is expected to lie between 8 and 16, based on the equivalence of a in the freely-jointed chain and $2l_p$ in the worm-like chain models, and reported persistence lengths l_p between 4 and 8 nm.[105, 152-154] In earlier work,[44] we had estimated $s \approx 56\mathrm{nm}$ by reflectometry.

Based on results that will be exposed further below, we fix $p = 14$ and $s = 57\text{nm}$. This leaves the product $A_1\nu_0$ and A_2 as the only fitting parameters. We obtained an excellent fit over the entire range of ionic strengths (Figure 4.2, *solid line*), with $A_1\nu_0 = 1.8$ nm^3 and $A_2 = 1.1$. To illustrate the impact of finite chain extensibility and excluded volume interactions, two simulated curves that neglect either one effect or the other were included in Figure 4.2 (*dashed* and *dotted line*, respectively). For Gaussian chain elasticity, Equation 4.3A simplifies to:

$$\left\{2A_2c_s\left[\sqrt{1+\left(\frac{\alpha c}{2c_s}\right)^2}-1\right]+A_1v_0c^2-\frac{3}{pbs^2}\frac{d}{l_c}\right\}_{d=L}=0. \qquad [4.3B]$$

Excluded volume interactions were neglected by setting $v_0 = 0$ in Equation 4.3A. The effect of finite chain extensibility is noticeable below 5 mM NaCl, or above 50% stretching. Above 30 mM NaCl, on the other hand, excluded volume interactions have an appreciable impact on the brush thickness. Comparison of simulated and fitted curves suggests that the apparent power law behavior with exponent -0.26 that we observed experimentally is the result of the gradual increasing impact of finite chain extensibility towards low ionic strength and excluded volume interactions towards high ionic strength.

To assess the discriminative power of the fit method, we did also attempt to fit the experimental data with Equation 4.3B. In this case, no satisfactory fit could be obtained: theory and experiment could be matched at the lowest and highest salt concentrations, by adjusting $A_1\nu_0$ to 2.6 nm^3 and A_2 to 0.2, but the theory then underestimated the thickness at intermediate salt concentrations by up to 35% (Figure 4.2, *grey dash-dotted line*). It is noticeable that the transition to the osmotic brush plateau is sharper when finite chain extensibility is taken into account. With $L = 2.5$ µm and $s = 57$ nm, the counterion concentration inside the brush would be 0.5 mM. This number is in good agreement with the salt concentration at which the osmotic brush plateau is seen to start experimentally and in the fit with Equation 4.3A (but not 4.3B). The remarkable quantitative agreement between experiment and theory therefore provides strong evidence that finite chain stretching and excluded volume repulsion are important determinants in the behavior of HA brushes.

4.2.3 Compression force profiles

For a brush on a planar surface, the compression force $F(d)$ by a sphere of radius $R \gg L$ is related to the energy of compression $E(d) - E(L)$ by a plane *via* the so-called Derjaguin approximation:[62]

$$F(d)/R = 2\pi[E(d) - E(L)]. \quad [4.4]$$

4.2.3.1 Forces profiles at high ionic strength (salted brush)

At high salt concentrations ($\alpha c \ll c_s$), Equation 4.2A reduces to $E_{ion}(d)/kT = l_c/(bs^2)\,\alpha^2/(4c_s)\,c$. Consequently, $[E_{ev}(d) + E_{ion}(d)]/kT = l_c/(bs^2)\,[v_0 + \alpha^2/(4c_s)]c$, and one can introduce the "effective" excluded volume $v = v_0 + \alpha^2/(4c_s)$, which accounts (within the accuracy of the mean-field approximation) for superposition of the "bare" excluded volume interactions and partially screened Coulomb repulsion between the charges on the HA chains. It follows that:

$$p^2 v = p^2\left(v_0 + \frac{\alpha^2}{4c_s}\right) = a^2\left(A_{v_0} b + \frac{\alpha^2}{4b^2 c_s}\right). \quad [4.5]$$

Furthermore, the chains are only moderately stretched at high ionic strength (Figure 4.2), and elastic stretching is hence well-described by Gaussian chain elasticity (4.2C). With the simple box-profile (BP) approximation, we obtain from Equations 4.1, 4.2B and 4.2C:

$$\frac{F}{R} = C_{\text{MFT-BP}}\left[\frac{L}{d} + \frac{1}{2}\left(\frac{d}{L}\right)^2 - \frac{3}{2}\right] \quad \text{with} \quad C_{\text{MFT-BP}} = 6\pi\frac{L_{\text{MFT-BP}}^2 kT}{pbs^2 l_c} \text{ and} \quad [4.6A]$$

$$L_{\text{MFT-BP}} = \left(\frac{1}{3}\right)^{1/3}\left(\frac{pv}{bs^2}\right)^{1/3} l_c. \quad [4.6B]$$

More advanced self-consistent mean-field theory for neutral brushes predicts a monomer density profile that, in good solvent, has the form of an inverted parabola with its maximum at the grafting surface ("parabolic profile", PP). This approach, developed independently by Zhulina et al.[107] and by Milner et al.[80, 164], gives:

$$\frac{F}{R} = C_{\text{MFT-PP}}\left[\frac{L}{d} + \left(\frac{d}{L}\right)^2 - \frac{1}{5}\left(\frac{d}{L}\right)^5 - \frac{9}{5}\right] \quad \text{with} \quad C_{\text{MFT-PP}} = \frac{\pi^3}{4}\frac{L_{\text{MFT-PP}}^2 kT}{pbs^2 l_c} \quad \text{and} \quad [4.7A]$$

$$L_{\text{MFT-PP}} = \left(\frac{8}{\pi^2}\right)^{1/3}\left(\frac{pv}{bs^2}\right)^{1/3} l_c. \quad [4.7B]$$

From the above equations, it is clear that the uncompressed brush thicknesses in the MFT-PP and MFT-BP models are not identical, but related by $L_{\text{MFT-PP}} = 1.34 L_{\text{MFT-BP}}$.

Another approximation for neutral brushes, based on scaling theory (ST) and historically the first approach, is the one by Alexander and de Gennes.[79] This model also assumes a box profile. The

contributions to the free energy are $E_{\mathrm{ev}}(d)/kT \cong 4/5\, s^{-2}\, l_{\mathrm{c}}/b\, (pv/b^3)^{3/4}(cb^3)^{5/4}$ and $E_{\mathrm{elastic}}(d)/kT \cong 4/7\, s^{-2}(l_{\mathrm{c}}/b)^{-1}(d/b)^2(c/pv)^{1/4}$, and:[55, 62]

$$\frac{F}{R} = C_{\mathrm{ST}}\left[7\left(\frac{L}{d}\right)^{5/4} + 5\left(\frac{d}{L}\right)^{7/4} - 12\right] \quad \text{with} \quad C_{\mathrm{ST}} = A_F\,\frac{L_{\mathrm{ST}}kT}{s^3} \quad \text{and} \qquad [4.8A]$$

$$L_{\mathrm{ST}} = A_L\left(\frac{pv}{bs^2}\right)^{1/3} l_{\mathrm{c}}. \qquad [4.8B]$$

A_F and A_L are numerical prefactors of order unity that are *a priori* unknown, i.e. they cannot be determined by the theory alone.[1] Equation 4.8A is similar to 4.6A, though the exponents of the power law dependences of different terms on the ratio d/L are slightly different. This is because Equation 4.8A accounts for local correlations in polymer density inside the brush, which are essential under good solvent conditions for flexible chains, but are disregarded by the mean field theories. The mean-field approximation, however, applies at marginally good solvent for semi-flexible chains.[167]

The full self-consistent field Poisson-Boltzmann theory describing the structure of a polyelectrolyte brush at arbitrary salt concentration without any pre-assumption concerning ion distribution was developed in ref. 158. However, this theory does not allow for a closed analytical expression for the free energy of the compressed polyelectrolyte brush (in the presence of salt). Therefore, for fitting the experimental results, we used expressions obtained for a neutral brush under good solvent conditions, replacing the excluded volume parameter by the effective salt-dependent second viral coefficient, Equation 4.5. This approach is expected to be accurate at high salt concentrations, when the "electrostatic excluded volume" becomes comparable to (or smaller than) the bare excluded volume. However, we expect that its extrapolation to moderate salt concentrations does not lead to major quantitative discrepancies.

[1] The equivalent of Equation 4.8A is often presented[55, 62] with a prefactor of $8\pi/35$, or $16\pi/35$ if both interacting surfaces are coated with a brush, in addition to an unknown numerical prefactor of order unity. For simplicity, and given that $8\pi/35 \approx 0.72$ is close to unity, we have lumped this prefactor into A_F. Also, it can be seen by comparing Equations 4.6B and 4.8B that the relationship between the unperturbed brush thicknesses in the MFT-PP and ST models cannot be quantitatively predicted from theory alone, because A_L is unknown. In the literature[55, 80, 155] a factor of $(24/\pi^2)^{1/3} \approx 1.34$ has repeatedly been proposed, presumably due to confusion between the MFT-BP and ST approaches.

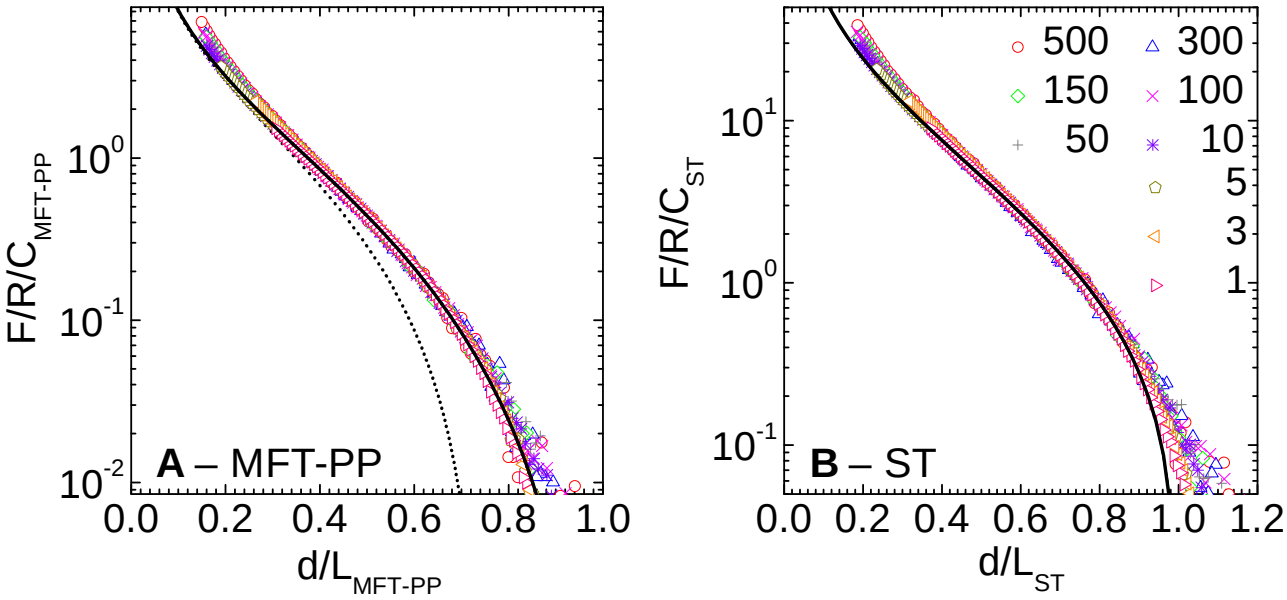

Figure 4.3**Application of theoretical models to salted HA brushes.** Plots of normalized forces *vs.* normalized distances of HA films for salt concentrations ≥1 mM NaCl. The experimental curves from Figure 4.1**B** and additional data at other ionic strengths were fitted with Equations 4.4.7A (MFT-PP model; ***A***) and 4.4.8A (ST model; ***B***) over the range $0.5 < d/L < 1$ (with L estimated through the force threshold F_{th}). Distances d were normalized by the brush thicknesses $L_{MFT\text{-}PP}$ and L_{ST}, and forces F/R were normalized by the prefactors $C_{MFT\text{-}PP}$ and C_{ST}, respectively, as obtained from the fitting of each individual force-distance curve. Symbols represent experimental data >50 pN at different salt concentrations (listed in ***B***); *solid black lines* are extrapolated fits. In these normalized presentations, all experimental data fall on a single curve. At low and medium compression, the MFT-PP model fits the data very well; while the ST model shows systematic deviations at low compression ($d/L > 0.9$). Both models underestimate the data at high compression ($d/L < 0.4$). The *dotted line* in ***A*** is simulated data, based on Equation 4.4.6A (MFT-BP model) and the results of the MFT-PP model.

To compare experiment and theory, we fitted our force curves with Equations 4.7A and 4.8A over the range of weak to moderate compressions. The approximation of ionic interactions by an effective excluded volume is expected to become increasingly inaccurate with increasing compression and decreasing ionic strength. Data below $d/L = 0.5$ (with L determined through the force threshold F_{th}) and force curves at ionic strengths <1 mM NaCl were therefore not included in the fit. Experimental approach curves at all tested ionic strengths ≥1 mM NaCl with the fits are displayed in Figure 4.3. To facilitate comparison, F/R was normalized by the prefactors, $C_{MFT\text{-}PP}$ and C_{ST}, respectively, and d was normalized by $L_{MFT\text{-}PP}$ and L_{ST}, respectively. The normalized force curves revealed a curve shape independent of ionic strength. The MFT-PP model fitted the data at weak and moderate compression very well, but systematically underestimated the data at strong compression. The ST model fitted the data at moderate compression well, but systematically underestimated the data at weak and strong compression. To illustrate the importance of the

parabolic density profile in the mean-field theory, an additional curve that was simulated with Equation 4.6 and the results from the fit to Equation 4.7A is displayed as a dotted line in Figure 4.3**A**. The simulated MFT-BP curve agrees well with the fitted MFT-PP curve at strong compression, but deviates significantly at weak and moderate compressions. Also, we found the fits with the MFT-BP model to reproduce the experimental data less well than the MFT-PP or ST models (*not shown*), and therefore do not further consider the MFT-BP model.[2]

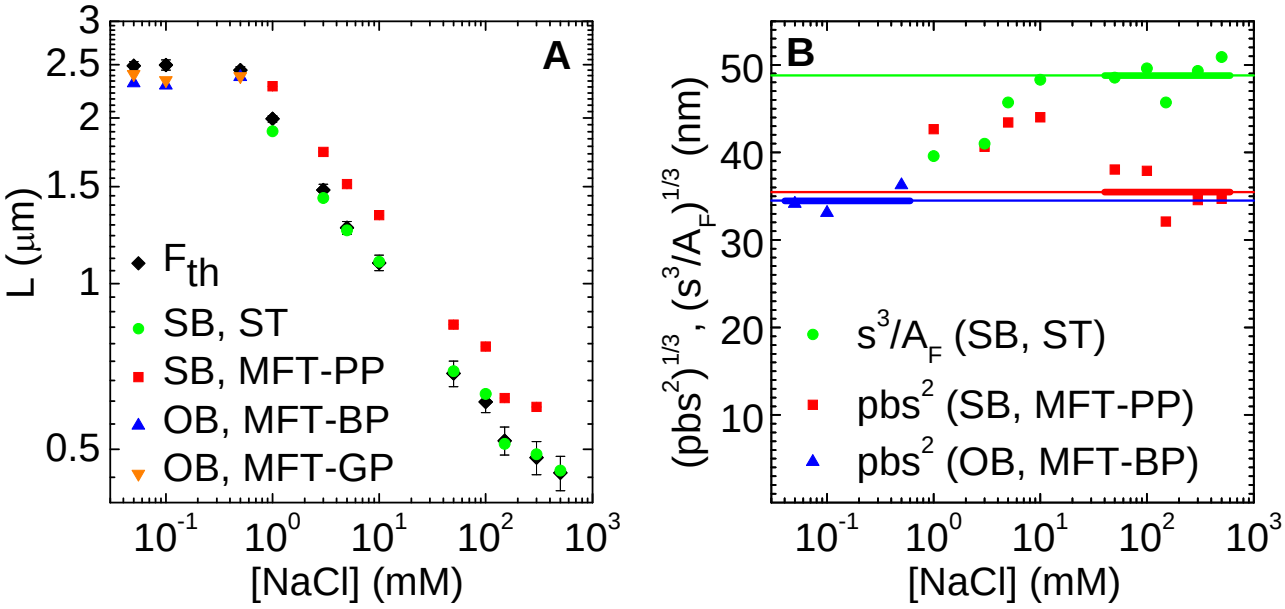

Figure 4.4 **Parameters extracted from the fits of theoretical models to salted and osmotic HA brushes.** (***A***) Film thickness, obtained with the ST (*green circles*) and MFT-PP (*red squares*) models for salted brushes (SB), and with the MFT-BP (*blue triangles*) and MFT-GP (*orange triangles*) models for osmotic brushes (OB). Confidence intervals were smaller than the symbol size. Brush thicknesses obtained *via* F_{th} = 50 pN (*black lozenges*, from Figure 4.2) are shown for comparison. (***B***) Cube roots of s^3/A_F (*green circles*) and pbs^2 (*red squares*, *blue triangles*), extracted through the three different models, respectively. Mean values (*solid lines*) were determined from data at ≥50 mM NaCl for salted brushes and ≤0.5 mM NaCl for osmotic brushes (fitting range indicated by *thick solid lines*).

Figure 4.4 displays the results of the fits. With l_c being known, the parameters $L_{MFT\text{-}PP}$ and pbs^2 could be extracted *via* Equation 4.7A, and L_{ST} and s^3/A_F *via* Equation 4.8A. The brush thicknesses (Figure 4.4**A**) determined with the MFT-PP model were typically about 20% larger than the values extracted *via* F_{th} = 50 pN, suggesting that forces as low as 50 pN do already induce appreciable compression. This is also readily apparent in Figure 4.3**A**, where the range of the experimental data is essentially confined to $d < 0.85\ L_{MFT\text{-}PP}$. The agreement between the values derived from the ST

[2] The quality of the fit improves when introducing additional numerical prefactors, analogous to what we did in Equation 4.3. This approach has been taken by others[156] to fit polyeletrolyte brush compression data.

model and *via* F_{th}, respectively, was excellent. This is likely to be coincidental, given that the choice of F_{th} is arbitrary. Notably, the ratio between $L_{MFT\text{-}PP}$ and L_{ST} did not depend on ionic strength, indicating that A_L is indeed constant as expected. With $L_{MFT\text{-}PP}/L_{ST} = 1.20\pm0.01$, and by comparing Equations 4.7B and 4.8B, we find $A_L = 0.78$, which is close to unity as expected.

pbs^2 and s^3/A_F (Figure 4.4**B**; cubic roots of both values are displayed to facilitate operation with numbers of unit length) scattered appreciably, but exhibited only a weak (if any) systematic dependence on ionic strength. Within the limits of validity of the effective excluded volume approximation, this is indeed expected because both p, b, s and A_F are constant in the experiment.

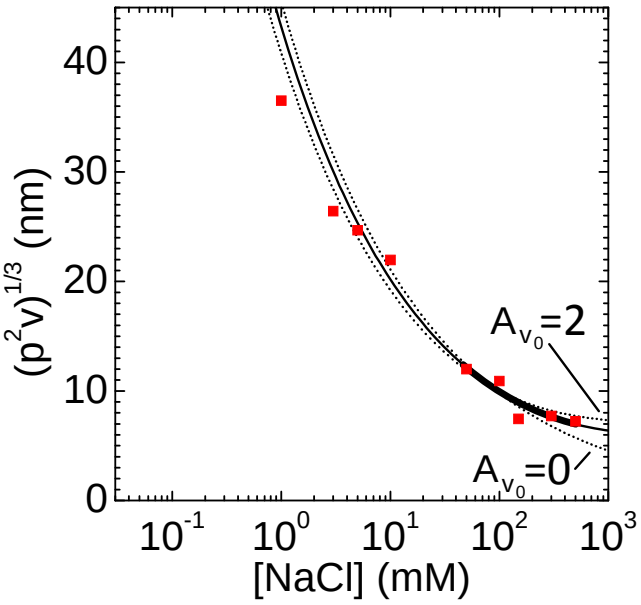

Figure 4.5 **Parameters extracted from the fits of theoretical models to salted HA brushes.** Cube root of p^2v (*red squares*), extracted with the MFT-PP model for salted brushes. Equation 4.4.5 was fitted to data at ≥50 mM NaCl (*thick solid line*) and extrapolated (*thin solid line*), giving $p = 13.9$ nm and $A_{v_0} = 0.9$. Extrapolated fits with A_{v_0} fixed to 0 and 2 (*dotted lines*) give $p = 15.0$ and 12.8, respectively.

Figure 4.5 displays (the cubic root of) p^2v, which was determined *via* Equation 4.7B from $L_{MFT\text{-}PP}$, pbs^2 and l_c without any further input parameters, as a function of ionic strength. To obtain estimates of the statistical segment length a and the prefactor A_{v_0}, we fitted this data to Equation 4.5. To avoid bias by the decreasing accuracy of the effective excluded volume approximation at low ionic strength, only the five data points at ≥50 mM NaCl were fitted. The fit (Figure 4.5, *thick solid line*) gave $a = 13.9\pm1.6$ nm and $A_{v_0} = 0.9 \pm 1.2$. The result for a is well constrained, as can be seen from the errors, and in good agreement with the range of 8 to 16 nm that has been reported in the literature.[105, 152-154] Molecular dynamics simulations[148, 168] predict a cross-section of about 1.0 nm for the HA chain, which happens to coincide with the HA disaccharide contour length b.

The result for A_{v_0} is very close to unity and hence consistent with aqueous solution being a good solvent for HA. We note, however, that the uncertainty on A_{v_0} is rather large, as further illustrated by fits in which A_{v_0} was fixed to 0 and 2 (Figure 4.5, *dotted lines*). Equation 4.5 could reproduce the experimental data reasonably well down to at least 3 mM NaCl (Figure 4.5, *thin solid line*), confirming that the treatment of ionic interactions as an effective excluded volume provides reasonable results even at rather low ionic strengths.

From the above estimates for a and b, we find $p = 13.9$ and $v_0 = A_{v_0} b^3 \approx 0.9\text{nm}^3$. The mean value of $(pbs^2)^{1/3}$ for ≥ 50mM NaCl was 36 nm (Figure 4.4**B**), leading to $s = 57$ nm. This value is in good agreement with results from independent analysis of the surface density and permeability of HA films.[44] We recall that the mean value of $s/A_F^{1/3}$ for ≥ 50mM NaCl was 49 nm (Figure 4.4**B**). Based on the estimate of $s \approx 57$ nm, we would obtain $A_F \approx 1.6$, which is again on the order of unity, as expected.

Taken together, self-consistent mean-field theory and scaling theory could reproduce the experiment well. The quality of the fits, and the extracted quantitative parameters suggest that grafted HA films can be treated as polymer brushes, in which ionic interactions are treated as an added excluded volume, over a large range of ionic strengths.

4.2.3.2 Force profiles at low salt concentrations (osmotic brush)

In the limit of low salt concentrations, we can neglect excluded volume interactions of the polymer backbone. In a first approximation, we assume a box profile, local electroneutrality and Gaussian chain elasticity. For $\alpha c \gg c_s$, Equation 4.2A simplifies to $E_{\text{ion}}(d)/kT = \alpha l_c/(bs^2)\ln(d/L)$. With Equations 4.1, 4.2C and 4.4, we obtain:

$$\frac{F}{R} = C_{\text{MFT-BP}}\left[\frac{1}{2}\left(\frac{d}{L}\right)^2 - \ln\left(\frac{d}{L}\right) - \frac{1}{2}\right] \quad \text{with} \quad C_{\text{MFT-BP}} = 6\pi\frac{L_{\text{MFT-BP}}^2 kT}{pbs^2 l_c} \text{ and} \qquad [4.9A]$$

$$L_{\text{MFT-BP}} = \left(\frac{\alpha p}{3}\right)^{1/2} l_c. \qquad [4.9B]$$

We fitted force curves at all tested ionic strengths ≤0.5 mM NaCl to Equations 4.4.9 over the range $0.5 < d/L$ (again with L determined through the force threshold F_{th}). The fits with normalized F/R and d are displayed in Figure 4.6. The model matched the experiment well at intermediate compression, but underestimated the data at low compression. The resulting values for the brush thickness were similar, though about 10% smaller, than those determined *via* F_{th} (Figure 4.4**A**). The results for pbs^2 agreed very well with those obtained with the MFT-PP model at high

salt concentrations (Figure 4.4**B**). Assuming $p = 13.9$ (as obtained with the MFT-PP model), and averaging the three available data points for pbs^2 at ≤0.5 mM NaCl, we find $s = 54$ nm, in good agreement with the results at high salt concentrations. In principle, it is also possible to calculate p from $L_{\text{MFT-BP}}$ through Equation 4.9B, but the result, 2.0, was unrealistically low. p is a measure for chain stiffness; the chains hence appear more flexible than they really are within this simple approximation.

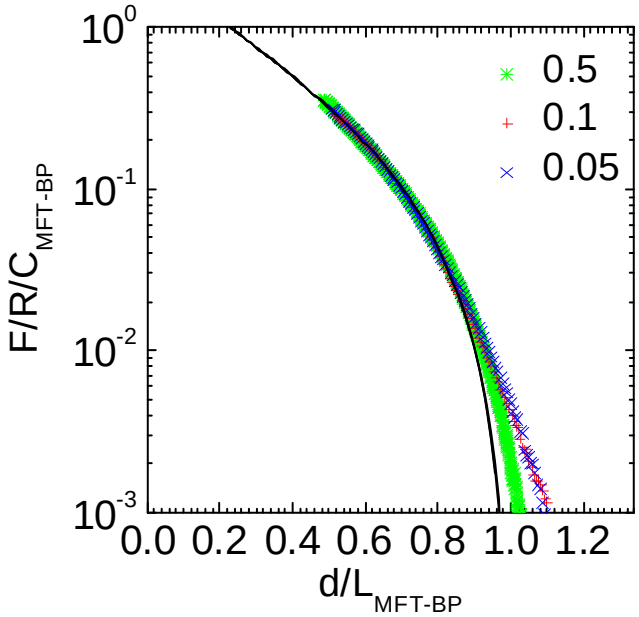

Figure 4.6**Application of theoretical models to osmotic HA brushes.** Force-distance curves at ≤0.5 mM NaCl were fitted with Equations 4.9A over the range $0.5 < d/L < 1.0$ (with L estimated through the force threshold F_{th}). Forces F/R was normalized by the prefactor $C_{\text{MFT-BP}}$, as obtained from the fitting of each individual force-distance curve. Distances d was normalized by the brush thicknesses $L_{\text{MFT-BP}}$. Symbols represent experimental data >50 pN at different NaCl concentrations, as listed; the *black solid line* represents the extrapolated fit for all datasets.

At low ionic strength, at least some of the HA chains become strongly stretched and Gaussian chain elasticity is clearly an oversimplification (Figure 4.2). Incorporation of finite chain extensibility *via* the FENE potential (Equation 4.2D) gives:

$$\frac{F}{R} = 2\pi \frac{\alpha l_c kT}{bs^2}\left\{-\frac{3}{2\alpha p}\ln\left[1-\frac{\alpha p}{\alpha p+3}\left(\frac{d}{L}\right)^2\right]+\ln\frac{L}{d}+\frac{3}{2\alpha p}\ln\frac{3}{\alpha p+3}\right\} \quad \text{with} \quad [4.10A]$$

$$L = \left(\frac{\alpha p}{\alpha p+3}\right)^{1/2} l_c. \quad [4.10B]$$

As follows from Equation 4.10B, the chains may reach the limit of the extension ($d \to l_c$) provided $\alpha p \gg 1$, that is, for strongly charged ($\alpha \approx 1$) and intrinsically rigid ($p \gg 1$) chains. In

contrast, for weakly charged and relatively flexible chains ($\alpha p \ll 3$), the well known power-law dependence (Equation 4.9B) is recovered. Equation 4.10A generates a steeper increase in the forces at low compression than Equation 4.9A. Consequently, the fit with Equation 4.10A was always worse (*not shown*). Clearly, the rather weak increase in the forces at low compression that we observe experimentally cannot be explained by finite chain extensibility.

Alternatively, the weak force increase may result from a non-constant monomer density profile. The box profile assumption can be released in the framework of self-consistent mean-field theory. Assuming again local electroneutrality and Gaussian chain elasticity, a Gaussian density profile would be expected for osmotic brushes (MFT-GP). In this case, the compression force can be derived from Equation 13 in ref. 157 and Equation 4.4:

$$\frac{F}{R} = C_{\text{MFT-GP}} \ln\left[\operatorname{erf}\left(\frac{L_{\text{MFT-GP}}}{H}\right)/\operatorname{erf}\left(\frac{d}{H}\right)\right] \text{ with } \quad C_{\text{MFT-GP}} = 2\pi\frac{\alpha l_c kT}{bs^2}, \qquad [4.11A]$$

where $\operatorname{erf}(\xi) = 2/\sqrt{\pi}\int_0^{\xi}\exp(-x^2)\,dx$ is the error function. The decay length of the Gaussian profile H (which should not be confounded with the brush thickness) is given by:

$$H = \left(\frac{8}{3\pi^2}\right)^{1/2}(\alpha p)^{1/2} l_c. \qquad [4.11B]$$

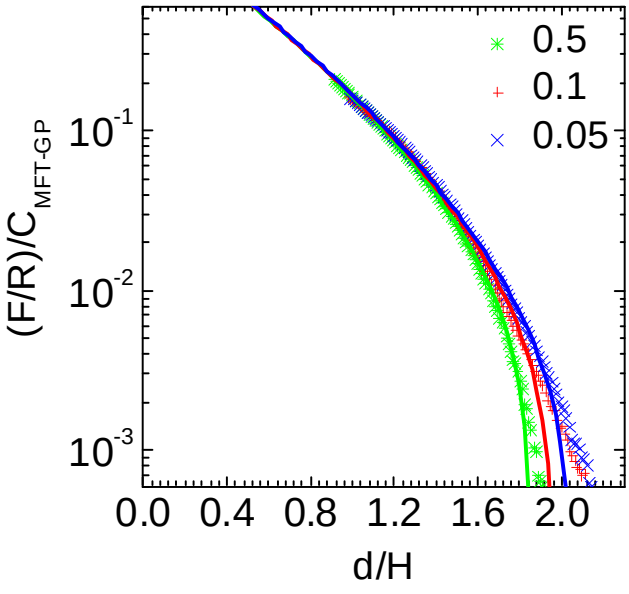

Figure 4.7**Application of Gaussian profile assumption to osmotic HA brushes.** Force-distance curves at ≤0.5 mM NaCl were fitted with Equations 4.11A over the range $0.5 < d/L < 1.0$ (with L estimated through the force threshold F_{th}). Forces F/R was normalized by the prefactor $C_{\text{MFT-GP}}$, as obtained from the fitting of each individual force-distance curve. Distances d was normalized by the decay length H. Symbols represent experimental data >50 pN at different NaCl concentrations, as listed; the *colored solid lines* are extrapolated fits to individual datasets.

In order to derive Equation 4.11A, we have assumed that a cutoff distance $L_{\text{MFT-GP}}$ exists at which $[\partial E(d)/\partial d]_{d=L} = 0$. $L_{\text{MFT-GP}}$ is hence an empirical measure for the uncompressed brush thickness. Using *s*, *L* and *H* as adjustable parameters, this approach significantly improved the fit (Figure 4.7) compared to the box-profile model (Figure 4.6), even though the theory still underestimated the forces at very weak compression. $L_{\text{MFT-GP}}$ agreed well with the brush thickness determined *via* F_{th} (Figure 4.4**A**). In contrast, *s* was approximately 2-fold larger than expected (mean 107 nm). By comparing Equation 4.9A-B with Equation 4.11A, it can easily be seen that $C_{\text{MFT-GP}} = C_{\text{MFT-BP}}$, and that an error of comparable magnitude would occur when deriving *s* through Equation 4.9A using $C_{\text{MFT-BP}} = 2\pi\,\alpha l_{\text{c}} kT/(bs^2)$. The overestimation of *s* is hence an indirect consequence of the underestimation of *p*, due to the neglect of finite chain extensibility. *H* was 2.0±0.1 fold smaller than $L_{\text{MFT-GP}}$. *H* was also 1.9-fold smaller than $L_{\text{MFT-BP}}$, that is 1.7-fold larger than what would be expected from the comparison of Equations 4.9B and 4.11B. We suspect that this discrepancy may also originate from ignoring finite chain extensibility in our model.

Taken together, the experimental data is overall consistent with the behavior expected for the osmotic brush regime. The best fit is obtained with the MFT-GP model, yet *s* remains overestimated in this case possibly because of the neglect of finite chain extensibility. A more realistic self-consistent model that accounts for finite chain extensibility is likely to lead to results that cannot be expressed by a simple analytical expression, and is outside the scope of this work. In the light of the results with Equations 4.10 and 4.11, the reasonably good quality of the fit with the MFT-BP model (Equation 4.9) appears to be coincidental, i.e. the result of a fortunate cancellation of errors due to the Gaussian chain elasticity approximation on the one hand and the box profile approximation on the other.

4.3 Discussion

Employing the combined AFM/ RICM setup, we have systematically quantified the thickness and the compressive response of HA brushes over a broad range of NaCl concentrations. With regard to polymer physics, our HA brushes are interesting as a well-defined model system for end-grafted polyelectrolyte chains. The molecular weight distribution of HA is narrow, and no bulky groups for attachment to the surface are required, such as it is the case for diblock copolymers.[169, 170] Instead, HA interacts exclusively *via* a biotin moiety at its reducing end with the surface.[44] The grafting-to approach produces surface densities that are large enough to induce chain stretching into the brush regime, even at high ionic strengths.

Our study provides evidence that grafted HA films behave very much like brushes of strong polyelectrolytes with an intrinsically stiff backbone (i.e. $p \gg 1$). Strong polyelectrolyte brushes that have so far been reported in the literature were predominantly made of a few different molecules: poly(styrene sulfonate) (PSS)[156, 171-174], poly(vinyl methyl pyridinium) (PVP),[175] and double-stranded DNA.[176, 177] When compared to these brushes, HA brushes reveal particular features:

At high salt concentrations, HA films show an attenuation in the dependence of thickness on ionic strength (Figure 4.2). The excellent fit with Equation 4.3A to the brush thickness data provides strong evidence that intrinsic inter-chain repulsion (i.e. positive excluded volume, $v_0 > 0$) is responsible for this behavior. Such a behavior is not commonly observed for water-soluble synthetic polyelectrolytes such as PSS or PVP: they typically display inter-chain attraction once charges are sufficiently screened. Several earlier reports[13, 178] had proposed HA self-association through inter-chain hydrophobic interactions and hydrogen bonds as a determinant of HA behavior, but this view has been challenged by more recent solution-based studies[19, 179] (see ref. 21 for a detailed discussion). In this regard, our study provides further and independent experimental evidence that attractive inter-chain interactions do not play an important role in the physico-chemical properties of polymeric HA assemblies.

At low ionic strength, on the other hand, HA becomes very strongly stretched: L/l_c reached values up to 0.87, which is larger than the largest values that we found in the literature: Balastre et al.[156] reported $L/l_c \leq 0.8$ for PSS brushes. Equation 4.10B can rationalize why this is. Relative chain stretching increases monotonously with $\alpha p = \alpha a/b$. The statistical segment length a of HA (14 nm) exceeds that of PSS (0.25 nm) by more than 50-fold. In addition, the fraction of charged monomers α is likely to be unity in HA, while values of PSS are about 3-fold lower, due to incomplete sulfonation and counterion condensation.[166] The latter gain is though offset by the fact that the disaccharide repeat unit in HA is about 4-fold larger than the monomers in PSS. Hence, the main reason for the stretching of HA is its intrinsic stiffness ($p \gg 1$), while the charges are distributed such that charge density is maximal yet counterion condensation is avoided. From theoretical considerations, we can expect that the grafting density affects the degree of stretching in the osmotic brush regime only weakly, although we have not tested this experimentally. Even though the intrinsic stiffness of HA is considerable, it should be pointed out that the statistical segment length a = 14 nm (or the corresponding persistence length l_p = 7 nm) remains by several orders of magnitude below the contour length. Therefore, mechanical effects of chain bending under confinement, which may dominate the force response for even stiffer chains, such as double-stranded DNA,[176, 177] remain negligible.

The overall quality of the fits to Equations 4.7, 4.8, 4.9 and 4.11 confirms that the brush compression data can be reasonably well approximated by simple scaling and mean-field models. Self-consistent mean-field theories reproduced the data best, for both salted (MFT-PP) and osmotic (MFT-GP) brushes. Since these models account for a distribution of the chain ends in the brush, it is not surprising that they captured the soft initial repulsion particularly well. For salted brushes, scaling theory (ST) reproduced the data better than the simple mean-field theory with constant density profile (MFT-BP).

We recall, however, that none of the models should be expected to reproduce the data perfectly. First, the applied theoretical approaches neglect Gaussian fluctuations of the free chain ends. Such fluctuations would be expected to lead to an onset of repulsion at larger distances. Second, for a polyelectrolyte brush, the assumption of all counterions being confined to the brush is an approximation. Residual counterions above the brush, and the cloud of counterions from the colloidal probe surface, will produce another soft repulsion at $d \geq L$.[83] Third, the polydispersity of the polyelectrolyte chains – even if it is minor in our case – is likely to have a sizeable effect on the distribution of chain ends,[180-183] and might hence also affect the forces at low compression. In the case of salted brushes, the interaction distances measured at $F_{\mathrm{th}} = 50$ pN were already about 20% smaller than the brush thicknesses determined with the self-consistent mean-field approach (Figure 4.4**A**). We therefore speculate that these subtle effects are too small to be picked up with the current force resolution of our experimental setup. It is also likely that the ST model reproduced the force profiles better than the MFT-BP model, because it has a softer profile at weak compression. For osmotic brushes, the counterion-cloud between the brush and the charged sphere, as well as the effect of polydispersity, would be longer ranged and more pronounced, due to the lack of screening by additional salt. This could explain the weaker rise in the force at low compression than predicted by our theoretical models. We note, however, that the assumption of local electroneutrality is a very good approximation for our experimental system: according to ref. 83, the LEA is valid if $H/\Lambda \gg 1$, with $\Lambda = bs^2/(2\pi l_{\mathrm{B}} \alpha l_{\mathrm{c}})$ being the Guy-Chapman length of an equivalent surface that carries all the negative charges of the HA brush; from $H = 1.2\mu\mathrm{m}$ and $s = 57\mathrm{nm}$ we find $H/\Lambda = 4700$. Moreover, the surface density of counterions outside the brush can be estimated by $Q_{\mathrm{outside}} = 3\pi L/(16\alpha^2 l_{\mathrm{B}} l_{\mathrm{c}}^2)$.[83] With $L_{\mathrm{MFT\text{-}GP}} = 2.4\mu\mathrm{m}$, we find a very small value of one charge per 4000 nm^2. This value is likely to be several orders of magnitude below the surface charge density of the colloidal probe surface, suggesting that the counterion cloud between brush and probe will be dominated by counterions from the probe. Last but not least, as the film is compressed, the local monomer density increases, and higher-order interactions would be expected to increasingly affect

the forces. Such interactions could explain why our theoretical models underestimated the forces above 50% compression systematically. Under good solvent conditions, ternary (and higher order) interactions typically contribute to a similar extent as binary interactions to the free energy, when the volume fraction of polymers inside the brush reaches a few tens of percent. In our experiments, the HA volume fraction did not exceed 1%, and the effect of higher order interactions should hence remain small.

The elastic response of pure HA brushes to compressive forces over a wide range of ionic strengths indicates that the chains can rearrange rapidly, within seconds, in the direction normal to the surface, and readily regain their original conformation if external stress is released. The longest segmental relaxation time in the system pertains to the relaxation of meshwork strands. To first approximations, the mesh size in the HA brush equals the characteristic spacing between grafting points,[79] and the meshwork strand relaxation time is $\tau_s \approx \eta s^3/(kT)$.[93] With the viscosity of water $\eta = 0.9\text{mPas}$ and $s = 57\text{nm}$, we find $\tau_s \approx 41\mu\text{s}$, i.e. segmental relaxations are indeed much faster than the experiment, consistent with the elastic response. At the same time, concomitant liquid flow in and out of the compressed area must occur with relative ease, i.e. without significant dissipative losses. The hydrodynamic forces due to liquid drainage can be estimated as $F_H \approx R^2 \eta l_c^{3/2} s^{-3} v_z d^{-1/2}$ (equation 2.13 in ref. 184). With an approach speed of $v_z = 100\,\text{nm/s}$ and smallest approach distances of $d_{\text{min}} = 0.1\mu\text{m}$ in our assays, the maximal force would be $F_H \approx 16\text{pN}$, which is indeed close to the detection limit. On the other hand, we note that the purely elastic response, and the good agreement of our data with polymer and polyelectrolyte brush models, suggest that lateral displacement of HA out of the compression zone is negligible in our case. This finding is not self-evident, given that the HA brushes were formed on fluid supported lipid bilayers, and that lateral displacement had previously been reported for films of HA molecules that were either physisorbed to surfaces[122] or covalently bound to SLBs *via* multiple attachment points along the chain.[121] A likely explanation is that the streptavidin molecules that anchor HA to the SLB are forming two-dimensional crystalline domains[127] thereby rendering HA laterally immobile. In addition, the approach speed in our study was rather high, compared to previous studies with the surface force apparatus.[121, 122] Future studies that systematically vary the grafting density, the molecular weight and the lateral mobility of HA, and the approach speed should allow to further refine our understanding of the behavior of HA assemblies and the dynamics of re-organization of HA films under mechanical stimuli.

4.4 Conclusions

Pure HA films showed a pronounced salt-dependence in the uncompressed thickness that is characteristic of strong polyelectrolyte brushes. The brush thickness could be modeled quantitatively, if finite chain stretching, intrinsic chain stiffness ($p \gg 1$) and intrinsic excluded volume ($v_0 > 0$) interactions were taken into account. Simple theoretical polyelectrolyte brush models could reproduce the response upon brush compression well. From the biological perspective, the generated data represent a valuable reference for future quantitative studies of more complex HA-rich films, such as pericellular coats. The level of control in their preparation should also make HA brushes a useful experimental model system to further test and refine the theories of brushes of strongly charged and intrinsically stiff polyelectrolytes.

5. Conclusions and perspectives

The primary aim of this work was the investigation of mechanical properties of hyaluronan brushes. To enable a detailed quantitative analysis, a novel setup of combined colloidal probe AFM/RICM was established. Comparison of experimental data with polymer physics theories left us with a thorough understanding of the physico-chemical properties of films of end-grafted HA and polyelectrolyte brushes in general. The surface-sensitive characterization techniques QCM-D and spectroscopic ellipsometry provided complementary information about film buildup and biomolecular binding kinetics.

An experimental setup that combines colloidal probe AFM and dual-wavelength RICM into one instrument has been developed. The combination provides compression forces as function of absolute probe-sample separation distance. With the novel "*R-adjustment*" method, the absolute distance can be quantified from the RICM data even without exact prior knowledge of the probe diameter and with imperfect focusing. The combination enables correction of linear instrumental drifts and can provide the cantilever sensitivity without an extra reference measurement.

At physiological ionic strength and pH, pure HA films showed an elastic compressive response in good quantitative agreement with theoretical predictions for polymer brushes. The HA brushes were further used to study the formation of extended HA-aggrecan matrices that are of importance in cartilage. The results confirm that several micrometer thick and very soft and hydrated films can be reconstituted through self-organization of aggrecan and surface-confined HA. The drastic aggrecan-induced increase in HA brush thickness and the ensuing compressive response suggest the formation of hierarchical brushes.

The salt dependence of the thickness and compressive response of end-grafted HA film was systematically studied. Comparing theory and experiment demonstrated that grafted HA films behave like strong polyelectrolyte brushes. An excellent quantitative agreement between theoretical predictions and experimental data was obtained when explicitly considering finite chain stretching, intrinsic chain stiffness and intrinsic excluded volume repulsion. This means that these parameters are important determinants of the polyelectrolyte behavior of HA brushes, and suggests that attractive inter-chain interactions do not play an important role in the physico-chemical properties of polymeric HA assemblies.

The combined colloidal probe AFM/RICM instrument developed in this thesis represents a novel tool for the quantitative analysis of the mechanical properties of surface-confined, soft and solvated films. Such an analysis is desired to test functional performance, but it can also provide valuable information about the internal organization and dynamics of the films. In terms of future technical development, developing a software program for online analysis of interferographs from the combined setup would be desirable. With such a tool, one could get information about the distance between the probe and the surface in real time, and feed the information back into the AFM to better control the applied forces and distances during a measurement. The combined colloidal probe AFM/RICM can be used to study the tribological properties of end-grafted polymer brushes by measuring the lateral deflection of AFM cantilever. Friction force can be measured by displacing the upper surface (where the cantilever is movement is connected to a piezo system) horizontally using piezo driven motors and by functionalizing the colloidal probe and underlying surface with identical polymers and immobile anchor points.

The research may be continued with systematic experiments by studying the impact of divalent ions like Ca^{2+} on the conformation of HA films. A plateau in thickness is predicted at high salt concentrations for monovalent ions due to excluded volume repulsion. It would be interesting to see if divalent ions have the same effect. Also a comparative investigation of brush thickness and mechanics as a function of salt concentration, with both monovalent and divalent ions, would help to better understand the effect of charge shielding on the conformation and physico-chemical properties of HA. Investigating the influence of pH on the conformational behavior of end-grafted HA would also be worthwhile. In particular, HA is expected to become a weak polyelectrolyte (where the polyelectrolyte charge density depends sensitively on the environment) at low pH, and a distinctly different response to variations in ionic strength would in this case be expected. Comparison with theory might provide additional insight into the behavior of films of grafted polyelectrolytes.

The supported lipid bilayer-based HA-aggrecan composite film developed in this thesis represents an interesting *in vitro* model system to get mechanistic insight into the mechanics of cartilage. For example, resistance of HA brushes to external mechanical stimuli can be studied at different concentrations of aggrecan in the HA films. Link protein is known to stabilize the HA-aggrecan interaction and is essential for cartilage. Future studies should therefore seek to study the buildup and mechanical response (i.e. the compressive response and tribological properties) of HA-aggrecan composite films in the presence of link protein. In particular, a systematic study on the influence of the approach rate on the compressive response of HA films would enhance our

understanding of the reorganization of HA films under mechanical stimuli, and provide insight into the hydrodynamics of HA assemblies that are likely to be important for cartilage function.

6. Materials and methods

6.1 Preparation of solutions, lipid vescicles, streptavidin, hyaluronan, and aggrecan

A 'HEPES' buffer solution of 150 mM NaCl, 10 mM HEPES, and 3 mM NaN_3 was prepared in ultrapure water (resistivity 18.2 MΩ/cm). The pH was adjusted to 7.4 using NaOH. An amount of 2 mM $CaCl_2$ was added for the formation of SLBs. NaCl solutions in ultra pure water at desired molar concentrations (500 to 0.01 mM) were also prepared.

Lyophilized dioleoylphosphatidylcholine (DOPC) and dioleoylphosphatidylethanolamine-CAP-biotin (DOPE-CAP-biotin) (Avanti Polar Lipids, Alabaster, AL, USA) were dissolved in chloroform, mixed in a molar ratio of 9:1, dried, re-suspended in HEPES buffer solution and homogenized, as described earlier.[70] Small unilamellar vesicles (SUVs) of 2 mg/mL concentration were obtained by sonication, as described earlier[185] and stored at 4°C.

Lyophilized hyaluronan (HA), biotinylated at its reducing end and with well-defined molecular weights of 1.08 ± 0.06 and 0.84 ± 0.04 MDa was purchased from Hyalose (Select-HA B1000; Oklahoma City, OK, USA). HA was dissolved in ultra pure water at a concentration of 1 mg/mL, and gently shaken for 2 hours. The stock solution was aliquoted, and stored at -20°C. Lyophilized streptavidin and aggrecan (both Sigma) were dissolved in ultra pure water and buffer solution (10 mM HEPES, pH 7.4, 150 mM NaCl, 3 mM NaN_3) at concentrations of 1 and 2 mg/mL respectively, aliquoted and stored at -20°C.

6.2 Substrate preparation

Silica coated QCM-D sensors were used as substrates in QCM-D experiments. QCM-D sensors with silica coating (QSX303, Biolin Scientific, Västra Frölunda, Sweden) were cleaned by immersion in a 2% sodium dodecyl sulfate solution for 30 min, thorough rinsing with ultrapure water followed by blow-drying with nitrogen gas. Cleaned substrates were exposed to UV/ozone (UV/Ozone ProCleaner; Bioforce Nanoscience, Ames, IA, USA) for 30 min prior to use.

For ellipsometry experiments, silicon wafers were used as substrates. A silicon wafer with a native oxide layer of about 2 nm thickness (University Wafers, South Boston, MA, USA), was cut to pieces of desired size (3×1 cm) to fit into the custom-made ellipsometry cuvette. The wafer

pieces were rinsed in ultrapure water, blow-dried with nitrogen gas and treated with UV/ozone for 30 min prior to use.

Glass cover slips were used as substrates for combined colloidal probe AFM/RICM measurements. Glass cover slips (#1.5, 24 × 24 mm^2; Menzel-Gläser, Thermo Scientific, Germany) were cleaned by rubbing with a lint-free tissue paper and immersion in freshly prepared piranha solution (3:1 (*v*/*v*) mixture of concentrated H_2SO_4 and 50% H_2O_2) for 1 h, rinsed thoroughly with ultra pure water and gently blow-dried with a stream of N_2 gas. Substrates were stored in sealed petri dishes. Prior to use, the glass cover slips were treated with UV/ozone for 30 min.

6.3 Atomic force microscopy

6.3.1 Spring constant calibration using thermal noise method

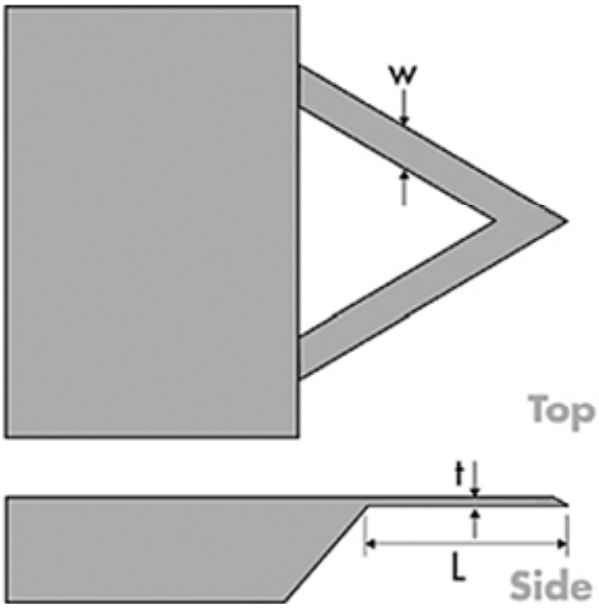

Figure 6.1 Scheme of a chip with a triangular tipless cantilever. Length L = 180-196 μm, width W = 18-28 μm, thickness t = 0.4-0.7 μm (adapted from www.brukerafmprobes.com).

To convert the deflection to force it is necessary to know the spring constant of the cantilever. There are several methods for calibrating the spring constants of cantilevers with calibration uncertainities of 10-20%, when compared between different methods.[186] We make use of the spring constant calibration method that is integrated into the Nanowizard AFM software (JPK) and which is based on the analysis of the thermal noise spectrum of the cantilever.

Modeling the cantilever as a simple harmonic oscillator, Hutter and Bechhoefer applied the equipartition theorem to relate the Brownian motion of the cantilever (assuming that motions around the cantilever's fundamental resonance frequency dominate) to thermal energy.[187] A

measurement of the thermal noise $\langle x^2 \rangle$ in the cantilever deflection allows the spring constant to be determined through $k = k_B T / \langle x^2 \rangle$, where k_B is Boltzmann's constant and T is the absolute temperature (in Kelvin). The value $\langle x^2 \rangle$ can be obtained by performing a power spectral density analysis of the thermally driven cantilever deflection and integrating the area under the resonance peak.

The software module measures the magnitude of frequency-dependent free fluctuations of the cantilever at room temperature. A Lorentzian curve is fitted to the peak that is observed at the cantilevers resonance frequency. The area under the curve corresponds to $\langle x^2 \rangle$ (Figure 6.2).

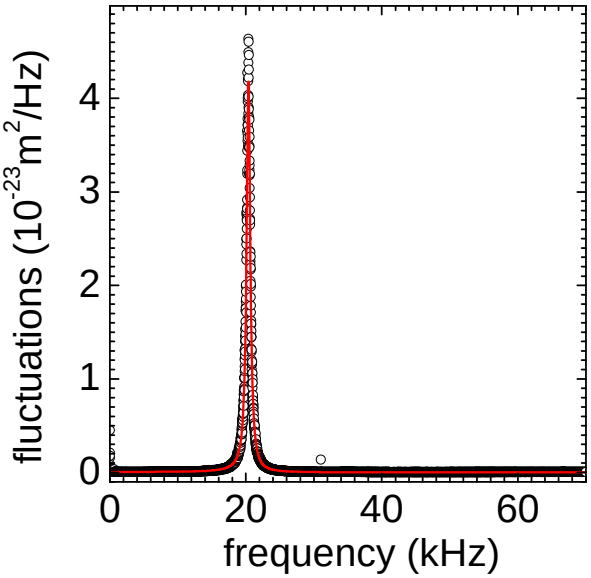

Figure 6.2 Calibration of the cantilever spring constant using thermal noise method. The plot shows the resonance peak that is observed at the cantilever's resonance frequency in air (*symbols*) and the Lorentz fit (*red solid line*). The fit in this example gave a spring constant of 0.1 N/m.

We used tipless V-shaped Si_3N_4 cantilevers with a nominal spring constant of 0.06 Nm^{-1} (Veeco Probes, CA, USA). The real cantilever spring constant, determined before attaching the microsphere using the thermal noise method,[187] was k = 0.1 Nm^{-1}.

6.3.2 Preparation of AFM colloidal probes

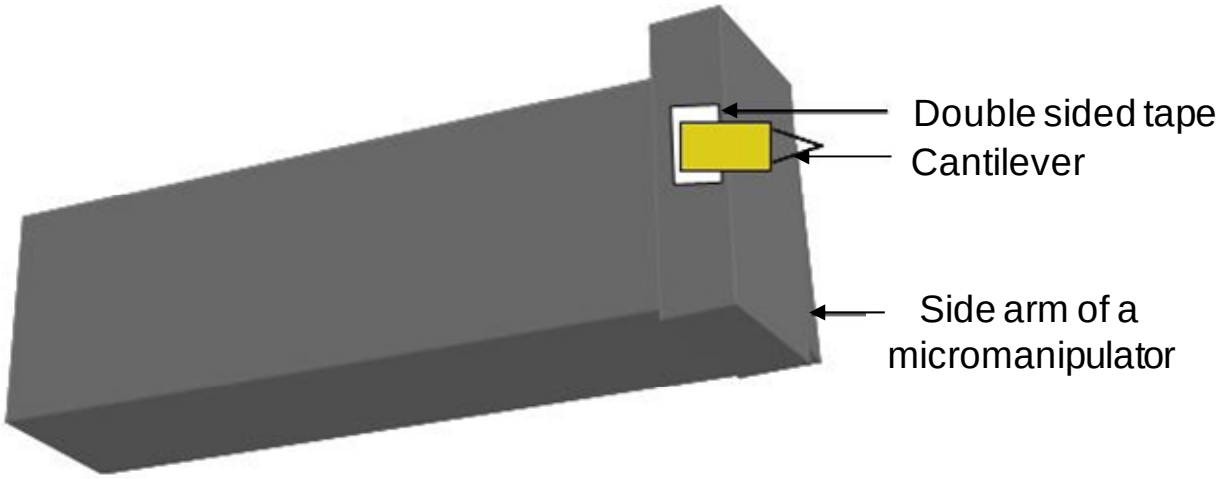

Figure 6.3 Cartoon showing the custom-designed side arm of the micromanipulator. A piece of double-sided sticky tape is used to attach the cantilever chip to the arm.

Polystyrene microspheres (Polysciences, Eppelheim, Germany) of 25±3 µm diameter (size provided by the manufacturer) were attached to tipless V-shaped Si_3N_4 cantilevers, using a black two-component epoxy glue (EPO-TEK 320, Polytec GmbH, Waldbronn, Germany). The microspheres were washed in ethanol and in ultra pure water, and stored in ultra pure water at 4°C. Before use, they were transferred into ethanol, 5 µl of the solution were spread on a cleaned glass cover slip, and the ethanol was left to evaporate. A small droplet of about 1 µl epoxy glue mixture was deposited on the same glass slide. The glass cover slip was mounted on an inverted microscope with 20× objective. A micromanipulation setup was used to wet the end of a given AFM cantilever with glue, and to attach a single microsphere to its apex. We found the gluing procedure to give the best results if the epoxy mixture was left to viscosify for about 1 h before use. Care was taken to wet a sufficient part of the lower cantilever face with the black glue (to avoid undesired reflections from the bottom of the cantilever during RICM imaging), but not to coat the upper Au-coated face (which is crucial for the laser-based detection of the cantilever bending in the AFM). Prior to use, the cantilevers with colloidal probe were treated with UV/ozone for not more than 5 min.

6.4 Combined colloidal probe AFM and RICM setup

6.4.1 Instrumental setup

We used a NanoWizard II with TAO module (JPK, Berlin, Germany), installed on an inverted optical microscope (Axio Observer D1; Zeiss, Oberkochen, Germany) to combine colloidal probe AFM and RICM (Figure 6.4). The NanoWizard II was equipped with an *x* and *y* sample scanner

(TAO module; JPK), which enables force measurements at various spots on a given sample while maintaining the colloidal probe aligned along the optical axis of the microscope. AFM force curves were acquired in closed-loop mode at an approach speed of v_{piezo} = 100 nm/s, and with a maximal load on the order of typically 10 nN. The microscope is equipped with a mercury lamp (X-Cite 120; Lumen Dynamics Group, Ontario, Canada) as light source in epi-illumination reflection mode. Stray light was filtered by the antiflex technique,[188] using a filter cube with crossed polarizers (AHF Analysentechnik, Tübingen, Germany) and an antiflex oil-immersion objective (EC Plan Neofluar Antiflex, 63×/1.25; Zeiss).[64, 123]

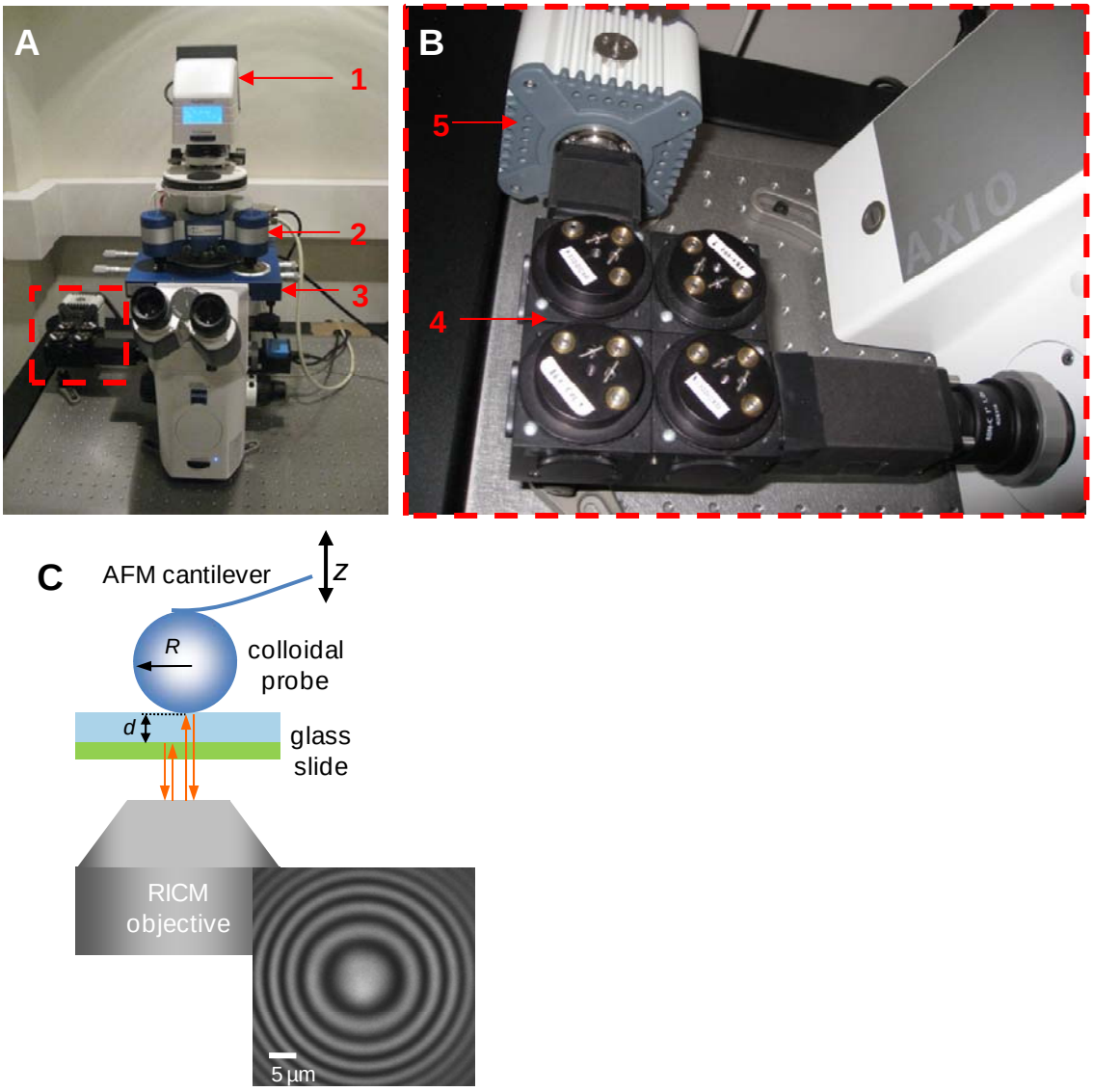

Figure 6.4 (**A**) Photograph of the combined AFM/RICM setup. The AFM (2) is positioned on an inverted optical microscope (1) equipped with *x* and *y* sample scanner (TAO module; 3). The combined setup enables optical imaging in parallel with AFM measurements. (**B**) For dual-wavelength RICM, images at two selected wavelengths are extracted from the reflected white light through the custom-made beam splitter and filter unit (4) and recorded by two halves of the CCD camera (5) chip. (**C**) Schematic representation of the combined colloidal probe AFM/RICM setup.

The colloidal probe was aligned to the optical axis with the aid of the bright field transmission optics of the optical microscope, and approached to the sample surface by the AFM stepper motors, until the characteristic Newtonian fringe pattern (Figure 6.4**C**) started to appear in RICM imaging mode. The emergence of the fringe pattern indicated that the probe was within a distance of a few µm from the sample. To optimize the quality of the RICM image, the opening of the field diaphragm was adjusted. The opening of the aperture diaphragm was kept minimal and constant throughout all measurements. Interferographs at 438 and 543 nm were acquired simultaneously by two halves of the same chip (1344×1024 pixels) of a CCD camera (ORCA-ER, Hamamatsu Photonics, Massy, France). To this end, the beam of reflected light exiting the microscope was guided through a custom-built beam splitter and filter unit. The unit contained (i) a chromatic beam splitter to separate light above and below 505 nm (Q505LP; AHF Analysentechnik), (ii) two band-pass filters of around 20 nm width, centered at wavelengths of $\lambda = 438$ and 543 nm, respectively (BrightLine HC 438/24 and BrightLine HC 543/22; AHF Analysentechnik), and (iii) two mirrors, focusing lenses and a laser beam splitter (600DCR; AHF Analysentechnik) to guide the two filtered beams onto the camera chip at a resolution of typically 50 nm per pixel. Images were acquired at a frame rate of 8 s^{-1} using the software SimplePCI (Hamamatsu) and an exposure time of 100 ms. A set of about 100 interferographs were acquired per AFM force curve.

6.4.2 Liquid chamber for combined AFM/RICM measurements

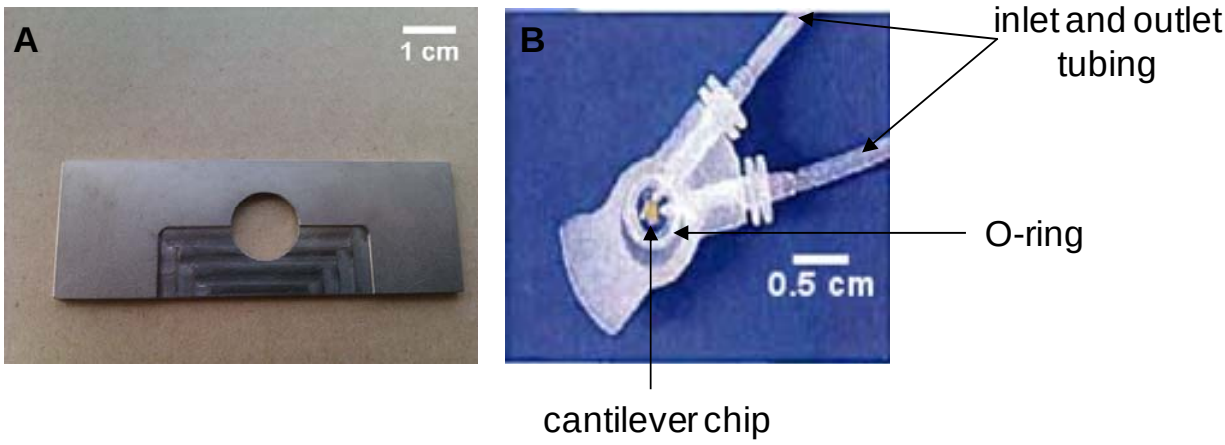

Figure 6.5 (**A**) Custom-made titanium sample holder for combined colloidal probe AFM/RICM measurements. (**B**) JPK's SmallVolumeCell with O-ring and a mounted cantilever chip. Liquid exchange occurred through inlet and outlet tubing connected to a peristaltic pump.

A cleaned glass cover slip was first attached to a custom-made titanium sample holder (Figure 6.5**A**) using two-component glue (Twinsil; Picodent, Wipperfurth, Germany), and covered with a droplet of 250 µL aqueous solution. The desired biomolecular film was prepared on the substrate,

and the sample was installed on the AFM sample stage. The sample holder was designed to accommodate both a liquid cell (SmallVolumeCell; JPK, shown in Figure 6.5**B**) on the top and a light microscope objective on the bottom. A chip with a colloidal probe cantilever was glued to the liquid cell using Twinsil glue. For measurements with liquid exchange, the liquid cell was equipped with silicone tubings, and with a silicone rubber ring (closed liquid cell). The sample holder, the liquid cell, the tubings, and the silicone rubber ring were cleaned by sonication, first in ethanol and then in ultra pure water, for 30 min respectively. The accessories were rinsed thoroughly with ultra pure water after each sonication step, and eventually blow-dried with a stream of N_2 gas. The liquid cell was mounted on the AFM head, and the tubings and the liquid cell were filled with aqueous solution using a pair of syringes, until a hanging droplet was formed in the liquid cell. The AFM head was then mounted on the AFM sample stage, and lowered towards the sample using stepper motors until the silicon rubber ring made a good seal with the glass substrate. Care was taken to avoid bubbles and to keep the sample wet at all times. For further exchange of liquids, the inlet port of the liquid cell was connected to a peristaltic pump (Ismatec, Glattbrugg, Switzerland). Applied flow rates were typically 0.5 ml/min. For measurements without liquid exchange, the liquid cell was used without tubings and rubber ring (open liquid cell), and liquid was filled into the inlet and outlet ports of the liquid cell with the aid of a pipette.

6.4.3 Preparation of HA films on glass slide for combined AFM/RICM measurements

Films of grafted HA were prepared within a 250 µL droplet of buffer solution (10 mM HEPES, pH 7.4, 150 mM NaCl, 3 mM NaN_3) on the glass cover slip, adapting a previously described method.[44] First, SUVs were added at a final concentration of 100 µg/mL together with 2 mM $CaCl_2$, and incubated for 30 min. Second, streptavidin was incubated at 20 µg/mL for 30 min. Third, biotinylated HA was incubated at 20 µg/mL for 8 h. To remove excess sample after each incubation step, the droplet content was diluted by repeated addition of a twofold excess of buffer and removal of excess liquid until the concentration of the solubilized sample, estimated from the extent of dilution, was below 10 ng/mL. Repeated aspiration and release of the droplet content by a micropipette ensured homogenization of the cuvette content at each dilution step. Care was taken to keep the substrate wet at all times.

6.5 Quartz crystal microbalance with dissipation monitoring (QCM-D)

The QCM-D technique is based on the change in the resonant frequency of an AT cut quartz crystal sensor disc sandwiched between two electrodes typically made of gold, upon interaction of

soft matter with the surface of the sensor crystal. To a first approximation, changes in the sensor's resonance frequency, Δf, relate to adsorbed masses (including hydrodynamically coupled solvent) and changes in the dissipation, ΔD, relate to frictional losses, for example, due to the soft, viscoelastic properties of an adsorbed film. For sufficiently rigid films, the relationship between Δf and the areal mass density (or mass per unit area), Δm, at the sensor surface is well approximated by:

$$\Delta m = -C\frac{\Delta f_n}{n}. \qquad [6.1]$$

This equation is the so-called Sauerbrey equation,[189] and establishes a linear relationship between Δf and Δm. n is the overtone number and

$$C = \frac{v_q \rho_q}{2f_0^2}, \qquad [6.2]$$

is the mass-sensitivity constant, with v_q, and ρ_q being the wave velocity (speed of sound) in quartz and the density of quartz, respectively. For the sensors with a fundamental resonance frequency of 4.95 ± 0.02 MHz used here, C = 18.06 ± 0.15 ng/cm^2/Hz.[190] Frictional losses lead to an underestimation of the areal mass density by the Sauerbrey equation as the softness and/or the thickness of the film increase.

The dissipation is the inverse of the quality factor Q and defined as:

$$D = \frac{1}{Q} = \frac{E_D}{2\pi E_S} \qquad [6.3]$$

where E_s is the energy stored and E_D the energy being dissipated per oscillation cycle. As can be appreciated from equation 6.3, the dissipation is a unitless number.

QCM-D measurements were conducted with a Q-Sense E4 system (Biolin Scientific, Västra Frölunda, Sweden) using flow modules. The system was operated in flow mode with a rate of typically 5-20 µl/min, using a syringe pump (KD Scientific, Holliston, MA, USA). The working temperature was 23^{o}C. The Δf and ΔD values were collected at six overtones (n = 3, 5, 7, 9, 11, 13) corresponding to resonance frequencies of ~15, 25, 35, 45, 55, 65 MHz. Changes in dissipation D_n and normalized frequency, $\Delta f_n/n$ at selected overtones are presented.

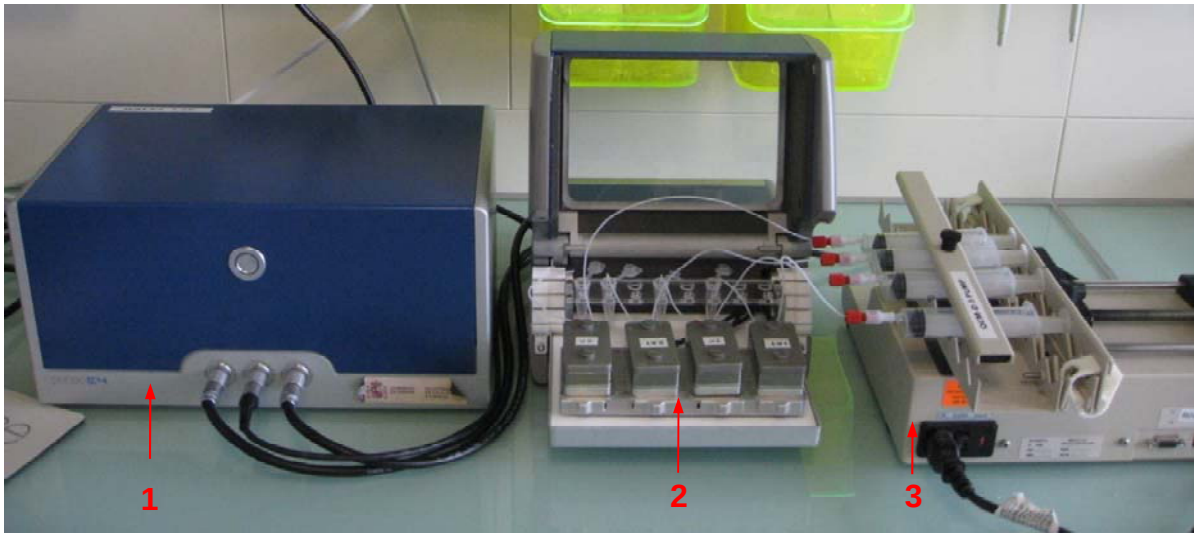

Figure 6.6 Photograph of the Q-Sense E4 QCM-D setup. 1. Electronics unit, 2. measurement unit with flow modules and sample holder, 3. syringe pump with tubings connected to the flow modules.

6.6 Spectroscopic ellipsometry

Ellipsometry is a non-destructive optical technique that measures changes in the ellipsometric angles, Delta (Δ) and Psi (Ψ), of polarized light upon reflection from a planar sample surface. We employed ellipsometry *in situ*, using silicon wafers as substrates that were installed in a custom-designed open glass cuvette. Data were acquired with a spectroscopic rotating compensator ellipsometer (M2000V, J.A. Woollam NE, USA) operating in a wavelength range of $\lambda = 380 - 1000$ nm, at 70^{o} angle of incidence and with a time resolution of ~5 s at ambient temperature.

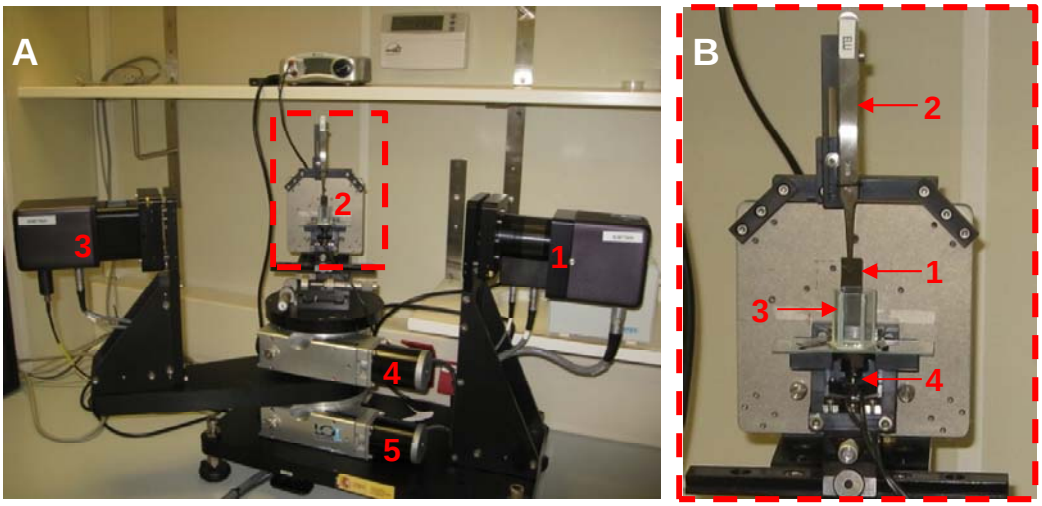

Figure 6.7 (**A**) Photograph of the ellipsometry setup used in the current experimental work. 1. Light source, 2. sample holder with fluid cell, 3. detector, 4 and 5. goniometers for sample stage and detector stage, respectively. (**B**) Magnified view of the sample stage with the substrate, a piece of silica wafer (1) held by a tweezer (2) and placed inside the glass cuvette (3). The motor driving the rotating stirrer is also visible below the glass cuvette (4).

6.6.1 Open fluid cell for ellipsometry

The custom-built cuvette was first passivated by immersion in an aquesous solution of 10 mg/mL bovine serum albumin for 20 min, rinsed with milli-Q water and blow-dried with a stream of N_2 gas. The cuvette was filled with ~700 µL buffer and care was taken to maintain the volume constant during the entire experiment (to adjust for liquid losses through evaporation, which were significant during long measurements, water was added periodically). Samples and buffer were injected using a micropipette, and excess liquid was sucked out using a syringe needle connected to a peristaltic pump (Ismatec, Glattbrugg, Switzerland). To ensure homogenization of the cuvette content, the cuvette was equipped with a magnetic stirrer at the bottom which was kept running during the injection of samples and for an additional 10 s after injection. Adsorption processes were monitored in still solution in order to match the experimental conditions that were used to create HA films for combined colloidal probe AFM/RICM experiments. To remove excess of samples, the cuvette content was diluted by repeated addition of 2-fold excess of buffer and removal of excess liquid until the concentration of the soluble sample, as estimated from the number of dilution steps, was below 10 ng/mL. The stirrer was kept running during the rinsing process.

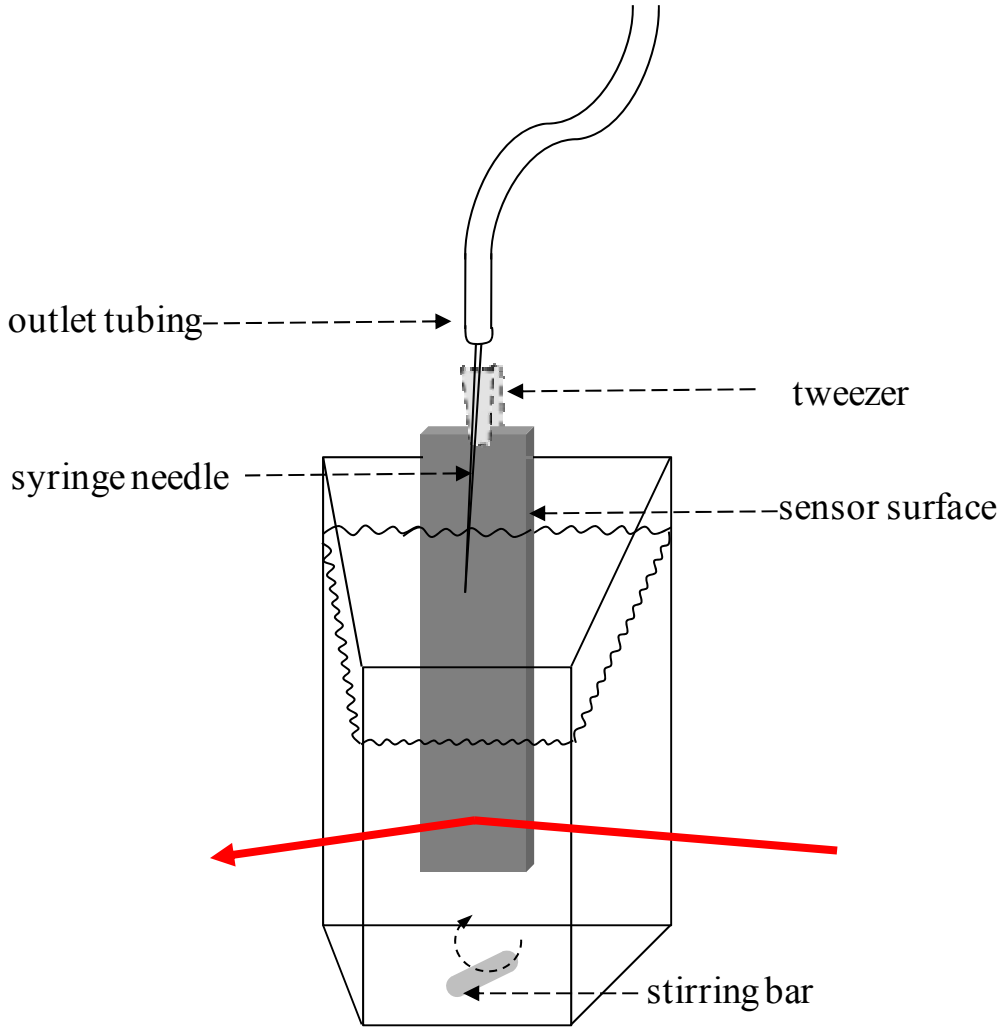

Figure 6.8 **Cartoon of the open fluid cell for in situ ellipsometric studies.** The magnetic stirrer at the bottom was driven by an external motor and ensures rapid mixing after injection of solutions. The side walls of the cuvette are made from BK7 glass. The light enters and leaves the cuvette through the side walls at perpendicular incidence. The sensor surface is held by tweezers and immersed in the solution. A syringe needle connected to a peristaltic pump is used for sucking out the excess liquid (outlet).

6.6.2 Modelling of the ellipsometry data

The software CompleteEASE (Wollam, NE, USA) was used to extract the film properties from the measured ellipsometric parameters Psi (Ψ) and Delta (Δ) across a spectrum of wavelengths (390 to 1000 nm) using a model of multiple laterally homogenous layers. Silicon was used as the substrate followed by a silicon oxide layer. First we determined the thickness L_{SiO_2} and the optical properties of the silicon oxide layer immersed in buffer solution. The native silicon oxide layer was treated as a transparent Cauchy medium, with a refractive index $n_{SiO_2}(\lambda) = A_{SiO_2} + B_{SiO_2}/(\lambda/\mu m)^2$. The semi-infinite bulk solution was also treated as a transparent Cauchy medium, with $n_{buffer}(\lambda) = A_{buffer} + B_{buffer}/(\lambda/\mu m)^2$ with $A_{buffer} = 1.325$

and $B_{\mathrm{buffer}} = 0.00322$.[191, 192] Tabulated constants for silicon were used. The fit resulted in $L_{\mathrm{SiO_2}} = 1.99$ nm, $A_{\mathrm{SiO_2}} = 1.505$ and $B_{\mathrm{SiO_2}} = 0.01315$, close to the values reported in previous studies.[185]

A first biomolecular layer that consisted either of lipids alone (ultimately forming a supported lipid bilayer) or additional of streptavidin, was treated as a homogeneous and transparent Cauchy medium with $n_{\mathrm{SLB/SAv}} = A_{\mathrm{SLB/SAv}} + B_{\mathrm{SLB/SAv}}/(\lambda/\mu\mathrm{m})^2$. $B_{\mathrm{SLB/SAv}}$ was fixed to 0.00322, i.e. the value for the surrounding buffer, and the parameters for all other layers were fixed to the values previously determined. The layer thickness $L_{\mathrm{SLB/SAv}}$ and $A_{\mathrm{SLB/SAv}}$ were fitted simultaneously. The quality of the fit was assessed by monitoring the mean square error (MSE).

The film thickness and refractive index were then used to determine the areal mass density using de Feijter's equation:[74]

$$\Gamma_{\mathrm{SLB/SAv}} = \frac{L_{\mathrm{SLB/SAv}}(n_{\mathrm{SLB/SAv}} - n_{\mathrm{buffer}})}{\mathrm{d}n/\mathrm{d}c}. \qquad [6.4]$$

Because $B_{\mathrm{SLB/SAv}} = B_{\mathrm{buffer}}$, this equation simplifies to:

$$\Gamma_{\mathrm{SLB/SAv}} = \frac{L_{\mathrm{SLB/SAv}}(A_{\mathrm{SLB/SAv}} - A_{\mathrm{buffer}})}{\mathrm{d}n/\mathrm{d}c} \qquad [6.5]$$

The dn/dc value represents the increment in the refractive index of the biomolecular film as a function of its concentration c. Values of 0.169 cm^3/g for lipids and 0.18 cm^3/g for SAv were used.[185]

The HA film was also treated as a transparent Cauchy medium. The HA film has a thickness that is comparable to or even larger than the wavelength of the probing light. For such layers, it is useful to explicitly consider heterogeneities in the direction of the surface normal, i.e. the density profile. We know (see Chapter 4) that pure HA brushes exhibit an approximately parabolic density profile at physiological ionic strength, i.e.

$$c_{\mathrm{HA}}(z) = c_{\mathrm{HA},0} L_{\mathrm{HA}}^2 \left[1 - \left(\frac{z}{L_{\mathrm{HA}}}\right)^2\right] \qquad \text{for } z \le L_{\mathrm{HA}} \qquad [6.6]$$

where z is the distance from the anchor points of the HA chains in the direction perpendicular to the surface, and $c_{\mathrm{HA},0}$ is the HA concentration close to the anchor points. To a good approximation, $\Delta n = n_{\mathrm{HA}} - n_{\mathrm{buffer}} = \mathrm{d}n/\mathrm{d}c \times c_{\mathrm{HA}}$, which gives:

$$\Delta n(z) = \Delta n_{\mathrm{HA},0} L_{\mathrm{HA}}^2 \left[1 - \left(\frac{z}{L_{\mathrm{HA}}}\right)^2\right] \qquad \text{for } z \le L_{\mathrm{HA}} \qquad [6.7]$$

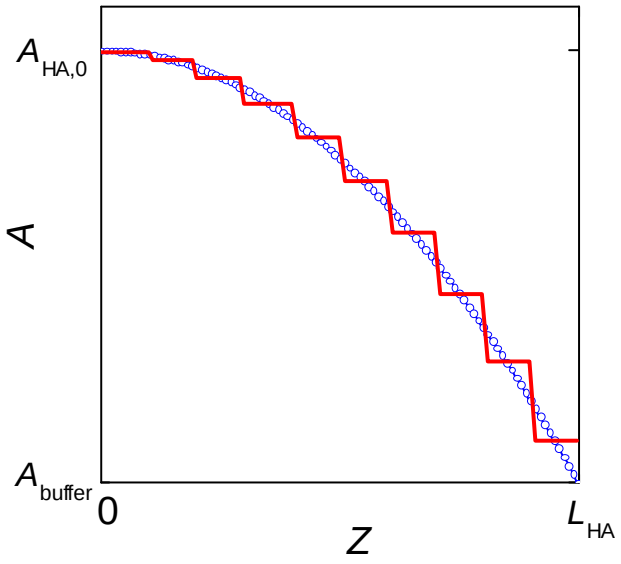

Figure 6.9 Non-linearly graded refractive index profile. The layer is divided into 10 slices of equal thickness. Each slice has a constant refractive index (red line), and the sequence of refractive indices approximates a parabola (blue circles).

To approximate the parabolic refractive index profile, the HA film was treated as a non-linearly graded layer as described in Figure 6.9, with $n_{\mathrm{HA},0} = A_{\mathrm{HA},0} + B_{\mathrm{HA},0}/(\lambda/\mu\mathrm{m})^2$ and $B_{\mathrm{HA},0} = B_{\mathrm{buffer}} = 0.00322$. Throughout the buildup of the HA film, $A_{\mathrm{HA},0}$ and the layer thickness L_{HA} were fitted simultaneously. We found that the thickness $L_{\mathrm{SLB/SAv}}$ exhibited minor drifts and that the results for L_{HA} and $A_{\mathrm{HA},0}$ depended quite sensitively on the choice of this parameter. Therefore, $L_{\mathrm{SLB/SAv}}$ was also kept as a fit parameter. All other parameters were again fixed to the values previously determined.

To obtain areal mass densities from the optical properties of a graded layer, de Fejter's equation needs to be generalized:

$$\Gamma = \frac{L_{\mathrm{HA}}}{\mathrm{d}n/\mathrm{d}c} \int_0^{L_{\mathrm{HA}}} \Delta n(z) dz. \qquad [6.8]$$

For a parabolic profile, and because the refractive index dispersion in the HA film and in the ambient medium is the same, we find:

$$\Gamma = \frac{2}{3}\left(A_{\mathrm{HA},0} - A_{\mathrm{buffer}}\right) \frac{L_{\mathrm{HA}}}{\mathrm{d}n/\mathrm{d}c}. \qquad [6.9]$$

For HA, we used dn/dc = 0.15 cm^3/g.[193]

The HA film containing aggrecan was also treated as a non-linearly graded layer. Consistent with the treatment of pure HA films, we assumed a parabolic density profile, even though we do not know the exact density profile of this composite film. Aggrecan was exposed to the HA brush at a

final concentration of 500 μg/mL. For comparison, the concentration of HA in the strongly hydrated HA brushes is about 1 mg/mL (see Chapter 2), i.e. of similar order of magnitude. This implies that the increase in the bulk refractive index due to the addition of aggrecan is comparable to the refractive index difference between the HA film and the bulk solution. Therefore, the refractive index of the ambient medium needs to be adjusted in the model. Aggrecan consists of a peptide chain with a molecular mass of ~250 kDa and many glycosaminoglycan (GAG) chains which total a molecular mass of approximately ~2.5 MDa.[194] With De Feijter's equation, we can estimate the refractive index change as $\Delta n_{\mathrm{aggrecan}} = \left[(\mathrm{d}n/\mathrm{d}c)_{\mathrm{peptide}} \times c_{\mathrm{peptide}} + (\mathrm{d}n/\mathrm{d}c)_{\mathrm{GAG}} \times c_{\mathrm{GAG}}\right]$ where, c_{peptide} and c_{GAG} are the peptide and GAG concentration, respectively, $(\mathrm{d}n/\mathrm{d}c)_{\mathrm{peptide}} = 0.18\,\mathrm{cm}^3/\mathrm{g}$ and $(\mathrm{d}n/\mathrm{d}c)_{\mathrm{GAG}} = 0.15\,\mathrm{cm}^3/\mathrm{g}$. Because the GAG chains dominate, we can simplify to:

$$\Delta n_{\mathrm{aggrecan}} \approx (\mathrm{d}n/\mathrm{d}c)_{\mathrm{GAG}} \times c_{\mathrm{aggrecan}}. \qquad [6.10]$$

For c = 500 μg/mL, this gives $\Delta n_{\mathrm{aggrecan}} = 0.000075$. Whenever aggrecan was present in the ambient solution, $A_{\mathrm{ambient}} = A_{\mathrm{buffer}} + \Delta n_{\mathrm{aggrecan}} = 1.325075$ was therefore used when fitting the data instead of A_{buffer}.

7. References

1. Evanko, S. P., Angello, J. C., and Wight, T. N., *Formation of Hyaluronan- and Versican-Rich Pericellular Matrix Is Required for Proliferation and Migration of Vascular Smooth Muscle Cells.* Arterioscler Thromb Vasc Biol, 1999. **19**(4): p. 1004-13.
2. Evanko, S. P., Tammi, M. I., Tammi, R. H., and Wight, T. N., *Hyaluronan-dependent pericellular matrix.* Adv. Drug Deliv. Rev., 2007. **59**(13): p. 1351-65.
3. Lee, G. M., Johnstone, B., Jacobson, K., and Caterson, B., *The Dynamic Structure of the Pericellular Matrix on Living Cells.* J Cell Biol, 1993. **123**(6): p. 1899-907.
4. van den Berg, B. M., Vink, H., and Spaan, J. A. E., *The Endothelial Glycocalyx Protects Against Myocardial Edema.* Circ Res, 2003. **92**(6): p. 592-94.
5. Henry, C. B. S. and Duling, B. R., *Permeation of the luminal capillary glycocalyx is determined by hyaluronan.* Am J Physiol Heart Circ Physiol, 1999. **277**(2): p. H508-H14.
6. Poole, C. A., *Review. Articular cartilage chondrons: form, function and failure.* J Anat, 1997. **191**(01): p. 1-13.
7. Guilak, F. and Mow, V. C., *The mechanical environment of the chondrocyte: a biphasic finite element model of cell-matrix interactions in articular cartilage.* J Biomech, 2000. **33**(12): p. 1663-73.
8. Knudson, C. B. and Knudson, W., *Hyaluronan-binding proteins in development, tissue homeostasis, and disease.* FASEB J, 1993. **7**: p. 1233-41.
9. Heldin, P. and Pertoft, H., *Synthesis and Assembly of the Hyaluronan-Containing Coats around Normal Human Mesothelial Cells.* Exp Cell Res, 1993. **208**(2): p. 422-29.
10. Knudson, W., Aguiar, D. J., Hua, Q., and Knudson, C. B., *CD44-Anchored Hyaluronan-Rich Pericellular Matrices: An Ultrastructural and Biochemical Analysis.* Exp Cell Res, 1996. **228**(2): p. 216-28.
11. Meyer, K. and Palmer, J. W., *The Polysaccharide of the Viterous Humour.* J Biol Chem, 1934. **107**(3): p. 629-34.
12. Lee, J. Y. and Spicer, A. P., *Hyaluronan: a multifunctional, megaDalton, stealth molecule.* Curr Opin Cell Biol, 2000. **12**(5): p. 581-86.
13. Scott, J. E. and Heatley, F., *Hyaluronan forms specific stable tertiary structures in aqueous solution: A 13C NMR study.* Proc. Natl. Acad. Sci. U. S. A., 1999. **96**(9): p. 4850-55.
14. Laurent, T. C. and Fraser, J. R., *Hyaluronan.* FASEB J, 1992. **6**(7): p. 2397-404.
15. Weissmann, B. and Meyer, K., *The Structure of Hyalobiuronic Acid and of Hyaluronic Acid from Umbilical Cord1,2.* J Am Chem Soc, 1954. **76**(7): p. 1753-57.
16. Almond, A., Brass, A., and Sheehan, J. K., *Oligosaccharides as Model Systems for Understanding Water−Biopolymer Interaction: Hydrated Dynamics of a Hyaluronan Decamer.* The Journal of Physical Chemistry B, 2000. **104**(23): p. 5634-40.
17. Scott, J. E., Cummings, C., Brass, A., and Chen, Y., *Secondary and tertiary structures of hyaluronan in aqueous solution, investigated by rotary shadowing-electron microscopy and computer simulation. Hyaluronan is a very efficient network-forming polymer.* Biochemistry Journal, 1991. **274**(3): p. 699-705.
18. Gribbon, P., Heng, B. C., and Hardingham, T. E., *The analysis of intermolecular interactions in concentrated hyaluronan solutions suggest no evidence for chain-chain association.* Biochemistry Journal, 2000. **350**: p. 329-35.
19. Gribbon, P., Heng, B. C., and Hardingham, T. E., *The analysis of intermolecular interactions in concentrated hyaluronan solutions suggest no evidence for chain-chain association.* Biochem. J., 2000. **350**: p. 329-35.

20. Hardingham, T., *Chapter 1 - Solution Properties of Hyaluronan*, in *Chemistry and Biology of Hyaluronan*, G.G. Hari, et al., Editors. 2004, Elsevier Science Ltd: Oxford. p. 1-19.
21. Day, A. J. and Sheehan, J. K., *Hyaluronan: polysaccharide chaos to protein organisation.* Curr. Opin. Struct. Biol., 2001. **11**: p. 617-22.
22. Lapčík, L., De Smedt, S., Demeester, J., and Chabreček, P., *Hyaluronan: Preparation, Structure, Properties, and Applications†.* Chemical Reviews, 1998. **98**(8): p. 2663-84.
23. Cowman, M. K., Spagnoli, C., Kudasheva, D., Li, M., Dyal, A., Kanai, S., and Balazs, E. A., *Extended, Relaxed, and Condensed Conformations of Hyaluronan Observed by Atomic Force Microscopy.* Biophys J, 2005. **88**(1): p. 590-602.
24. Toole, B. P., *Hyaluronan: from extracellular glue to pericellular cue.* Nat Rev Cancer, 2004. **4**: p. 528-39.
25. Day, A. J. and de la Motte, C. A., *Hyaluronan cross-linking: a protective mechanism in inflammation?* Trends Immunol., 2005. **26**(12): p. 637-43.
26. Goebeler, M., Kaufmann, D., Brocker, E. B., and Klein, C. E., *Migration of highly aggressive melanoma cells on hyaluronic acid is associated with functional changes, increased turnover and shedding of CD44 receptors.* J Cell Sci, 1996. **109**(7): p. 1957-64.
27. Delpech, B., Courel, M.-N., Maingonnat, C., Chauzy, C., Sesboüé, R., and Pratesi, G., *Hyaluronan Digestion and Synthesis in an Experimental Model of Metastatic Tumour.* Histochem J, 2001. **33**(9): p. 553-58.
28. Toole, B. P., *Hyaluronan in morphogenesis.* Semin. Cell Dev. Biol., 2001. **12**(2): p. 79-87.
29. Day, A. J. and Prestwich, G. D., *Hyaluronan-binding Proteins: Tying up the Giant.* J Biol Chem, 2002. **277**(7): p. 4585-88.
30. Watanabe, H., Yamada, Y., and Kimata, K., *Roles of Aggrecan, a Large Chondroitin Sulfate Proteoglycan, in Cartilage Structure and Function.* J. Biochem., 1998. **124**(4): p. 687-93.
31. Wight, T. N., Toole, B. P., and Hascall, V. C., *The Extracellular Matrix: an Overview*, R.P. Mecham, Editor. 2011, Springer Berlin Heidelberg. p. 147-95.
32. Kiani, C., Chen, L., Wu, Y. J., Yee, A. J., and Yang, B. B., *Structure and function of aggrecan.* Cell Res, 2002. **12**(1): p. 19-32.
33. Dean, D., Han, L., Grodzinsky, A. J., and Ortiz, C., *Compressive nanomechanics of opposing aggrecan macromolecules.* J Biomech, 2006. **39**(14): p. 2555-65.
34. Bruce Alberts, A. J., Julian Lewis, Martin Raff, Keith Roberts, and Peter Walter, *Molecular Biology of the Cell*. Vol. 4th edition. 2002, New York: Garland Science.
35. Ng, L., Grodzinsky, A. J., Patwari, P., Sandy, J., Plaas, A., and Ortiz, C., *Individual cartilage aggrecan macromolecules and their constituent glycosaminoglycans visualized via atomic force microscopy.* J Struct Biol, 2003. **143**(3): p. 242-57.
36. Heinegård, D. and Oldberg, Å., *Structure and biology of cartilage and bone matric noncollagenous macromolecules.* FASEB J., 1989. **3**: p. 2042-51.
37. Day, J. M., Olin, A. I., Murdoch, A. D., Canfield, A., Sasaki, T., Timpl, R., Hardingham, T. E., and Aspberg, A., *Alternative Splicing in the Aggrecan G3 Domain Influences Binding Interactions with Tenascin-C and Other Extracellular Matrix Proteins.* J Biol Chem, 2004. **279**(13): p. 12511-18.
38. Hedlund, H., Hedbom, E., Heinegård, D., Mengarelli-Widholm, S., Reinholt, F. P., and Svensson, O., *Association of the Aggrecan Keratan Sulfate-rich Region with Collagen in Bovine Articular Cartilage.* J Biol Chem, 1999. **274**(9): p. 5777-81.
39. Mow, V. C. and Guo, X. E., *Mchano-Electrochemical Properties of Articular Cartilage: Their Inhomogeneities and Anisotropies.* Annu Rev Biomed Eng, 2002. **4**(1): p. 175-209.
40. Groves, J. T., Boxer, S. G., and McConnell, H. M., *Lateral reorganization of fluid lipid membranes in response to the electric field produced by a buried charge.* J. Phys. Chem. B, 2000. **104**(47): p. 11409-15.

41. Cremer, P. S., Groves, J. T., Kung, L. A., and Boxer, S. G., *Writing and Erasing Barriers to Lateral Mobility into Fluid Phospholipid Bilayers.* Langmuir, 1999. **15**(11): p. 3893-96.
42. Richter, R. P., Bérat, R., and Brisson, A. R., *The formation of solid-supported lipid bilayers - an integrated view.* Langmuir, 2006. **22**(8): p. 3497-505.
43. Reviakine, I., Simon, A., and Brisson, A., *Effect of Ca2+ on the Morphology of Mixed DPPC−DOPS Supported Phospholipid Bilayers.* Langmuir, 2000. **16**(4): p. 1473-77.
44. Richter, R. P., Hock, K. K., Burkhartsmeyer, J., Boehm, H., Bingen, P., Wang, G., Steinmetz, N. F., Evans, D. J., and Spatz, J. P., *Membrane-Grafted Hyaluronan Films: A Well-Defined Model System of Glycoconjugate Cell Coats.* J. Am. Chem. Soc., 2007. **129**(17): p. 5306-07.
45. Baranova, N. S., Nilebäck, E., Haller, F. M., Briggs, D. C., Svedhem, S., Day, A. J., and Richter, R. P., *The Inflammation-Associated Protein TSG-6 Cross-Links Hyaluronan via Hyaluronan-Induced TSG-6 Oligomers.* J Biol Chem, 2011. **286**: p. 25675-86.
46. Binnig, G., Quate, C. F., and Gerber, C., *Atomic force microscope.* Phys. Rev. Lett., 1986. **56**(9): p. 930-33.
47. Drake, B., Prater, C. B., Weisenhorn, A. L., Gould, S. A., Albrecht, T. R., Quate, C. F., Cannell, D. S., Hansma, H. G., and Hansma, P. K., *Imaging crystals, polymers, and processes in water with the atomic force microscope.* Science, 1989. **243**(4898): p. 1586-9.
48. Rief, M. and Grubmuller, H., *Force spectroscopy of single biomolecules.* ChemPhysChem, 2002. **3**(3): p. 255-61.
49. Diezemann, G., Schlesier, T., Geil, B., and Janshoff, A., *Statistics of reversible bond dynamics observed in force-clamp spectroscopy.* Phys Rev E Stat Nonlin Soft Matter Phys, 2010. **82**(5 Pt 1): p. 051132.
50. *www.mpip-mainz.mpg.de/groups/butt/people/butt*.
51. Butt, H.-J., *Electrostatic interaction in atomic force microscopy.* Biophys. J., 1991. **60**(4): p. 777-85.
52. Ducker, W. A., Senden, T. J., and Pashley, R. M., *Direct measurement of colloidal forces using an atomic force microscope.* Nature, 1991. **353**(6341): p. 239-41.
53. Dimitriadis, E. K., Horkay, F., Maresca, J., Kachar, B., and Chadwick, R. S., *Determination of elastic moduli of thin layers of soft material using the atomic force microscope.* Biophys J, 2002. **82**(5): p. 2798-810.
54. Feiler, A., Plunkett, M. A., and Rutland, M. W., *Atomic Force Microscopy Measurements of Adsorbed Polyelectrolyte Layers. 1. Dynamics of Forces and Friction.* Langmuir, 2003. **19**: p. 4173-79.
55. Butt, H.-J., Cappella, B., and Kappl, M., *Force measurements with the atomic force microscope: Technique, interpretation and applications.* Surf. Sci. Rep., 2005. **59**(1-6): p. 1-152.
56. Ducker, W. A., Senden, T. J., and Pashley, R. M., *Direct measurement of colloidal forces using an atomic force microscope.* Nature, 1991. **353**: p. 239-41.
57. Ducker, W. A., Senden, T. J., and Pashley, R. M., *Measurement of forces in liquids using a force microscope.* Langmuir, 1992. **8**(7): p. 1831-36.
58. Butt, H.-J., Kappl, M., Mueller, H., Raiteri, R., Meyer, W., and Rühe, J., *Steric Forces Measured with the Atomic Force Microscope at Various Temperatures.* Langmuir, 1999. **15**(7): p. 2559-65.
59. Feldman, K., Hähner, G., Spencer, N. D., Harder, P., and Grunze, M., *Probing Resistance to Protein Adsorption of Oligo(ethylene glycol)-Terminated Self-Assembled Monolayers by Scanning Force Microscopy.* J Am Chem Soc, 1999. **121**(43): p. 10134-41.
60. Efremova, N. V., Bondurant, B., O'Brien, D. F., and Leckband, D. E., *Measurements of interbilayer forces and protein adsorption on uncharged lipid bilayers displaying poly(ethylene glycol) chains.* Biochemistry (Mosc.), 2000. **39**(12): p. 3441-51.

61. Claesson, P., *Poly(ethylene oxide) surface coatings: Relations between intermolecular forces, layer structure and protein repellency.* Colloids Surf., A, 1993. **77**(2): p. 109-18.
62. Israelachvili, J. N., *Intermolecular and Surface Forces*. Second ed. 1991: Academic Press.
63. Curtis, A. S., *The Mechanism of Adhesion of Cells to Glass. A Study by Interference Reflection Microscopy.* J Cell Biol, 1964. **20**: p. 199-215.
64. Limozin, L. and Sengupta, K., *Quantitative Reflection Interference Contrast Microscopy (RICM) in Soft Matter and Cell Adhesion.* ChemPhysChem, 2009. **10**(16): p. 2752-68.
65. Albrecht, R. and Weber, I., *Interference Reflection Microscopy*, in *eLS*. 2001, John Wiley & Sons, Ltd.
66. Kühner, M. and Sackmann, E., *Ultrathin Hydrated Dextran Films Grafted on Glass: Preparation and Characterization of Structural, Viscous, and Elastic Properties by Quantitative Microinterferometry.* Langmuir, 1996. **12**(20): p. 4866-76.
67. Rädler, J. and Sackmann, E., *On the Measurement of Weak Repulsive and Frictional Colloidal Forces by Reflection Interference Contrast Microscopy.* Langmuir, 1992. **8**(3): p. 848-53.
68. Schilling, J., Sengupta, K., Goennenwein, S., Bausch, A. R., and Sackmann, E., *Absolute interfacial distance measurements by dual-wavelength reflection interference contrast microscopy.* Phys. Rev. E, 2004. **69**(2): p. 021901.
69. Rodahl, M., Hook, F., Krozer, A., Brzezinski, P., and Kasemo, B., *Quartz crystal microbalance setup for frequency and Q-factor measurements in gaseous and liquid environments.* Rev. Sci. Instrum., 1995. **66**(7): p. 3924-30.
70. Richter, R. P., Mukhopadhyay, A., and Brisson, A., *Pathways of lipid vesicle deposition on solid surfaces: a combined QCM-D and AFM study.* Biophys J, 2003. **85**(5): p. 3035-47.
71. Keller, C. A. and Kasemo, B., *Surface specific kinetics of lipid vesicle adsorption measured with a quartz crystal microbalance.* Biophys J, 1998. **75**(3): p. 1397-402.
72. *www.tcd.ie/physics/surfaces/ellipsometery*.
73. Neal, W. E. J., *Application of ellipsometry to surface films and film growth.* Surface Technology, 1977. **6**(2): p. 81-110.
74. De Feijter, J. A., Benjamins, J., and Veer, F. A., *Ellipsometry as a tool to study the adsorption behavior of synthetic and biopolymers at the air–water interface.* Biopolymers, 1978. **17**(7): p. 1759-72.
75. Charnley, M., Textor, M., and Acikgoz, C., *Designed polymer structures with antifouling–antimicrobial properties.* React. Funct. Polym., 2011. **71**(3): p. 329-34.
76. Chen, M., Briscoe, W. H., Armes, S. P., and Klein, J., *Lubrication at physiological pressures by polyzwitterionic brushes.* Science, 2009. **323**(5922): p. 1698-701.
77. Senaratne, W., Andruzzi, L., and Ober, C. K., *Self-Assembled Monolayers and Polymer Brushes in Biotechnology: Current Applications and Future Perspectives.* Biomacromolecules, 2005. **6**(5): p. 2427-48.
78. Halperin, A., Tirrell, M., and Lodge, T., *Macromolecules: Synthesis, Order and Advanced Properties*. 1992, Springer Berlin / Heidelberg. p. 31-71.
79. de Gennes, P. G., *Polymers at an interface; a simplified view.* Adv. Colloid Interface Sci., 1987. **27**(3-4): p. 189-209.
80. Milner, S. T., *Polymer Brushes.* Science, 1991. **251**(4996): p. 905-14.
81. Milner, S. T., Witten, T. A., and Cates, M. E., *Theory of the grafted polymer brush.* Macromolecules, 1988. **21**(8): p. 2610-19.
82. Zhulina, E. B., Borisov, O. V., and Birshtein, T. M., *Structure of grafted polyelectrolyte layer.* J. Phys. II (France), 1992. **2**: p. 63-74.
83. Zhulina, E. B. and Borisov, O. V., *Structure and interaction of weakly charged polyelectrolyte brushes: self-consistent field theory.* J. Chem. Phys., 1997. **107**(15): p. 5952-67.

84. Pincus, P., *Colloid stabilization with grafted polyelectrolytes.* Macromolecules, 1991. **24**(10): p. 2912-19.
85. Borisov, O. V., Birshtein, T. M., and Zhulina, E. B., *Collapse of grafted polyelectrolyte layer.* J. Phy. II (France), 1991. **1**(5): p. 521-26.
86. Taunton, H. J., Toprakcioglu, C., Fetters, L. J., and Klein, J., *Interactions between surfaces bearing end-adsorbed chains in a good solvent.* Macromolecules, 1990. **23**(2): p. 571-80.
87. Kegler, K., Konieczny, M., Dominguez-Espinosa, G., Gutsche, C., Salomo, M., Kremer, F., and Likos, C. N., *Polyelectrolyte-Compression Forces between Spherical DNA Brushes.* Phys. Rev. Lett., 2008. **100**(11): p. 118302.
88. Borisov, O. V., Zhulina, E. B., and Birshtein, T. M., *Diagram of the states of a grafted polyelectrolyte layer.* Macromolecules, 1994. **27**(17): p. 4795-803.
89. Evanko, S. P., Tammi, M. I., Tammi, R. H., and Wight, T. N., *Hyaluronan-dependent pericellular matrix.* Adv. Drug Del. Rev., 2007. **59**(13): p. 1351-65.
90. Ren, K., Crouzier, T., Roy, C., and Picart, C., *Polyelectrolyte Multilayer Films of Controlled Stiffness Modulate Myoblast Cell Differentiation.* Adv. Funct. Mater., 2008. **18**(9): p. 1378-89.
91. Senaratne, W., Andruzzi, L., and Ober, C. K., *Self-Assembled Monolayers and Polymer Brushes in Biotechnology: Current Applications and Future Perspectives.* Biomacromolecules, 2005. **6**(5): p. 2427-48.
92. Fleer, G. J., Stuart, M. A. C., Scheutjens, J. M. H. M., Cosgrove, T., and Vincent, B., *Polymers At Interfaces*. 1993, London: Chapman & Hall.
93. Rubinstein, M. and Colby, R. H., *Polymer Physics*. 2003, Oxford: Oxford University Press.
94. Butt, H.-J., *Measuring electrostatic, van der Waals, and hydration forces in electrolyte solutions with an atomic force microscope.* Biophys. J., 1991. **60**(6): p. 1438-44.
95. Picart, C., Lavalle, P., Hubert, P., Cuisinier, F. J. G., Decher, G., Schaaf, P., and Voegel, J.-P., *Buildup Mechanism for Poly(L-lysine)/Hyaluronic Acid Films onto a Solid Surface.* Langmuir, 2001. **17**(23): p. 7414-24.
96. Clark, S. C., Walz, J. Y., and Ducker, W. A., *Atomic Force Microscopy Colloid-Probe Measurements with Explicit Measurement of Particle-Solution Separation.* Langmuir, 2004. **20**: p. 7616-22.
97. Heinrich, V., Wong, W. P., Halvorsen, K., and Evans, E., *Imaging biomolecular interactions by fast three-dimensional tracking of laser-confined carrier particles.* Langmuir, 2008. **24**(4): p. 1194-203.
98. Israelachvili, J., Min, Y., Akbulut, M., Alig, A., Carver, G., Greene, W., Kristiansen, K., Meyer, E., Pesika, N., Rosenberg, K., and Zeng, H., *Recent advances in the surface forces apparatus (SFA) technique.* Rep. Prog. Phys., 2010. **73**(3): p. 036601.
99. Seror, J., Merkher, Y., Kampf, N., Collinson, L., Day, A. J., Maroudas, A., and Klein, J., *Articular cartilage proteoglycans as boundary lubricants: structure and frictional interaction of surface-attached hyaluronan and hyaluronan-aggrecan complexes.* Biomacromolecules, 2011. **12**(10): p. 3432-43.
100. Hlady, V., Pierce, M., and Pungor, A., *Novel Method of Measuring Cantilever Deflection during an AFM Force Measurement.* Langmuir, 1996. **12**(22): p. 5244-46.
101. Stuart, J. K. and Hlady, V., *Reflection Interference Contrast Microscopy Combined with Scanning Force Miroscopy Verifies the Nature of Protein-Ligand Interaction Force Measurements.* Biophys. J., 1999. **76**: p. 500-08.
102. Dubreuil, F., Elsner, N., and Fery, A., *Elastic properties of polyelectrolyte capsules studied by atomic-force microscopy and RICM.* Eur. Phys. J. E, 2003. **12**(2): p. 215-21.
103. Robert, P., Sengupta, K., Puech, P.-H., Bongrand, P., and Limozin, L., *Tuning the Formation and Rupture of Single Ligand-Receptor Bonds by Hyaluronan-Induced Repulsion.* Biophys. J., 2008. **95**(8): p. 3999-4012.

104. Erath, J., Schmidt, S., and Fery, A., *Characterization of adhesion phenomena and contact of surfaces by soft colloidal probe AFM.* Soft Matter, 2010. **6**: p. 1432-37.
105. Takahashi, R., Kubota, K., Kawada, M., and Okamoto, A., *Effect of molecular weight distribution on the solution properties of sodium hyaluronate in 0.2M NaCl solution.* Biopolymers, 1999. **50**(1): p. 87-98.
106. Zhulina, E. B., Borisov, O. V., and Priamitsyn, V. A., *Theory of steric stabilization of colloid dispersions by grafted polymers.* J. Colloid Interface Sci., 1990. **137**(2): p. 495-511.
107. Zhulina, E. B., Priamitsyn, V. A., and Borisov, O. V., *Structure and conformational transitions in grafted polymer chain layers. A new theory.* Polymer Sci. U.S.S.R., 1989. **31**(1): p. 205-16.
108. Israelachvili, J. N. and McGuiggan, P. M., *Adhesion and short-range forces between surfaces. Part I: New apparatus for surface force measurements.* J. Mater. Res., 1990. **5**: p. 2223-31.
109. Klein, J., *Forces between mica surfaces bearing adsorbed macromolecules in liquid media.* Journal of the Chemical Society, Faraday Transactions 1: Physical Chemistry in Condensed Phases, 1983. **79**(1): p. 99-118.
110. Briscoe, W. H. and Horn, R. G., *Direct Measurement of Surface Forces Due to Charging of Solids Immersed in a Nonpolar Liquid.* Langmuir, 2002. **18**(10): p. 3945-56.
111. Fraser, J. R., Laurent, T. C., and Laurent, U. B., *Hyaluronan: its nature, distribution, functions and turnover.* J. Intern. Med., 1997. **242**(1): p. 27-33.
112. Cohen, M., Joester, D., Geiger, B., and Addadi, L., *Spatial and Temporal Sequence of Events in Cell Adhesion: From Molecular Recognition to Focal Adhesion Assembly.* ChemBioChem, 2004. **5**: p. 1393-99.
113. Rilla, K., Tiihonen, R., Kultti, A., Tammi, M., and Tammi, R., *Pericellular hyaluronan coat visualized in live cells with a fluorescent probe is scaffolded by plasma membrane protrusions.* J. Histochem. Cytochem., 2008. **56**(10): p. 901-10.
114. Sokolov, I., Iyer, S., Subba-Rao, V., Gaikwad, R. M., and Woodworth, C. D., *Detection of surface brush on biological cells in vitro with atomic force microscopy.* Appl. Phys. Lett., 2007. **91**: p. 023902-05.
115. Nijenhuis, N., Mizuno, D., Schmidt, C. F., Vink, H., and Spaan, J. A. E., *Microrheology of Hyaluronan Solutions: Implications for the Endothelial Glycocalyx.* Biomacromolecules, 2008. **9**(9): p. 2390-98.
116. Nijenhuis, N., Mizuno, D., Spaan, J. A., and Schmidt, C. F., *Viscoelastic response of a model endothelial glycocalyx.* PhBio, 2009. **6**(2): p. 025014.
117. Weinbaum, S., Zhang, X., Han, Y., Vink, H., and Cowin, S. C., *Mechanotransduction and flow across the endothelial glycocalyx.* Proc Natl Acad Sci U S A, 2003. **100**(13): p. 7988-95.
118. Boehm, H., Mundinger, T. A., Boehm, C. H. J., Hagel, V., Rauch, U., Spatz, J. P., and Curtis, J. E., *Mapping the mechanics and macromolecular organization of hyaluronan-rich cell coats.* Soft Matter, 2009. **5**: p. 4331-37.
119. Frey, S., Richter, R. P., and Görlich, D., *FG-Rich Repeats of Nuclear Pore Proteins Form a Three-Dimensional Meshwork with Hydrogel-Like Properties.* Science, 2006. **314**: p. 815-17.
120. Netz, R. R. and Andelman, D., *Neutral and charged polymers at interfaces.* PhR, 2003. **380**(1-2): p. 1-95.
121. Benz, M., Chien, N., and Israelachvili, J. N., *Lubrication and wear properties of grafted polyelectrolytes, hyaluronan and hylan, measured in the surface force apparatus.* J. Biomed. Mater. Res., 2004. **71A**: p. 6-15.

122. Tadmor, R., Chen, N., and Israelachvili, J. N., *Normal and Shear Forces between Mica and Model Membrane Surfaces with Adsorbed Hyaluronan.* Macromolecules, 2003. **36**(25): p. 9519-26.
123. Wolny, P. M., Banerji, S., Gounou, C., Brisson, A. R., Day, A. J., Jackson, D. G., and Richter, R. P., *Analysis of CD44-Hyaluronan Interactions in an Artificial Membrane System.* J. Biol. Chem., 2010. **285**(39): p. 30170-80.
124. Albersdörfer, A. and Sackmann, E., *Swelling behavior and viscoelasticity of ultrathin grafted hyaluronic acid films.* EPJB, 1999. **10**: p. 663-72.
125. Le Grimellec, C., Lesniewska, E., Cachia, C., Schreiber, J. P., de Fornel, F., and Goudonnet, J. P., *Imaging of the membrane surface of MDCK cells by atomic force microscopy.* Biophys. J., 1994. **67**(1): p. 36-41.
126. O'Shea, S. J., Welland, M. E., and Rayment, T., *An atomic force microscope study of grafted polymers on mica.* Langmuir, 1993. **9**(7): p. 1826-35.
127. Richter, R. P. and Brisson, A., *Characterization of lipid bilayers and protein assemblies supported on rough surfaces by atomic force microscopy.* Langmuir, 2003. **19**(5): p. 1632-40.
128. Knudson, W. and Knudson, C. B., *Assembly of chondrocyte-like pericellular matrix on non-chondrogenic cells.* J Cell Sci, 1991. **99**: p. 227-35.
129. Iyer, S., Gaikwad, R. M., Subba-Rao, V., Woodworth, C. D., and Sokolov, I., *Atomic force microscopy detects differences in the surface brush of normal and cancerous cells.* Nat. Nanotechnol., 2009. **4**(6): p. 389-93.
130. Ng, L., Hung, H. H., Sprunt, A., Chubinskaya, S., Ortiz, C., and Grodzinsky, A., *Nanomechanical properties of individual chondrocytes and their developing growth factor-stimulated pericellular matrix.* J Biomech, 2007. **40**(5): p. 1011-23.
131. Richter, R., Mukhopadhyay, A., and Brisson, A., *Pathways of lipid vesicle deposition on solid surfaces: a combined QCM-D and AFM study.* Biophys J, 2003. **85**(5): p. 3035-47.
132. Larsson, C., Rodahl, M., and Höök, F., *Characterization of DNA Immobilization and Subsequent Hybridization on a 2D Arrangement of Streptavidin on a Biotin-Modified Lipid Bilayer Supported on SiO2.* Anal. Chem., 2003. **75**(19): p. 5080-87.
133. Benes, M., Billy, D., Benda, A., Speijer, H., Hof, M., and Hermens, W. T., *Surface-dependent transitions during self-assembly of phospholipid membranes on mica, silica, and glass.* Langmuir, 2004. **20**(23): p. 10129-37.
134. Hardingham, T. E. and Muir, H., *The specific interaction of hyaluronic acid with cartillage proteoglycans.* Biochim Biophys Acta, 1972. **279**(2): p. 401-5.
135. Watanabe, H., Cheung, S. C., Itano, N., Kimata, K., and Yamada, Y., *Identification of Hyaluronan-binding Domains of Aggrecan.* J. Biol. Chem., 1997. **272**(44): p. 28057-65.
136. Buckwalter, J. A. and Rosenberg, L. C., *Electron microscopic studies of cartilage proteoglycans. Direct evidence for the variable length of the chondroitin sulfate-rich region of proteoglycan subunit core protein.* J Biol Chem, 1982. **257**: p. 9830-39.
137. Han, L., Dean, D., Ortiz, C., and Grodzinsky, A. J., *Lateral nanomechanics of cartilage aggrecan macromolecules.* Biophys J, 2007. **92**(4): p. 1384-98.
138. Dean, D., Han, L., Ortiz, C., and Grodzinsky, A. J., *Nanoscale Conformation and Compressibility of Cartilage Aggrecan Using Microcontact Printing and Atomic Force Microscopy.* Macromolecules, 2005. **38**: p. 4047-49.
139. Hodge, W. A., Fijan, R. S., Carlson, K. L., Burgess, R. G., Harris, W. H., and Mann, R. W., *Contact pressures in the human hip joint measured in vivo.* Proc Natl Acad Sci U S A, 1986. **83**(9): p. 2879-83.
140. Grodzinsky, A. J., Levenston, M. E., Jin, M., and Frank, E. H., *Cartilage tissue remodeling in response to mechanical forces.* Annu Rev Biomed Eng, 2000. **2**(1): p. 691-713.

141. Li, L. P., Buschmann, M. D., and Shirazi-Adl, A., *Strain-rate dependent stiffness of articular cartilage in unconfined compression.* J Biomech Eng, 2003. **125**(2): p. 161-8.
142. Loparic, M., Wirz, D., Daniels, A. U., Raiteri, R., Vanlandingham, M. R., Guex, G., Martin, I., Aebi, U., and Stolz, M., *Micro- and nanomechanical analysis of articular cartilage by indentation-type atomic force microscopy: validation with a gel-microfiber composite.* Biophys J, 2010. **98**(11): p. 2731-40.
143. Stolz, M., Gottardi, R., Raiteri, R., Miot, S., Martin, I., Imer, R., Staufer, U., Raducanu, A., Duggelin, M., Baschong, W., Daniels, A. U., Friederich, N. F., Aszodi, A., and Aebi, U., *Early detection of aging cartilage and osteoarthritis in mice and patient samples using atomic force microscopy.* Nat. Nanotechnol., 2009. **4**(3): p. 186-92.
144. Knudson, C. B. and Knudson, W., *Cartilage proteoglycans.* Semin. Cell Dev. Biol., 2001. **12**: p. 69-78.
145. Morra, M., *Engineering of Biomaterials Surfaces by Hyaluronan.* Biomacromolecules, 2005. **6**(3): p. 1205-23.
146. Crouzier, T. and Picart, C., *Ion pairing and hydration in polyelectrolyte multilayer films containing polysaccharides.* Biomacromolecules, 2009. **10**(2): p. 433-42.
147. Ren, K., Crouzier, T., Roy, C., and Picart, C., *Polyelectrolyte multilayer films of controlled stiffness modulate myoblast cells differentiation.* Adv. Funct. Mater., 2008. **18**(9): p. 1378-89.
148. Almond, A., Brass, A., and Sheehan, J. K., *Oligosaccharides as model systems for understanding water-biopolymer interaction: hydrated dynamics of a hyaluronan decamer.* J. Phys. Chem. B, 2000. **104**: p. 5634-40.
149. Cleland, R. L., Wang, J. L., and Detweiler, D. M., *Polyelectrolyte properties of sodium hyaluronate. 2. Potentiometric titration of hyaluronic acid.* Macromolecules, 1982. **15**: p. 386-95.
150. Talbot, P., Geiske, C., and Knoll, M., *Oocyte pickup by the mammalian oviduct.* Mol. Biol. Cell., 1999. **10**(1): p. 5-8.
151. Attili, S. and Richter, R. P., *Combining colloidal probe atomic force and reflection interference contrast microscopy to study the compressive mechanics of hyaluronan brushes.* Langmuir, 2012. **28**: p. 3206-16.
152. Fouissac, E., Milas, M., Rinaudo, M., and Borsali, R., *Influence of the Ionic Strength on the Dimensions of Sodium Hyaluronate.* Macromolecules, 1992. **25**(21): p. 5613-17.
153. Hayashi, K., Tsutsumi, K., Nakajima, F., Norisuye, T., and Teramoto, A., *Chain Stiffness and Excluded-Volume Effects in Solutions of Sodium Hyaluronate at High Ionic Strength.* Macromolecules, 1995. **28**(11): p. 3824-30.
154. Mendichi, R., Soltes, L., and Schieroni, A. G., *Evaluation of Radius of Gyration and Intrinsic Viscosity Molar Mass Dependence and Stiffness of Hyaluronan.* Biomacromolecules, 2003. **4**: p. 1805-10.
155. Kenworthy, A. K., Hristova, K., Needham, D., and McIntosh, T. J., *Range and magnitude of the steric pressure between bilayers containing phospholipids with covalently attached poly(ethylene glycol).* Biophys. J., 1995. **68**(5): p. 1921-36.
156. Balastre, M., Li, F., Schorr, P., Yang, J., Mays, J. W., and Tirrell, M. V., *A Study of Polyelectrolyte Brushes Formed from Adsorption of Amphiphilic Diblock Copolymers Using the Surface Forces Apparatus.* Macromolecules, 2002. **35**(25): p. 9480-86.
157. Zhulina, E. B., Borisov, O. V., and Birshtein, T. M., *Structure of grafted polyelectrolyte layer.* Journal de Physique II (France), 1992. **2**: p. 63-74.
158. Zhulina, E. B., Klein Wolterink, J., and Borisov, O. V., *Screening effects in a polyelectrolyte brush: self-consistent field theory.* Macromolecules, 2000. **33**: p. 4945-53.
159. Chen, L., Merlitz, H., He, S.-z., Wu, C.-X., and Sommer, J.-U., *Polyelectrolyte Brushes: Debye Approximation and Mean-Field Theory.* Macromolecules, 2011. **44**(8): p. 3109-16.

160. Biesheuvel, P. M., de Vos, W. M., and Amoskov, V. M., *Semianalytical Continuum Model for Nondilute Neutral and Charged Brushes Including Finite Stretching.* Macromolecules, 2008. **41**(16): p. 6254-59.
161. Zhulina, E. B., Birshtein, T. M., and Borisov, O. V., *Curved polymer and polyelectrolyte brushes beyond the Daoud-Cotton model.* Eur. Phys. J. E Soft Matter, 2006. **20**(3): p. 243-56.
162. Ballauf, M. and Borisov, O., *Polyeletrolyte Brushes.* Curr. Opin. Colloid Interface Sci., 2006. **11**: p. 316-23.
163. Skvortsov, A. M., Pavlushkov, I. V., Gorbunov, A. A., Zhulina, E. B., Borisov, O. V., and Pryamitsyn, V. A., *Structure of dense-grafted polymer monolayers.* Polymer Sci. U.S.S.R., 1988. **30**: p. 1706-15.
164. Milner, S. T., Witten, T. A., and Ctaes, M. E., *A parabolic density profile for grafted polymers.* Europhys. Lett., 1988. **5**(5): p. 413-18.
165. O'Shaughnessy, B. and Yang, Q., *Strongly charged polymer brushes.* Europhys. Lett., 2006. **75**(3): p. 427-33.
166. Manning, G. S., *Limiting Laws and Counterion Condensation in Polyelectrolyte Solutions I. Colligative Properties.* J. Chem. Phys., 1969. **51**(3): p. 924-33.
167. Birshtein, T. M. and Zhulina, E. B., *Conformations of star-branched molecules.* Polymer, 1984. **25**: p. 1453-61.
168. Gargiulo, V., Morando, M. A., Silipo, A., Nurisso, A., Perez, S., Imberty, A., Canada, F. J., Parrilli, M., Jimenez-Barbero, J., and De Castro, C., *Insights on the conformational properties of hyaluronic acid by using NMR residual dipolar couplings and MD simulations.* Glycobiology, 2010. **20**(10): p. 1208-16.
169. Kelley, T. W., Schorr, P. A., Johnson, K. D., Tirrell, M., and Frisbie, C. D., *Direct Force Measurements at Polymer Brush Surfaces by Atomic Force Microscopy.* Macromolecules, 1998. **31**(13): p. 4297-300.
170. Amiel, C., Sikka, M., Schneider, J. W., Tsao, Y.-H., Tirrell, M., and Mays, J. W., *Adsorption of Hydrophilic-Hydrophobic Block Copolymers on Silica from Aqueous Solutions.* Macromolecules, 1995. **28**(9): p. 3125-34.
171. Ahrens, H., Förster, S., and Helm, C. A., *Charged Polymer Brushes: Counterion Incorporation and Scaling Relations.* Phys. Rev. Lett., 1998. **81**(19): p. 4172-75.
172. Mir, Y., Auroy, P., and Auvray, L., *Density Profile of Polyelectrolyte Brushes.* Phys. Rev. Lett., 1995. **75**(15): p. 2863-66.
173. Tran, Y., Auroy, P., and Lee, L. T., *Determination of the Structure of Polyelectrolyte Brushes.* Macromolecules, 1999. **32**(26): p. 8952-64.
174. Hariharan, R., Biver, C., Mays, J., and Russel, W. B., *Ionic Strength and Curvature Effects in Flat amd Highly Curved Polyelectrolyte Brushes.* Macromolecules, 1998. **31**: p. 7506-13.
175. Biesalski, M., Johannsmann, D., and Rühe, J., *Electrolyte-induced collapse of a polyelectrolyte brush.* J. Chem. Phys., 2004. **120**(18): p. 8807-14.
176. Kegler, K., Konieczny, M., Dominguez-Espinosa, G., Gutsche, C., Salomo, M., Kremer, F., and Likos, C. N., *Polyelectrolyte-compression forces between spherical DNA brushes.* Phys. Rev. Lett., 2008. **100**(11): p. 118302-06.
177. Kegler, K., Salomo, M., and Kremer, F., *Forces of interaction between DNA-grafted colloids: an optical tweezer measurement.* Phys. Rev. Lett., 2007. **98**(5): p. 058304.
178. Scott, J. E., Cummings, C., Brass, A., and Chen, Y., *Secondary and tertiary structures of hyaluronan in aqueous solution, investigated by rotary shadowing-electron microscopy and computer simulation. Hyaluronan is a very efficient network-forming polymer.* Biochem. J., 1991. **274**: p. 699-705.

179. Gribbon, P., Heng, B. C., and Hardingham, T. E., *The Molecular Basis of the Solution Properties of Hyaluronan Investigated by Confocal Fluorescence Recovery After Photobleaching.* Biophys. J., 1999. **77**: p. 2210-16.
180. Merlitz, H., He, G.-L., Wu, C.-X., and Sommer, J.-U., *Surface Instabilities of Monodisperse and Densely Grafted Polymer Brushesities.* Macromolecules, 2008. **41**: p. 5070-72.
181. Merlitz, H., He, G.-L., Wu, C.-X., and Sommer, J.-U., *Nanoscale brushes: how to build a smart surface coating.* Phys. Rev. Lett., 2009. **102**(11): p. 115702-06.
182. Klushin, L. I. and Skvortsov, A. M., *Chain behavior in a polydisperse brush: depression of critical fluctuations.* Macromolecules, 1992. **25**(13): p. 3443–48.
183. Milner, S. T., Witten, T. A., and Cates, M. E., *Effects of polydispersity in the end-grafted polymer brush.* Macromolecules, 1989. **22**(2): p. 853-61.
184. Fredrickson, G. H. and Pincus, P., *Drainage of Compressed Polymer Layers: Dynamics of a "Squeezed Sponge".* Langmuir, 1991. **7**: p. 786-95.
185. Eisele, N. B., Frey, S., Piehler, J., Gorlich, D., and Richter, R. P., *Ultrathin nucleoporin phenylalanine-glycine repeat films and their interaction with nuclear transport receptors.* EMBO Rep, 2010. **11**(5): p. 366-72.
186. Burnham, N. A., Chen, X., Hodges, C. S., Matei, G. A., Thoreson, E. J., Roberts, C. J., Davies, M. C., and Tendler, S. J. B., *Comparison of calibration methods for atomic-force microscopy cantilevers.* Nanotechnology, 2003. **14**(1): p. 1-6.
187. Hutter, J. L. and Bechhoefer, J., *Calibration of atomic-force microscope tips.* Rev. Sci. Instrum., 1993. **64**(7): p. 1868-73.
188. Ploem, J. S., *Reflection-contrast microscopy as a tool for investigation of the attachment of living cells to glass surface, in Mononuclear Phagocytes in Immunity, Infection And Pathology.* (Von Furth, R., ed.), Blackwell, Oxford, UK., 1975: p. 405-21.
189. Sauerbrey, G., *Use of quartz vibrator for weighing thin films on a microbalance.* Z. Phys., 1959. **155**: p. 206-22.
190. Bingen, P., Wang, G., Steinmetz, N. F., Rodahl, M., and Richter, R. P., *Solvation effects in the quartz crystal microbalance with dissipation monitoring response to biomolecular adsorption. A phenomenological approach.* Anal Chem, 2008. **80**(23): p. 8880-90.
191. Daimon, M. and Masumura, A., *Measurement of the refractive index of distilled water from the near-infrared region to the ultraviolet region.* Appl. Opt., 2007. **46**(18): p. 3811-20.
192. Lide, D. R., *Handbook of Chemistry and Physics*. Vol. 85 edn. 2004, Boca Raton, FL, USA: CRC Press.
193. Mendichi, R., Schieroni, A. G., Grassi, C., and Re, A., *Characterization of ultra-high molar mass hyaluronan: 1. Off-line static methods.* Polymer, 1998. **39**(25): p. 6611-20.
194. Hardingham, T. E. and Fosang, A. J., *Proteoglycans: many forms and many functions.* FASEB J, 1992. **6**(3): p. 861-70.

Hyaluronan (HA) is a naturally occurring linear, negatively charged polysaccharide that plays a vital role in the mechanical integrity and function of pericellular matrices (PCM) surrounding many cell types and that is becoming increasingly popular in biomedical applications. Elucidating the mechanical properties of the highly hydrated HA-rich matrices would be valuable to understand how PCMs are organized and how they function. For a thorough investigation of the physical principles underlying the biological function of HA-rich pericellular matrices and provided the instrumental limitations in studying these highly hydrated systems *in vivo*, we have studied a model system that is based on films of HA that is end-grafted to a supported lipid bilayer. The major characterization techniques used are atomic force microscopy (AFM) and reflection interference contrast microscopy (RICM), as well as quartz crystal microbalance with dissipation monitoring (QCM-D) and spectroscopic ellipsometry.

In this thesis, we combine AFM, a widely used analytical approach to determine the behavior of molecules or thin films under mechanical force, and colloidal probe RICM, an established microinterferometric technique to determine the thickness of soft hydrated films, into one instrument. The combination provides interaction forces as a function of the absolute distance between the two approaching surfaces, information that may not easily be obtained with either technique alone. We employ the combined setup to quantify the thickness of films of end-grafted HA, and their resistance to compression forces as a function of the external salt concentration. We find a swelling behavior that is consistent with expectations for a polyelectrolyte brush. Through comparison of the experimental data with polymer theory, molecular parameters that govern the swelling and force response are identified and quantified. Intercalation of aggrecan, a HA-binding proteoglycan prominent in the PCM of chondrocytes, drastically increased the thickness and resistance of HA films to compression.

The combined AFM/RICM setup can serve as powerful tool to study the compression and frictional forces of surface-confined, hydrated films in general. The data on the mechanical properties of well-defined HA and HA/aggrecan composite films can be used as a reference point for future studies on the mechanics of PCMs.

CIC biomaGUNE, Biosurfaces Unit, Donostia-San Sebastian, Spain.

Max-Planck-Institute for Intelligent Systems Department of New Materials and Biosystems, Stuttgart, Germany.